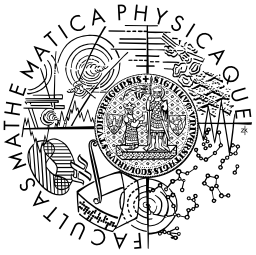

FACULTY
OF MATHEMATICS
AND PHYSICS
Charles University

DOCTORAL THESIS

Michal Zamkovský

Study of the extremely rare decay $K^+ \to \pi^+ \nu\bar{\nu}$ with the NA62 experiment at CERN

Institute of Particle and Nuclear Physics

Supervisor of the doctoral thesis:	Karol Kampf, RNDr., PhD, Doc.
Study programme:	Physics
Study branch:	Subnuclear Physics

Prague 2019

I declare that I carried out this doctoral thesis independently, and only with the cited sources, literature and other professional sources.

I understand that my work relates to the rights and obligations under the Act No. 121/2000 Sb., the Copyright Act, as amended, in particular the fact that the Charles University has the right to conclude a license agreement on the use of this work as a school work pursuant to Section 60 subsection 1 of the Copyright Act.

In ..... date ..... signature of the author

I wish to thank to my supervisor Karol Kampf for his limitless support during the whole period of my doctoral studies. I would like to express gratitude to professor Andrzej Buras who helped me to understand the theoretical scope of the thesis. I also want to thank Giuseppe Ruggiero for many fruitful discussions concerning the data analysis and to Rado Marchevski for his explanations of the background treatment. A special thank goes to Michal Koval, who carefully red the thesis, found countless mistakes and gave me valuable comments on both, the form and content of the text. In general I wish to thank to all people in the NA62 collaboration, for numerous encouraging discussions which helped me to understand how the experiment works.

Title: Study of the extremely rare decay $K^+ \to \pi^+ \nu\bar{\nu}$ with the NA62 experiment at CERN

Author: Michal Zamkovský

Institute: Institute of Particle and Nuclear Physics

Supervisor: Karol Kampf, RNDr., PhD, Doc., Institute of Particle and Nuclear Physics

Abstract: The decay $K^+ \to \pi^+ \nu\bar{\nu}$ has one of the most precisely predicted branching ratio at the level of 10^{-10}. It is forbidden at the tree level, which makes it sensitive to the effects of new physics. The NA62 experiment at the CERN SPS aims to measure the branching ratio of the $K^+ \to \pi^+ \nu\bar{\nu}$ using a unique decay-in-flight technique. NA62 took data so far in 2016-2018. The statistics acquired in 2016 allowed to reach Standard Model sensitivity for $K^+ \to \pi^+ \nu\bar{\nu}$. Owing to the statistics collected in 2017, NA62 surpasses the present best sensitivity. In the scope of this thesis, the preliminary result obtained from 2017 data sample is reported.

Keywords: kaon data analysis Standard Model

Contents

Introduction **4**

1 Theoretical Motivation **6**
1.1 Effective Hamiltonian for $K^+ \to \pi^+ \nu\bar{\nu}$ decay 6
1.2 Top quark contributions 7
1.3 Charm quark contributions 8
1.4 SM predictions 12
1.5 Grossman-Nir Bound 14
1.6 $K \to \pi\nu\bar{\nu}$ decays beyond the Standard Model 15
1.6.1 Minimal Flavour Violation models 17
1.6.2 $U(3)^3$ and $U(2)^3$ flavour symmetries 17
1.6.3 New $U(1)$ gauge symmetry 18

2 Experimental setup **19**
2.1 Beam line 19
2.2 Decay region and detectors 20
2.2.1 KTAG 22
2.2.2 GTK 22
2.2.3 CHANTI 23
2.2.4 Straw Spectrometer 24
2.2.5 LAV 25
2.2.6 RICH 26
2.2.7 CHOD 27
2.2.8 NA48 CHOD 27
2.2.9 MUV0 27
2.2.10 IRC 28
2.2.11 LKr 29
2.2.12 MUV1 31
2.2.13 MUV2 32
2.2.14 MUV3 32
2.2.15 SAC 33
2.2.16 HASC 34
2.3 Trigger 34
2.3.1 Level-0 trigger 34
2.3.2 Level-1 trigger 35
2.4 Data processing 36
2.4.1 Time calibration 36
2.4.2 Reconstruction 36
2.4.3 Data filter 37
2.5 Corrections 38
2.5.1 Beam parameters 40
2.5.2 Data Quality monitoring 40

3 Analysis procedure **41**
3.1 Analysis strategy for $K^+ \to \pi^+ \nu\bar{\nu}$ 41

4 Event selection **45**
4.1 Downstream track - detectors association . . . 45
4.1.1 STRAW Selection . . . 45
4.1.2 CHOD48 - STRAW association . . . 45
4.1.3 CHOD - STRAW Association . . . 46
4.1.4 RICH - STRAW association . . . 47
4.1.5 LKr - STRAW association . . . 48
4.1.6 Calorimetric energy reconstruction . . . 49
4.1.7 MUV3 - STRAW association . . . 50
4.2 Upstream - Downstream candidate matching . . . 51
4.2.1 Upstream candidate definition . . . 51
4.2.2 Association of the GTK candidate with the *pion candidate* 52
4.3 $\pi\nu\bar{\nu}$ sample selection . . . 55
4.3.1 Beam kinematics conditions . . . 55
4.3.2 Cuts against upstream backgrounds . . . 56
4.3.3 Kinematics criteria . . . 59
4.3.4 Single-track kaon decay . . . 59
4.3.5 Charged multiplicity rejection . . . 60
4.3.6 Particle identification . . . 63
4.3.7 Photon rejection . . . 67
4.4 Kinematic selection . . . 69

5 Background estimation **71**
5.1 Background from $\mathrm{K}_{2\pi}(\gamma)$ . . . 72
5.2 Background from $\mathrm{K}_{\mu 2}(\gamma)$ . . . 75
5.3 Background from $\mathrm{K}_{3\pi}$ . . . 79
5.4 Background from $\mathrm{K}^+ \to \pi^+\pi^- e + \nu_e(\mathrm{K}_{e4})$ . . . 79
5.5 Background from $\mathrm{K}^+ \to \pi^+\gamma\gamma$ . . . 81
5.6 Upstream Background . . . 81
5.6.1 Upstream background evaluation . . . 83
5.7 Background with positrons . . . 87
5.7.1 Study of RICH electron rejection . . . 87
5.7.2 $K^+ \to \pi^+\pi^0_D$ background . . . 89
5.7.3 $K^+ \to \mu^+\nu$; $\mu^+ \to e^+\nu\bar{\nu}$ background . . . 90
5.7.4 $K^+ \to e^+\nu$ background . . . 91
5.7.5 $\mathrm{K}^+ \to \pi^0 e^+\nu_e$ (K_{e3}) and $\mathrm{K}^+ \to \pi^0\mu^+\nu_\mu$ ($K_{\mu 3}$) background . 92
5.8 Background summary . . . 93
5.8.1 Final background validation . . . 93

6 $\mathrm{K}^+ \to \pi^+\nu\bar{\nu}$ analysis **95**
6.1 Single Event Sensitivity . . . 95
6.2 Efficiencies . . . 95
6.2.1 Trigger Efficiency . . . 97
6.2.2 Random Veto ε_{RV} . . . 99
6.2.3 Pion induced veto $\varepsilon_{veto}(\pi - induced)$ . . . 101
6.3 Normalization selection . . . 103
6.3.1 $K_{2\pi}$ normalization sample selection . . . 103
6.3.2 $K_{\mu 2}$ normalization sample selection . . . 104
6.4 Acceptances . . . 105

6.4.1 MC $\pi\nu\nu$ acceptance . . . 105
6.4.2 MC $\pi^+\pi^0$ acceptance . . . 106
6.4.3 MC $\mu^+\nu$ acceptance . . . 108
6.5 SES and number of expected events . . . 108
6.5.1 Using $K_{2\pi}$ as normalization . . . 110
6.5.2 Using $K_{\mu 2}$ as normalization . . . 112

7 Results **115**
7.1 Statistical interpretation . . . 117
7.2 Combined 2016 and 2017 results . . . 117

Conclusion **120**

A Appendix **121**
A.1 Full $K^+ \to \pi^+\pi^0$ selection . . . 121
A.2 $K^+ \to \pi^+\pi^+\pi^-$ selection . . . 122
A.3 $K^+ \to \pi^0 e^+ \nu_e$ selection . . . 122
A.4 π^0 decay identification . . . 123

Bibliography **124**

List of Figures **129**

List of Tables **135**

List of Abbreviations **137**

List of publications **138**

Introduction

The NA62 experiment at CERN SPS is a fixed target experiment aiming to study rare kaon decays [1]. Its main purpose is to measure the extremely rare decay $K^+ \to \pi^+\nu\bar{\nu}$ with an unprecedent precision. It is one of the rarest decays to be measured, with the branching ratio (BR) $\sim 10^{-11}$. The Standard Model (SM) expectation for its decay rate has a few per cent relative precision, not matched by any other loop-induced meson decay. In addition, its SM prediction is dominated by the uncertainties of the CKM parameters, which are improving thanks to the present day experiments. The decay rate is therefore uniquely sensitive to possible contributions mediated by new heavy particles, provides grounds for precision tests of flavour dynamics [2] and allows for a decisive test of the SM.

The $K^+ \to \pi^+\nu\bar{\nu}$ has been studied since 70's with the stopped kaons, when the first experiments set limits on its BR. The first observation was achieved by the BNL experiment E787, which found two events in the high momentum range ($211< P <229$ MeV/c) [3, 4] and one event in the low momentum range ($140< P <195$ MeV/c), compatible with the background [5, 6]. Then, the experiment E949 found one more event in the high momentum range ($211< P <229$ MeV/c) [7] and three events in the low momentum range ($140< P <199$ MeV/c)[8]. Both experiments have studied the kaon decays at rest. Their combined result, based on seven events, results in the BR value [9]:

$$BR(K^+ \to \pi^+\nu\bar{\nu}) = (1.73^{+1.15}_{-1.05}) \times 10^{-10}. \quad (1)$$

The NA62 experiment, starting with a pilot run in 2014 and the commissioning run in 2015, recorded its first $K^+ \to \pi^+\nu\bar{\nu}$ data in September 2016. The experiment is using a novel decay-in-flight technique. From the 2016 data sample, which corresponded to 45 days of data taking at low intensity, it reported one event observed in the signal region and set an upper limit on the BR [10]:

$$BR(K^+ \to \pi^+\nu\bar{\nu}) < 14 \times 10^{-10} \qquad @95\% \text{ CL}. \quad (2)$$

The NA62 continued the data taking during years 2017 for 160 days and 2018 for 217 days, at a higher beam intensity and collected ~ 30 times more data than in 2016. In the scope of this work, the results based on 2017 data set will be reported.

The experimental timeline is shown in Fig. 1.

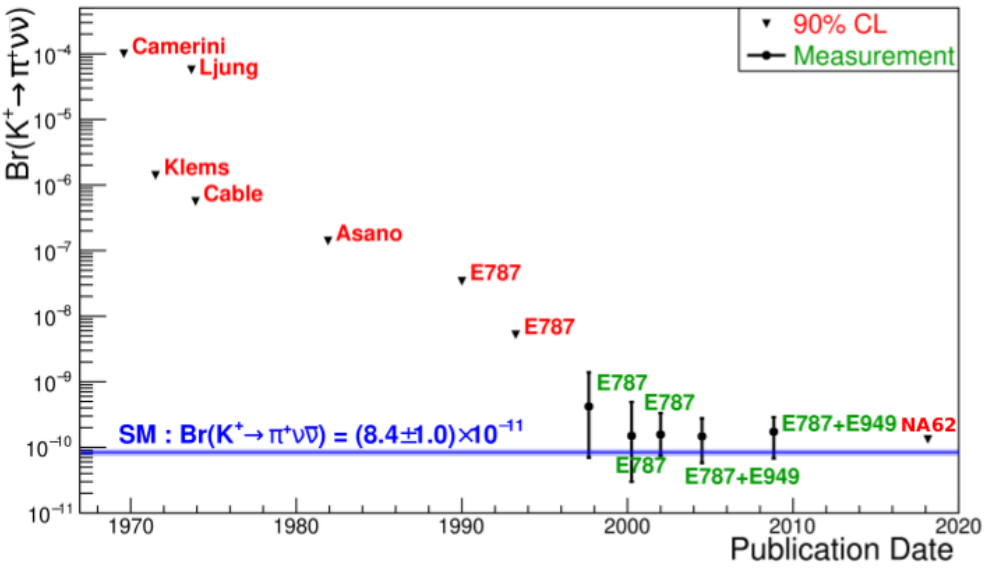

Figure 1: History of the experimental efforts directed towards the $K^+ \to \pi^+ \nu\bar{\nu}$ decay rate measurement.

This work is organised in the following way: a theoretical motivation is given in chapter 1, a description of the experiment layout, trigger and data proccessing is summarized in chapter 2, chapter 3 outlines the data selection strategy, followed by a detailed description of the selection in chapter 4. The background evaluation is covered in chapter 5. Then chapter 6 provides a review on the calculation of the Single Event Sensitivity, which is used to estimate the number of expected events. Result are summarized in chapter 7.

The pictures without citation are either made by the author or taken from the NA62 official repository. Unless mentioned as preliminary, all plots presented are unofficial.

1. Theoretical Motivation

Flavour-Changing Neutral Current (FCNC) processes carry an important information about the SM parameters. They are also sensitive to the effects Beyond the SM (BSM). However, the predictions of their amplitudes are usually plagued by uncertainties of the low energy QCD dynamics. The exceptions can be found in processes dominated by $W-$box and $Z-$penguin diagrams, where the low energy effects can be factorized. The FCNC are forbidden at the tree level in the SM and suppressed in the loops by the GIM mechanism [11], which cancels out all contributions independent on the quark masses running in the loops by the unitarity of the Cabbibo-Kobayashi-Maskawa (CKM) matrix. This makes the studied decays extremely rare, as they do not occur at the tree level, but only at the quantum loop level with the different mass dependent terms.

The extremely rare kaon decays $\mathrm{K}^+ \to \pi^+\nu\bar{\nu}$ and $\mathrm{K}^0_\mathrm{L} \to \pi^0\nu\bar{\nu}$ are considered as golden modes of flavour physics due to their very clean theoretical origin. They are dominated by the short-distance (SD) contributions between free quarks and leptons, producing an effective local four-fermion coupling:

$$\bar{s}_L\gamma_\mu d_L\bar{\nu}_{i_L}\gamma^\mu\nu_{i_L}, \tag{1.1}$$

where $\bar{s}_L$, d_L, $\bar{\nu_{i_L}}$, ν_{i_L} are the (anti)quark and (anti)neutrino quantum fields, and γ_μ are the Dirac matrices. The subscript L refers to left handed components of the fields, obtained from the projection:

$$\psi_L = \frac{1-\gamma_5}{2}\psi, \tag{1.2}$$

where γ_5 is a combination of Dirac matrices: $\gamma_5 = i\gamma_0\gamma_1\gamma_2\gamma_3\gamma_4$. The hadronic matrix element $\langle\pi|(\bar{s}d)_V|K\rangle$ is extracted, including isospin breaking corrections [12], from the accurately measured leading semi-leptonic decay $\mathrm{K}^+ \to \pi^0 e^+\nu_e$. The remaining long-distance interactions involving hadronic degrees of freedom in intermediate state were calculated in [13, 14] and were found to be three orders of magnitude smaller than the SD contribution at the level of BR.

This cleanliness makes them very sensitive to the effects of BSM physics. The precise measurement of the CP conserving charged mode and CP violating neutral mode offers a unique determination of the standard unitarity triangle [15]. Its comparison with the B physics can provide description of the New Physics (NP) flavour dynamics.

1.1 Effective Hamiltonian for $\mathrm{K}^+ \to \pi^+\nu\bar{\nu}$ decay

The effective interaction Hamiltonian describing $\bar{s} \to d\nu\bar{\nu}$ transition is the following:

$$\mathscr{H}_{eff} = \frac{G_F}{\sqrt{2}}\frac{\alpha}{2\pi\sin^2\theta_W}\sum_{\ell=e,\mu,\tau}\sum_{i=c,t}V^*_{is}V_{id}X(x_i)\bar{s}_L\gamma_\mu d_L\bar{\nu}_{\ell_L}\gamma^\mu\nu_{\ell_L}, \tag{1.3}$$

where G_F is a Fermi coupling constant, $\alpha(m)$ is an electromagnetic coupling constant, θ_W is a weak mixing angle, V_{ij} are the CKM matrix elements, $X(x_i)$

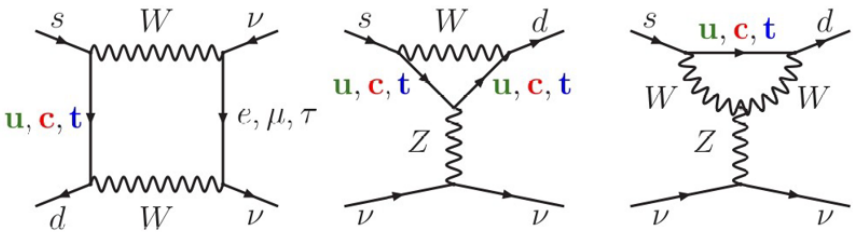

Figure 1.1: Feynman box-diagrams and $Z-$penguin diagram in the SM [19].

($x_i = m_i^2/M_W^2$, where m_i is a quark mass and M_W is a W boson mass) is a monotonically increasing function given below, and the four fermion interaction was explained in eq. (1.1). The BR, for a single lepton flavour, is then:

$$BR(K^+ \to \pi^+ \nu_l \bar{\nu}_l) = \frac{\alpha^2 BR(K^+ \to \pi^0 e^+ \nu)}{V_{us}^2 2\pi^2 \sin^4 \Theta_W} \left| \sum_{i=c,t} V_{is}^* V_{id} X(x_i) \right|^2 \tag{1.4}$$

The part

$$\sum_i V_{is}^* V_{id} X(x_i) = V_{ts}^* V_{td} (F(x_t) - F(x_u)) + V_{cs}^* V_{cd} (F(x_c) - F(x_u)) \tag{1.5}$$

describes top and charm quark contributions, originating in the SM at the lowest order from the box-diagrams and $Z-$penguin diagram shown in Fig. 1.1. The term $F(x_t)$, containing the top quark, is proportional to $\lambda^5 x_t$. It was calculated to the Next-to-leading order (NLO) in [16, 17]. In case of top quark, the lepton masses are negligible as they enter only in the ratio $r = m_\ell^2/m_t^2$.

Charm quark contribution enter through the term:

$$F(x_c) \sim \lambda \frac{m_c^2}{M_W^2} \ln \frac{M_W}{m_c}. \tag{1.6}$$

Here, only the muon and electron masses can be neglected, as the tau mass is comparable to charm mass and needs to be considered. The up quark contributions are subtracted from the top and charm loops. The calculation was carried out in Chiral perturbation theory and on Lattice [18]. The contribution of top quark dominates, but due to the smallness of $V_{ts}^* V_{td}$, the charm quark contribution, suppressed by the smallness of x_c, is also non-negligible and needs to be taken into account.

1.2 Top quark contributions

The top quark contribution to the BR (1.4) can be divided into the electroweak and the QCD part:

$$X(x_t) = X_0(x_t) + \frac{\alpha_s}{4\pi} X_1(x_t) + \frac{\alpha}{4\pi} X_{EW}(x_t), \tag{1.7}$$

where X_0 is the leading-order (LO) component

$$X_0(x) = \frac{x}{8} \left[-\frac{2+x}{1-x} + \frac{3x-6}{(1-x)^2} \ln x \right]; \tag{1.8}$$

and $X_1(x)$ refers to the NLO QCD correction, in the $\overline{MS}$ scheme:

$$\begin{aligned} X_1(x) = & - \frac{23x+5x^2-4x^3}{3(1-x)^2} + \frac{x-11x^2+x^3+x^4}{(1-x)^3}\ln x \\ & + \frac{8x+4x^2+x^3-x^4}{2(1-x)^3}\ln^2 x - \frac{4x-x^3}{(1-x)^2}\int_1^x dt\frac{\ln t}{1-t} \\ & + 8x\frac{\partial X_0(x)}{\partial x}\ln\frac{\mu^2}{M_W^2}, \end{aligned} \tag{1.9}$$

with $\mu = \mathcal{O}(m_t)$ and the subscript identifying the top quark was omitted. The 2-loop electroweak correction factor $r_X = 1 + X_{EW}(x_t)/X_0(x_t)$ has an approximate form [20]:

$$r_X = 1 - A + B \cdot C^{(M_t)/165\ \text{GeV}} - D\left(\frac{M_t}{165\ \text{GeV}}\right), \tag{1.10}$$

where

$$A = 1.11508, \quad B = 1.12316, \quad C = 1.15338, \quad D = 0.179454. \tag{1.11}$$

It approximates the full result within the limits 160 GeV$\leq M_t \leq$ 170 GeV to an accuracy of better than $\pm 0.05\%$.

The scale factor μ dependence in the last term of $X_1(x)$, at which the running top quark mass is defined, will cancel-out to the order considered with the scale dependence in $X_0(x(\mu))$ [16]. The theoretical uncertainty on the QCD corrections, arising from the top quark matching scale $\mu = \mathcal{O}(m_t)$, is at the level of 1% in NLO, compared to $\sim 6\%$ in LO. The sub-leading electroweak contributions to the theoretical uncertainty are estimated to be 2% [21]. The full electroweak two-loop correction calculation to the top quark contribution $X(x_t)$ performed in [20] resulted into the reduction of the scheme ambiguity down to 0.134%. The short-distance top quark function, including all mentioned corrections equals [22]:

$$X(x_t) = 1.481 \pm 0.005_{theory} \pm 0.008_{exp}, \tag{1.12}$$

where the theoretical uncertainty combines the remaining renormalization scale and scheme uncertainties, as well as the theoretical error on the $\overline{MS}$ parameters due to matching at the electroweak scale. The second uncertainty comes from the experimental error on the top quark and W masses entering the ratio x_t, and on the strong coupling $\alpha_s(M_Z)$.

A further theoretical development in top quark contribution at the NNLO level has been done. The $Z-$penguin 3-loop QCD corrections for $B_s \to \mu\mu$ process were calculated in [23] and they are directly applicable to $K \to \pi\nu\bar{\nu}$ decay. However, at NNLO, the QCD corrections to box diagram in $K \to \pi\nu\bar{\nu}$ and $B_s \to \mu\mu$ differ from each other. Nevertheless, they have been calculated recently [24] for the $X(x_t)$ function, so it is now known including NNLO QCD corrections. The preliminary result of the possible scale dependence of $X(x_t) \equiv X_t$ at NNLO is shown in Fig. 1.2 [24], together with the error budget at NLO [22].

1.3 Charm quark contributions

For the charm quark contribution, where both the weak scale $\mu_W = \mathcal{O}(M_W)$ and the low-energy scale $\mu_c = \mathcal{O}(m_c)$ are involved, the full Renormalization Group

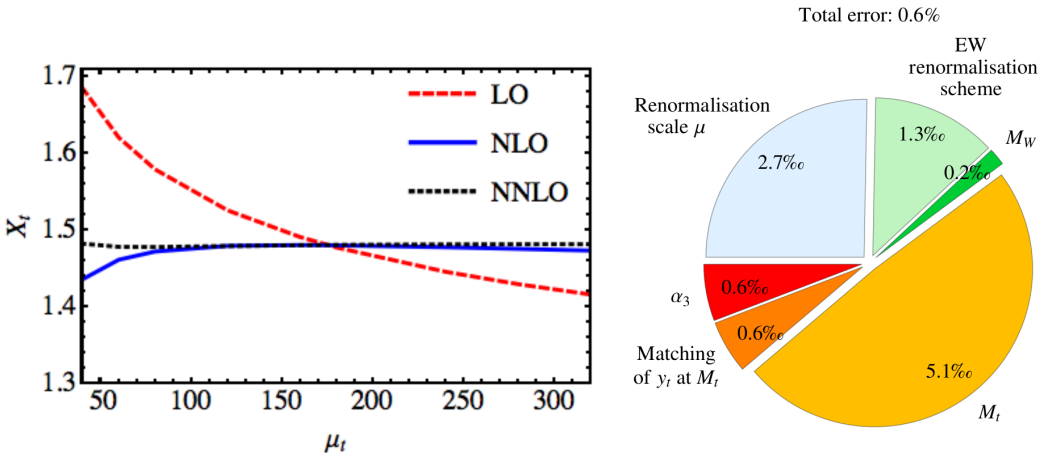

Figure 1.2: Possible scale dependence in NNLO for the top quark contribution (left) and error budget to $X(x_t)$ at NLO (right).

(RG) analysis is required. Hence the large logarithms $ln(\mu_W^2/\mu_c^2)$ are re-summed to all orders in α_s. In the following, a phenomenological parameter

$$P_c(X) = P_c^{SD} + \delta P_{c,u} \tag{1.13}$$

will be used. Here, P_c^{SD} describes the short-distance contribution of the charm quark:

$$P_c^{SD}(X) = \frac{1}{|V_{us}|^4}\left(\frac{2}{3}X^e(x_c) + \frac{1}{3}X^\tau(x_c)\right), \tag{1.14}$$

where $|V_{us}|$ is a CKM parameter and superscripts denotes the lepton flavour. The term

$$\delta P_{c,u} = 0.04 \pm 0.02 \tag{1.15}$$

represents the charm quark contribution of dimension-eight operators at the charm quark scale μ_c, combined with the long distance contributions [18]. Its error can be in principle improved with the help of the lattice QCD [25]. The short-distance part can be expanded in α_s:

$$\begin{aligned} P_c^{SD}(X) = &\frac{4\pi}{\alpha_s(\mu_c)}P_c^{(0)}(X) + P_c^{(1)}(X) + \frac{\alpha_s(\mu_c)}{4\pi}P_c^{(2)}(X) + \\ &+ \frac{4\pi\alpha}{\alpha_s^2(\mu_c)}P_c^{e}(X) + \frac{\alpha}{\alpha_s(\mu_c)}P_c^{(es)}(X), \end{aligned} \tag{1.16}$$

where the upper numerical indices represent contributions from L0, NLO and NNLO and the last two terms epitomize the electroweak corrections calculated in [26].

At the leading order, $P_c^{(0)}(X)$ has a theoretical uncertainty at the level of 26% [27, 28]. The NLO QCD correction calculation improves the uncertainty to $\sim 10\%$.

The charm quark contribution to the BR (1.4), resulting from the RG calculation in NLO logarithmic approximation, has the following form [29]:

$$X(x_c) = C_{NL} - 4B_{NL}^{1/2} \tag{1.17}$$

with

$$C_{NL} = \frac{x(m)}{32} K_c^{\frac{24}{25}} \left[\left(\frac{48}{7} K_+ + \frac{24}{11} K_- - \frac{696}{77} K_{33} \right) \left(\frac{1}{a(\mu)} + \frac{15212}{1875} (1 - K_c^{-1}) \right) \right.$$
$$+ \left(1 - \ln \frac{\mu^2}{m^2} \right) (16 K_+ - 8 K_-) - \frac{1176244}{13125} K_+ - \frac{2302}{6875} K_- + \frac{3529184}{48125} K_{33}$$
$$\left. + K \left(\frac{56248}{4375} K_+ - \frac{81448}{6875} K_- + \frac{4563698}{144375} K_{33} \right) \right] \tag{1.18}$$

where

$$K = \frac{a(M_W)}{a(\mu)} \qquad K_c = \frac{a(\mu)}{a(m)} \tag{1.19}$$

$$K_+ = K^{\frac{6}{25}} \qquad K_- = K^{\frac{-12}{25}} \qquad K_{33} = K^{\frac{-1}{25}} \tag{1.20}$$

$$B_{NL}^{(1/2)} = \frac{x(m)}{4} K_c^{\frac{24}{25}} \left[3(1 - K_2) \left(\frac{1}{a(\mu)} + \frac{15212}{1875} (1 - K_c^{-1}) \right) \right.$$
$$\left. - \ln \frac{\mu^2}{m^2} - \frac{r \ln r}{1 - r} - \frac{305}{12} + \frac{15212}{625} K_2 + \frac{15581}{7500} K K_2 \right] \tag{1.21}$$

Here $K_2 = K^{-1/25}$, $m = m_c$, $r = m_\ell^2/m_c^2$ (m_ℓ is the lepton mass) and the scale $\mu = \mathcal{O}(m_c)$. The function $a(\mu)$ represents the two-loop contributions:

$$a(\mu) = \frac{4\pi}{\beta_0 \ln \frac{\mu^2}{\Lambda^2}} \left[1 - \frac{\beta_1}{\beta_0^2} \frac{\ln \ln \frac{\mu^2}{\Lambda^2}}{\ln \frac{\mu^2}{\Lambda^2}} \right] \tag{1.22}$$

where $\Lambda \equiv \Lambda_{\overline{MS}}^{(4)}$. The parameters of the $\beta-$function are:

$$\beta_0 = \frac{11N - 2f}{3} \qquad \beta_1 = \frac{34}{3} N^2 - \frac{10}{3} N f - 2 C_F f \qquad C_F = \frac{N^2 - 1}{2N}, \tag{1.23}$$

where $N(f)$ is the number of colors (flavours). The part C_{NL} represents the contribution from the $Z-$penguin, while the $B_{NL}^{1/2}$ stands for the $W-$box diagram. The index $1/2$ refers to the weak isospin of the final state leptons. As in the case of top quark contribution, the scale dependence $ln(\mu^2/m^2)$ will cancel-out between C_{NL} and $B_{NL}^{(1/2)}$ to the considered order. From this computation, taking $|V_{us}| = 0.2248$, the charm quark contribution equals [30]:

$$P_c^{SD}(X) = 0.369 \pm 0.036_{theory} \pm 0.033_{m_c} \pm 0.009_{\alpha_s}, \tag{1.24}$$

where the parametric errors originate from the ranges of the charm quark $\overline{MS}$ mass $m_c(m_c)$ and the strong coupling constant $\alpha_s(M_Z)$.

To suppress the sizable dependence on the scale, one needs to proceed with the NNLO QCD correction. The full computation was performed in [30]. The explicit analytic expression is too long to be presented here and can be found in sections 6.8 and 7.7 of the mentioned publication for the $Z-$penguin and $W-$box

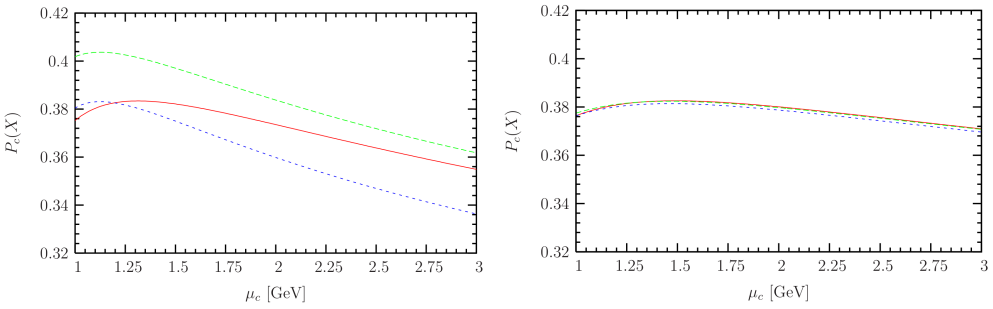

Figure 1.3: $P_c(X)$ as a function of the scale parameter μ_c in the NLO (left) and NNLO (right). The different lines correspond to various strategies of the $\alpha_s(\mu_c)$ computations [30].

diagrams, respectively. The approximate formula, including the electroweak corrections with precision of $\pm 0.05\%$ within the $1.15\text{GeV} \leq m_c(m_c) \leq 1.45\text{GeV}$ and $0.114 \leq \alpha_s(M_Z) \leq 0.122$ ranges is [26]:

$$P_c^{SD}(X) = 0.38049 \left(\frac{m_c(m_c)}{1.30\text{GeV}}\right)^{0.5081} \left(\frac{\alpha_s(M_Z)}{0.1176}\right)^{1.0192} \left(1 + \sum_{i,j} \kappa_{ij} L_{m_c}^i L_{\alpha_s}^j\right) \tag{1.25}$$
$$\pm\, 0.008707 \left(\frac{m_c(m_c)}{1.30\text{GeV}}\right)^{0.5276} \left(\frac{\alpha_s(M_Z)}{0.1176}\right)^{1.8970} \left(1 + \sum_{i,j} \varepsilon_{ij} L_{m_c}^i L_{\alpha_s}^j\right),$$

where

$$L_{m_c} = ln\left(\frac{m_c(m_c)}{1.30\text{GeV}}\right), \qquad L_{\alpha_s} = ln\left(\frac{\alpha_s(M_Z)}{0.1176}\right) \tag{1.26}$$

and

$$\kappa_{10} = 1.6624,\ \kappa_{01} = -2.3537,\ \kappa_{11} = -1.5862,\ \kappa_{20} = 1.5036,\ \kappa_{02} = -4.3477, \tag{1.27}$$

$$\varepsilon_{10} = -0.3537,\ \varepsilon_{01} = 0.6003,\ \varepsilon_{11} = -4.7652,\ \varepsilon_{20} = 1.0253,\ \varepsilon_{02} = 0.8866. \tag{1.28}$$

Incorporating results of the NNLO QCD and the electroweak corrections, and taking $|V_{us}| = 0.2252(9), m_c(m_c) = 1.279(13)\text{GeV}, \alpha_s(M_Z) = 0.1185(6)$, the $P_c^{SD}(X)$ equals:

$$P_c^{SD}(X) = 0.365 \pm 0.009_{theory} \pm 0.007_{m_c} \pm 0.004_{\alpha_s}. \tag{1.29}$$

The theoretical uncertainty is diminished by a factor 4, from 9.8% down to 2.5%. The scale dependence of $P_c^{SD}(X)$ in NLO and NNLO is graphically depicted in Fig. 1.3. The three different lines correspond to different approaches to evaluate $\alpha_s(\mu_c)$ from $\alpha_s(M_Z)$. These differences in NLO are quite sizable, but in NNLO the variation is within 0.2%.

The charm quark contribution is relevant only for the charged mode, the contribution for the neutral decay is well below 1%.

1.4 SM predictions

The branching ratio of the $K^+ \to \pi^+ \nu\bar{\nu}$ decay can be, after summing over three neutrino flavours, parametrized as:

$$BR(K^+ \to \pi^+ \nu\bar{\nu}) = \kappa_+(1+\Delta_{EM})\cdot \left[\left(\frac{\mathrm{Im}\lambda_t}{\lambda^5}X(x_t)\right)^2 + \left(\frac{\mathrm{Re}\lambda_c}{\lambda}(P_c^{SD}(X)+\delta P_c(X)) + \frac{\mathrm{Re}\lambda_t}{\lambda^5}X(x_t)\right)^2\right], \quad (1.30)$$

where the functions $X(x_t)$, $P_c^{SD}(X)$ and $\delta P_c(X)$ are the top and charm quark contributions explained above, with the factors in front of them being CKM parameters $\lambda = |V_{us}|$, $\lambda_i = V_{is}^* V_{id}$. These parameters can be expressed, with the accuracy up to $\mathcal{O}(\lambda^4)$ corrections (with respect to their leading order in λ), as follows:

$$Re\lambda_t \simeq |V_{ub}||V_{cb}|\cos\gamma(1-2\lambda^2) + (|V_{ub}|^2 - |V_{cb}|^2)\lambda\left(1-\frac{\lambda^2}{2}\right), \quad (1.31)$$

$$Im\lambda_t \simeq |V_{ub}||V_{cb}|\sin\gamma, \quad (1.32)$$

$$Re\lambda_c \simeq -\lambda\left(1-\frac{\lambda^2}{2}\right), \quad (1.33)$$

where γ is the angle of the unitarity triangle. The remaining long distance corrections are factored out into the following two parameters: κ_+ and Δ_{EM} [26]. The former contains higher-order electroweak corrections to the low energy matrix elements, in particular the relevant hadronic matrix elements that can be extracted from leading semi-leptonic decay $K^+ \to \pi^0 e^+ \nu$ taking into account isospin breaking. The latter denotes long distance QED corrections. A detailed analysis of these contributions to NLO and partially NNLO in chiral perturbation theory has been performed in [31], with the numerical values

$$\kappa_+ = (0.5173 \pm 0.0025)\times 10^{-10}(\lambda/0.225)^8 \quad \Delta_{EM} = -0.003. \quad (1.34)$$

Similarly, for the neutral mode [32]:

$$BR(K_L \to \pi^0 \nu\bar{\nu}) = \kappa_L \cdot \left(\frac{\mathrm{Im}\lambda_t}{\lambda^5}X(x_t)\right)^2, \quad (1.35)$$

where the symbols have the same meaning as in (1.30) and

$$\kappa_L = (2.231 \pm 0.013)\times 10^{-10}\left[\frac{\lambda}{0.225}\right]^8. \quad (1.36)$$

The parametric expressions for the BR of charged and neutral modes, in terms of the CKM parameters, are:

$$BR(K^+ \to \pi^+ \nu\bar{\nu}) = (8.39 \pm 0.30)\cdot 10^{-11}\left(\frac{|V_{cb}|}{0.0407}\right)^{2.8}\left(\frac{\gamma}{73.2^\circ}\right)^{0.74}, \quad (1.37)$$

$$BR(K_L^0 \to \pi^0 \nu\bar{\nu}) = (3.36 \pm 0.05)\cdot 10^{-11}\left(\frac{|V_{ub}|}{0.00388}\right)^2\left(\frac{|V_{cb}|}{0.0407}\right)^2\left(\frac{\sin\gamma}{\sin 73.2^\circ}\right)^2. \quad (1.38)$$

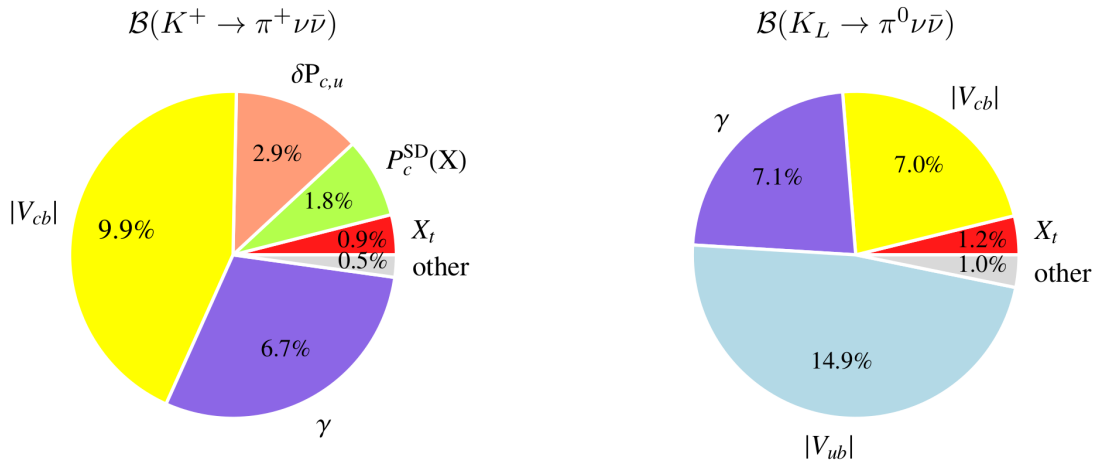

Figure 1.4: Error budget of the BR for the charged (left) and the neutral (right) $K \to \pi\nu\bar{\nu}$ decays [22].

Using the following values, where the CKM parameters represent the average of inclusive and exclusive tree-level measurements,

$$|V_{ub}| = (3.88 \pm 0.29) \times 10^{-3}, \quad |V_{cb}| = (40.7 \pm 1.4) \times 10^{-3}, \quad \gamma = (73.2^{+6.3}_{-7.0})^\circ, \tag{1.39}$$

one arrives to the SM predictions for the BR:

$$BR(\mathrm{K}^+ \to \pi^+\nu\bar{\nu}) = (8.4 \pm 1.0) \cdot 10^{-11}, \tag{1.40}$$
$$BR(\mathrm{K}^0_\mathrm{L} \to \pi^0\nu\bar{\nu}) = (3.4 \pm 0.6) \cdot 10^{-11}. \tag{1.41}$$

The errors are dominated by the uncertainties on the CKM parameters, namely $|V_{cb}|$ for the charged mode and $|V_{ub}|$ for the neutral mode. The pie charts of the error budgets are shown in Fig. 1.4.

An alternative approach is to estimate the BR within the SM with respect to the correlated decay $B_s \to \mu^+\mu^-$, which also depends on the $|V_{cb}|$. In this way, the $|V_{cb}|$ parameters will cancel out and one finds:

$$BR(\mathrm{K}^+ \to \pi^+\nu\bar{\nu}) = (8.39 \pm 0.58) \times 10^{-11} \times \left(\frac{\gamma}{73.2^\circ}\right)^{0.81} \left(\frac{BR(B_s \to \mu^+\mu^-)}{3.4 \cdot 10^{-9}}\right)^{1.42} \left(\frac{227.7}{F_{B_s}}\right)^{2.84}, \tag{1.42}$$

where F_{B_s} is a form-factor related to the $B-$decay. One can also rewrite the relation (1.37) with different CKM parameters:

$$BR(\mathrm{K}^+ \to \pi^+\nu\bar{\nu}) = (8.39 \pm 1.11) \times 10^{-11} \times \left(\frac{|\varepsilon_K|}{2.23 \cdot 10^{-3}}\right)^{1.07} \left(\frac{\gamma}{73.2^\circ}\right)^{-0.11} \left(\frac{V_{ub}}{3.88 \cdot 10^{-3}}\right)^{-0.95}. \tag{1.43}$$

It is obvious that the reduction of $BR(\mathrm{K}^+ \to \pi^+\nu\bar{\nu})$ implies also a reduction of $|\varepsilon_K|$.

The CKM parameters can be obtained in various ways, the ones reported above are taken as an average from measurements of inclusive and exclusive

processes at the tree level. In this way, they are not affected by the possible NP effects. However, if the loop observables are free of NP up to a reasonably high energy scale, one can obtain these parameters from the loop-level observables at the higher precision. Using experimental results of $|\varepsilon_K|$, Δ_{M_s}, $\Delta_{M_d}, S_{\psi K_s}$, the predictions for BR are:

$$BR(\mathrm{K}^+ \to \pi^+ \nu\bar{\nu}) = (9.11 \pm 0.72) \cdot 10^{-11}, \tag{1.44}$$

$$BR(\mathrm{K}_\mathrm{L}^0 \to \pi^0 \nu\bar{\nu}) = (3.00 \pm 0.31) \cdot 10^{-11}. \tag{1.45}$$

All the details on the extraction of the parameters relevant for the $\mathrm{K} \to \pi\nu\bar{n}u$ decays can be found in [22].

The result obtained from the tree level processes, represented by eq. (1.40), will be used in all estimations of the expected events on the analyzed data sample.

1.5 Grossman-Nir Bound

The neutral kaons are not present in the nature as a pure flavour states $|K^0\rangle = |d\bar{s}\rangle$ and $|\bar{K}^0\rangle = |\bar{d}s\rangle$, but as mass eigenstates $|K_L\rangle$ and $|K_S\rangle$, which are the combinations of the flavour states:

$$|K_L\rangle = p|K^0\rangle - q|\bar{K}^0\rangle, \qquad |K_S\rangle = p|K^0\rangle + q|\bar{K}^0\rangle, \tag{1.46}$$

where p and q are the complex parameters obeying $|p|^2 + |q|^2 = 1$.

Let's define a parameter λ as the ratio of the decay amplitudes $|K^0\rangle = |d\bar{s}\rangle$ and $|\bar{K}^0\rangle = |\bar{d}s\rangle$ into the same final state:

$$\lambda = \frac{q}{p}\frac{\langle \pi^0\nu\bar{\nu}|H|\bar{K}^0\rangle}{\langle \pi^0\nu\bar{\nu}|H|K^0\rangle}, \tag{1.47}$$

where H stands for the effective Hamiltonian describing the process. Then a ratio of the decay rates can be written in the following way:

$$\frac{\Gamma(K_L \to \pi^0\nu\bar{\nu})}{\Gamma(K_S \to \pi^0\nu\bar{\nu})} = \frac{1 + |\lambda|^2 - 2Re\lambda}{1 + |\lambda|^2 + 2Re\lambda}. \tag{1.48}$$

Now, following the discussion in [33], one can define θ as the relative phase between $K - \bar{K}$ mixing amplitude and the $s \to d\nu\bar{\nu}$ decay amplitude, namely $\lambda = e^{2i\theta}$, and from eq. (1.48):

$$\frac{\Gamma(K_L \to \pi^0\nu\bar{\nu})}{\Gamma(K_S \to \pi^0\nu\bar{\nu})} = \frac{1 - \cos 2\theta}{1 + \cos 2\theta} = \tan 2\theta. \tag{1.49}$$

In experiment, it is practically impossible to measure $\Gamma(K_S \to \pi^0\nu\bar{\nu})$, but one can use the isospin symmetry relation:

$$\frac{A(K^0 \to \pi^0\nu\bar{\nu})}{A(K^+ \to \pi^+\nu\bar{\nu})} = \frac{1}{\sqrt{2}} \tag{1.50}$$

to replace the denominator in equation (1.49) by the charged mode, measurable experimentally:

$$r_{is}\frac{\Gamma(K_L \to \pi^0\nu\bar{\nu})}{\Gamma(K^+ \to \pi^+\nu\bar{\nu})} = \frac{1 - \cos 2\theta}{2} = \sin^2\theta, \tag{1.51}$$

where $r_{is} = 0.954$ is the isospin breaking factor [12] arising from the differences in the $\pi^+ - \pi^0$ and $K^+ - K^0$ masses and the different vector form factors. The ratio (1.51) is most useful if the possible NP is dominated by the same combination of mixing angle in both, $K_L \to \pi^0\nu\bar{\nu}$ and $K^+ \to \pi^+\nu\bar{\nu}$. In that case, the phase of this combination is directly identified with θ, and no additional new parameters are needed. As $\sin^2\theta \leq 1$, eq. (1.51) allows one to set an upper limit on $BR(K_L \to \pi^0\nu\bar{\nu})$ from the charged mode. Considering differences in the life times $\tau_{K_L}/\tau_{K^+} = 4.17$, one gets:

$$BR(K_L \to \pi^0\nu\bar{\nu}) < 4.37 \times BR(K^+ \to \pi^+\nu\bar{\nu}). \tag{1.52}$$

This relation is called the Grossman-Nir bound.

1.6 $\mathrm{K} \to \pi\nu\bar{\nu}$ decays beyond the Standard Model

The theoretical cleanliness of these processes makes them an excellent probe for the BSM effects. They were studied from the theoretical point of view in several NP scenarios, which will enhance or reduce its BRs. Even the results precisely matching the SM predictions will have a valuable impact on several NP scenarios, as they can set limits where the NP will emerge.

To account for the effects beyond the SM, the relations (1.30) and (1.35) can be rewritten as follows [34]:

$$BR(\mathrm{K}^+ \to \pi^+\nu\bar{\nu}) = \kappa_+(1+\Delta_{EM}) \cdot \left[\left(\frac{\mathrm{Im}\lambda_t}{\lambda^5}X_{eff}\right)^2 + \left(\frac{\mathrm{Re}\lambda_c}{\lambda}P_c(X) + \frac{\mathrm{Re}\lambda_t}{\lambda^5}X_{eff}\right)^2\right], \tag{1.53}$$

$$BR(\mathrm{K_L} \to \pi^0\nu\bar{\nu}) = \kappa_L \cdot \left(\frac{\mathrm{Im}\lambda_t}{\lambda^5}X_{eff}\right)^2, \tag{1.54}$$

where X_{eff} represents the SM part discussed above and the NP part parametrized by ξ and θ:

$$X_{eff} = V_{ts}^* V_{td}(X(x_t) + X_{NP}(x_t)) = V_{ts}^* V_{td} X^{SM}(1 + \xi e^{i\theta}), \tag{1.55}$$

which can be expressed also as a function of the BR:

$$\mathrm{Re}X_{eff} = -\lambda^5 \left[\frac{BR(\mathrm{K}^+ \to \pi^+\nu\bar{\nu})}{\kappa_+(1+\Delta_{EM})} - \frac{BR(\mathrm{K_L} \to \pi^0\nu\bar{\nu})}{\kappa_L}\right]^{1/2} - \lambda^4 \mathrm{Re}\lambda_c P_c(X), \tag{1.56}$$

$$\mathrm{Im}X_{eff} = \lambda^5 \left[\frac{BR(\mathrm{K_L} \to \pi^0\nu\bar{\nu})}{\kappa_L}\right]^{1/2}. \tag{1.57}$$

Precise measurement of the $\mathrm{K} \to \pi\nu\bar{\nu}$ BRs will improve the understanding of NP structure and together with other rare decay measurements, such as $B'_{s,d} \to \mu^+\mu^-$ and $B \to K(K^*)\nu\bar{\nu}$, it can identify the appropriate SM extension. Some examples of NP, which can be tested: Minimal Flavour Violation models, Z' FCNC, Littlest Higgs with T-parity [35], Randall-Sundrum models with custodial symmetry [36], $U(3)^3$ and $U(2)^3$ models, minimal Super-symmetric model with large $\tan\beta$ [37, 38], Lepton Flavour Unitarity violation models [39] and models with leptoquarks [40]. The effects of the first four mentioned scenarios are depicted in Fig. 1.5.

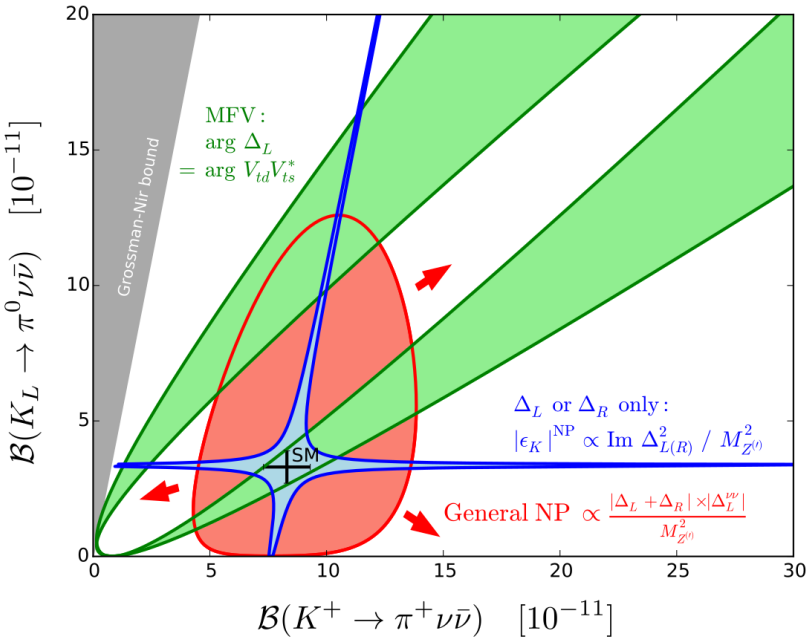

Figure 1.5: Example of the NP correlations in the plane of K $\to \pi\nu\bar{\nu}$ BRs [34]. The green bands correspond to Minimal Flavour Violation models, where no right-handed interactions are present. The blue lines illustrate the correlation between the BRs in the Littlest Higgs with T-parity and Z' FCNC models, with pure left-handed or right-handed couplings. The expanding red area represent the models with general left- and right-handed couplings, such as Randall-Sundrum models with custodial symmetry, where no correlation is expected.

1.6.1 Minimal Flavour Violation models

The Minimal Flavour Violation (MFV) models are the class of models with no extra flavour changing interactions beyond the SM ones, i.e. there are no FCNC at the tree level. Such models are SM, Two Higgs Doublet Model I, II, Minimal Super-symmetric Model with minimal flavour violation and not too large $\tan\beta$, and SM with one extra large dimension. The MFV models can be probed with the $K \to \pi\nu\bar{\nu}$ decays. Using the "reduced" BR:

$$B_+ = \frac{BR(K^+ \to \pi^+\nu\bar{\nu})}{\kappa_+}; \qquad B_L = \frac{BR(K_L \to \pi^0\nu\bar{\nu})}{\kappa_L}, \tag{1.58}$$

one can write [41]:

$$\sin 2\beta = \frac{2r_s}{1+r_s^2}; \quad r_s = \sqrt{\sigma}\frac{\sqrt{\sigma(B_+ - B_L)} - P_c(X)}{\sqrt{B_L}}; \quad \sigma = \frac{1}{(1-\frac{\lambda^2}{2})^2}, \tag{1.59}$$

where β is the angle of the unitarity triangle. Here, the $\sin 2\beta$ depends only on the $K \to \pi\nu\bar{\nu}$ BRs and a precisely calculated function $P_c(X)$. One can get $\sin 2\beta$ also from the $B_d \to J/\psi K_S$ decay. Then, in the SM and MFV, to a very good approximation, holds the following relation:

$$(\sin 2\beta)_{\pi\nu\nu} = (\sin 2\beta)_{J/\psi K_S}. \tag{1.60}$$

Comparing these two methods will provide an important test of the MFV idea. Indeed, in the $K \to \pi\nu\bar{\nu}$ decays the phase β comes from the $Z-$penguin diagram, whereas in the latter it originates in the $B_d^0 - \bar{B}_d^0$ box diagram. Consequently, with $\sin 2\beta$ extracted from $B_d \to J/\psi K_S$ and the measured BR for $K^+ \to \pi^+\nu\bar{\nu}$, one can predict $BR(K_L \to \pi^0\nu\bar{\nu})$. Then, in the full class of the MFV model, independent of any new parameters, $BR(K_L \to \pi^0\nu\bar{\nu})$ can have two values, corresponding to different signs of X. Hence, the measurement of $BR(K_L \to \pi^0\nu\bar{\nu})$ will either pick one of the possible values or discard all MFV models [42].

1.6.2 $U(3)^3$ and $U(2)^3$ flavour symmetries

The $U(3)^3$ is a MFV model with one new real parameter a, introducing the Z quark flavour violating coupling [34]:

$$\Delta_L^{sd}(Z) = aV_{ts}^*V_{td}, \tag{1.61}$$

and modifying the top quark function $X(x_t)$:

$$\Delta(X(x_t)) = a\frac{\pi\Delta_L^{\nu\bar{\nu}}(Z)}{2M_Z^2M_W^2G_F^2}, \tag{1.62}$$

where G_F is the Fermi coupling constant. From eq. (1.62) it is clear that this model can shift the decay rates. As parameter a can be either positive or negative, it can enhance the BR or decrease it. In the $U(2)^3$ model, two new complex parameters a and b are introduced, changing CKM parameters differently for kaon and B decays. Even though the part relevant for the kaon decays is unchanged, it is affecting B decays and so the $\sin 2\beta$ mentioned in MFV section will be different with respect to the one obtained from kaon BRs.

1.6.3 New $U(1)$ gauge symmetry

One of the simplest extension of the SM is by introducing new $U(1)$ gauge symmetry represented by a heavy neutral gauge boson Z' [43]. In general, it brings several new parameters: the mass $M_{Z'}$, the coupling constant and depending on the flavour symmetries, the parameters a and b as explained in section 1.6.2. It can in principle have left- or right-handed or both couplings to fermions and introduce FCNC processes in the quark sector already at the tree level. All the observables in this model are proportional to the ratio of the Z' couplings over the $M_{Z'}$. The discussed processes can probe this model up to $M_{Z'} = 200$ TeV, considering the largest coupling allowed [44].

2. Experimental setup

The NA62 experiment is located in the North Area of CERN (Conseil Européen pour la Recherche Nucléaire), the European Organization for Nuclear Research. It is a fixed target experiment, using a primary proton beam from the accelerator SPS (Super Proton Synchrotron).

2.1 Beam line

The 400 GeV/c primary protons from the SPS are delivered in 30 s super-cycles with two five-second flat-top spills. They impinge on the T10 target, a beryllium cylinder, which is 2 mm in diameter and 400 mm long, located in the tunnel between SPS and the experimental hall. The beam-target collisions produce a variety of particles of different momenta. The secondary hadron beam (K12) is selected by the set of dipole magnets, focusing quadrupole magnets, muon sweepers and collimators. The schematic overview of the K12 beam line is shown in Fig. 2.1. First, the beam is focused by a triplet of radiation-hard, small-aperture, quadrupole magnets (Q1, Q2, Q3). Then, its momentum and charge are defined by the first two magnets in a four dipole achromat (A1) and by momentum-defining slits incorporated into a 3.2 m thick copper/iron proton beam dump (TAX1, TAX2). Between the TAXes, there are multiple tungsten plates, optimized to slow down positrons by Bremsstrahlung and minimize the loss of hadrons by scattering. The nominal momentum value is 75 GeV/c with 1% momentum spread (rms), transverse size is 60×30 mm^2 and the rate of particles is 450 MHz. The composition of the secondary beam is dominated by pions ($\sim$70%) and protons ($\sim$24%), with about 6% of kaons. The beam is accompanied by a muon halo at the rate of 3 MHz.

After the achromat A1, a quadrupole triplet (Q4, Q5, Q6) refocuses the beam in the vertical plane and brings it parallel with limited width in the horizontal plane. In between these quadrupoles are collimators (C1, C2), redefining the vertical and horizontal acceptance of the transmitted beam. Following the quadrupole triplet, a collimator (C3) redefines the beam at the second focus in the vertical plane and absorbs the positrons degraded in momenta by the tungsten plates between the TAXes. Then the beam enters into three 2 m long dipole magnets (B3) through the 40 mm diameter bore in the iron plates inserted between the dipole poles. The magnetic field in the iron sweeps aside muons of both signs, while the impact on the beam is canceled by two steering dipoles (TRIM2, TRIM3). The dipole B3 is followed by two quadrupoles (Q7, Q8), rendering the beam parallel in both planes to match the requirements of the Differential Cerenkov counter (KTAG), and two cleaning collimators (C4, C5) absorbing the tails of the beam. After KTAG, two quadrupoles (Q9, Q10) prepare the beam for a momentum measurement in the silicon pixel beam spectrometer GTK. Following the GTK, a steering magnet (TRIM5) deflects the beam by +1.2 mrad towards a positive X to compensate a subsequent kick of -3.6 mrad by the spectrometer magnet MNP33. Figure 2.2 illustrates the beam position in the vacuum tank and an effect of the spectrometer magnet MNP33. The beam is entering the decay region after TRIM5 and the undecayed component of the beam is steered

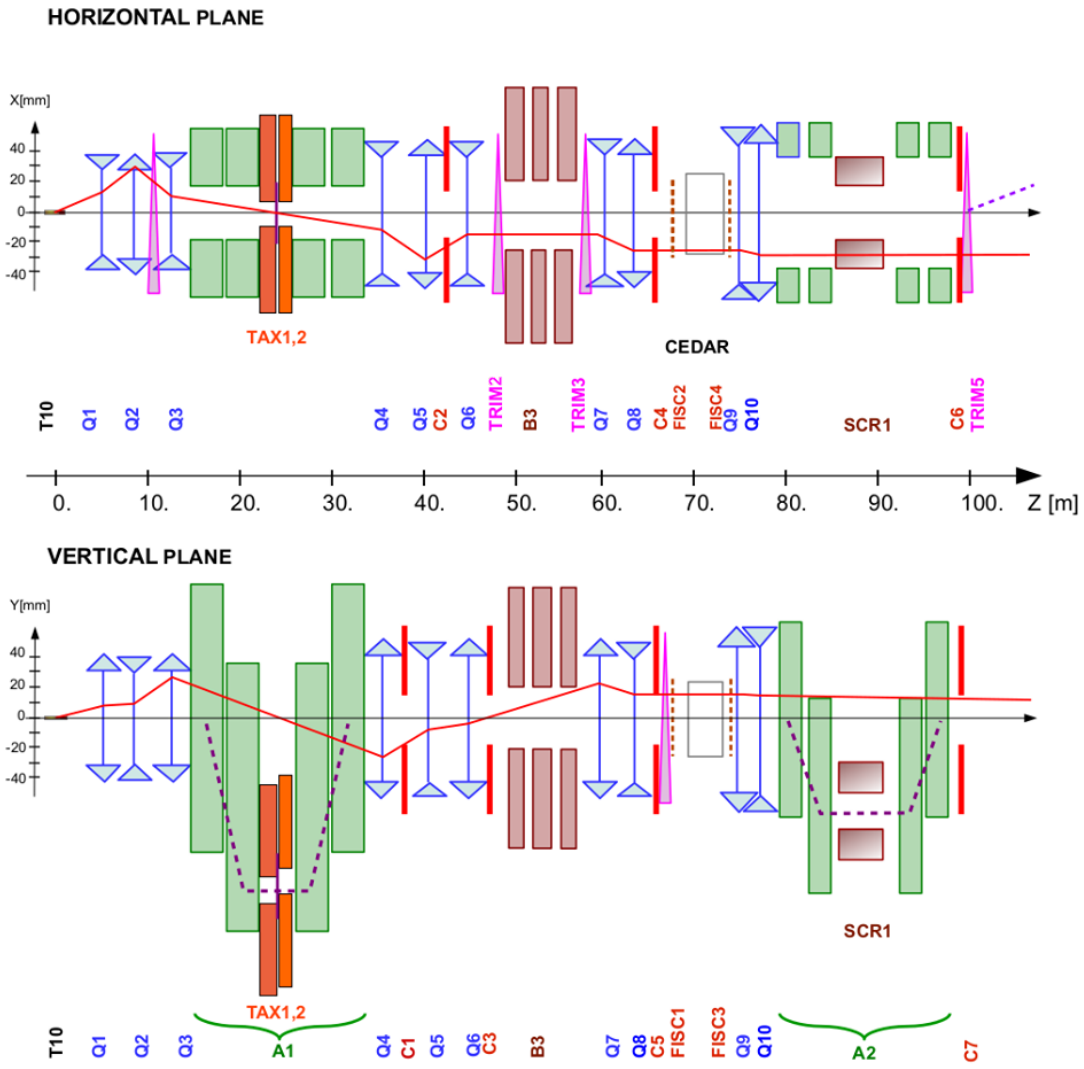

Figure 2.1: Schematic drawing of the K12 beam line. The solid red line represents the trajectory of a particle produced in the middle of the target at a nominal momentum at the indicated angle. The dashed line corresponds to the trajectory of an initially on-axis particle with the nominal momentum [45].

inside the beam pipe when passing the downstream detectors.

2.2 Decay region and detectors

The first upstream detectors are the kaon tagging detector (KTAG), used to identify K^+ in the beam, the beam spectrometer GTK and the Charged Anti-counter detector (CHANTI), used to suppress products of inelastic interactions in the GTK. They are followed by a 117 m long vacuum tank, starting 102.4 m downstream of the target. The fiducial volume (FV) is defined in the first 60 m of the vacuum region, where about 13% of the K^+ entering the experiment decay. The tank is evacuated to 10^{-6} mbar and contains four tracking stations of the magnetic spectrometer (STRAW).

Around the vacuum tube ring-shaped Large Angle Vetoes (LAV) are located,

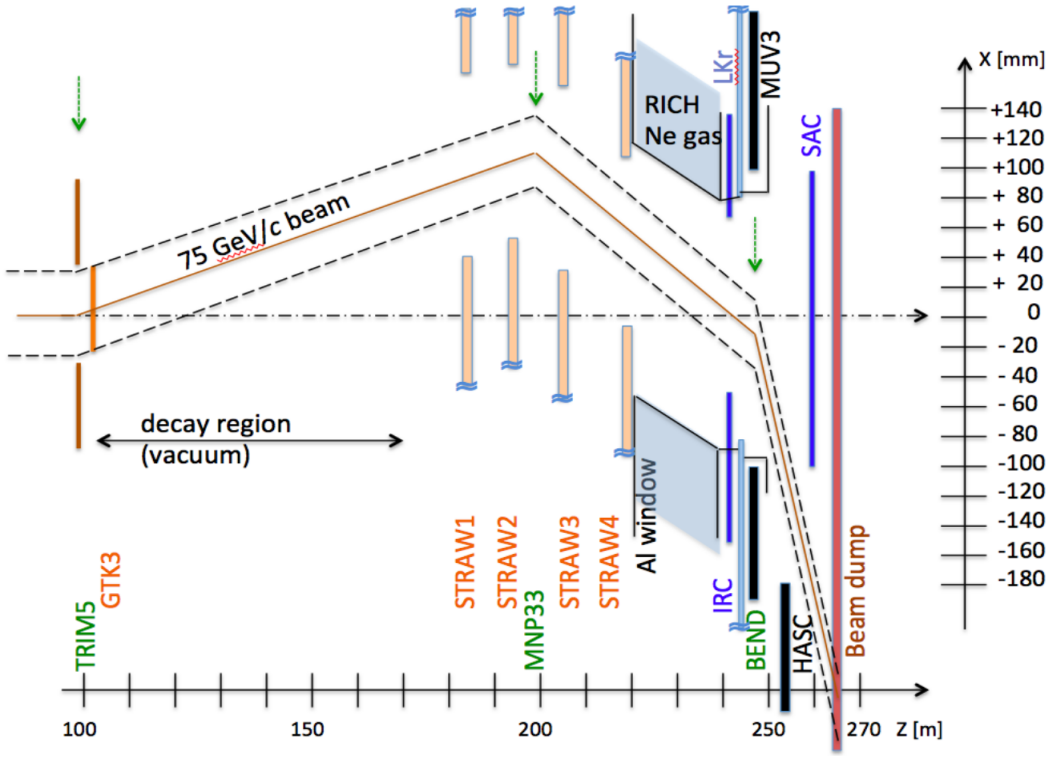

Figure 2.2: Close view of the beam line in the downstream part of the NA62 experiment [45].

having an increasing diameter with distance from the target. They form a photon veto system, together with the electromagnetic Liquid Krypton calorimeter (LKr), the Inner Ring Calorimeter (IRC) and Small Angle Calorimeter (SAC). The system provides hermetic acceptance for photons emitted in the K^+ decays for polar angles from zero up to 50 mrad. A Ring-Imaging Cherenkov counter (RICH) for particle identification, and two plastic scintillator charged hodoscopes (CHOD, CHOD48) are located downstream of the vacuum tank, before the LKr. For further particle identification two hadronic calorimeters and muon veto detector (MUV1,2,3) are placed after the LKr. Additional counters (MUV0, HASC) are installed at optimized locations to provide hermetic coverage for charged particles produced in multi-track kaon decays. After MUV3 the beam is deflected by BEND magnet into the beam dump. The schematic view of the detectors is shown in Figure 2.3. In the following, a more detailed description is given, while the full detector description can be found in Ref. [45] and in the technical design document [46].

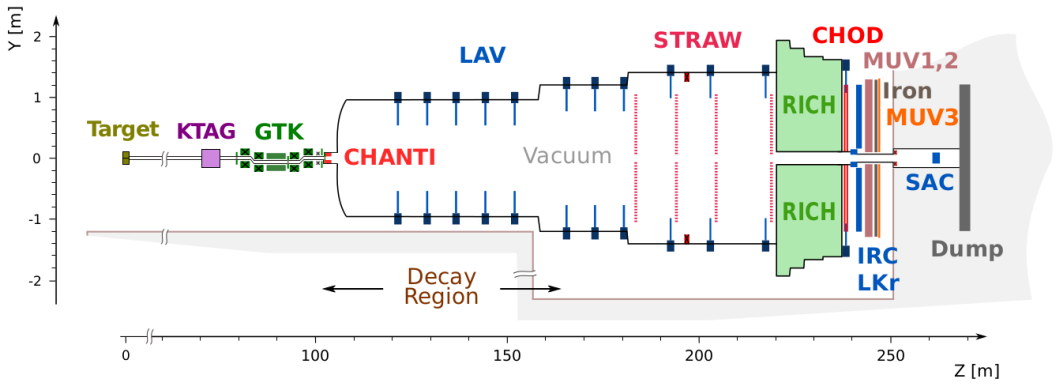

Figure 2.3: Schematic view of the NA62 detectors [45].

2.2.1 KTAG

A Cherenkov differential counter KTAG is a modified CERN W-type CEDAR detector [47]. It is optimized to sustain higher beam rate, provide time resolution at the level of 100 ps, reach the efficiency above 95% and keep the contamination of the kaon sample below 10^{-4} [48]. KTAG is filled with nitrogen gas at 1.75 bar pressure at room temperature. Only a light produced by a beam kaon in the radiator gas can pass through an annular diaphragm and is focused through eight quartz windows onto eight spherical mirrors, equally spaced around the circumference of the diaphragm. The mirrors reflect the light into eight light boxes (sectors), each containing 48 photomultipliers (PM).

The reconstruction of KTAG candidate (kaon) starts with the iterative clustering of hits from different sectors in time within 2.5 ns after they were corrected for slewing. A kaon candidate is reconstructed if at least 5 sectors have at least one PMT signal within 2.5 ns around the average cluster time. On average, 20 hits form the kaon candidate. The measured kaon time resolution in KTAG is 70 ps [49].

2.2.2 GTK

The beam spectrometer GTK is a hybrid silicon pixel detector providing a measurement of momentum to 0.2% relative precision, time measurement with 200 ps hit resolution, and directions dx/dz and dy/dz of the beam at the exit of the achromat to 16 μrad precision. The schematic view of the beam passing the detector is shown in Fig. 2.4. The GTK consists of three stations, each having 18000 pixels of 300×300 μm^2 arranged in a matrix of 200×90 elements. The silicon thickness in each station is limited to about 500 μm, optimized to obtain the desired momentum resolution, to suppress multiple Coulomb scattering and to minimize inelastic scattering of the beam particles in the last GTK station. The latter is a possible source of upstream background as it could mimic an isolated outgoing charged particle from a decay.

The space alignment between the GTK stations is at the level of 100 μm, performed with the sample of $K^+ \to \pi^+\pi^+\pi^-$ decays reconstructed from the STRAW spectrometer. The GTK hits are corrected for slewing and are grouped

in time within ±2 ns with respect to the reference time provided by KTAG and in space by selecting hits in different stations along directions compatible with beam particle trajectories allowed by the beam acceptance [49].

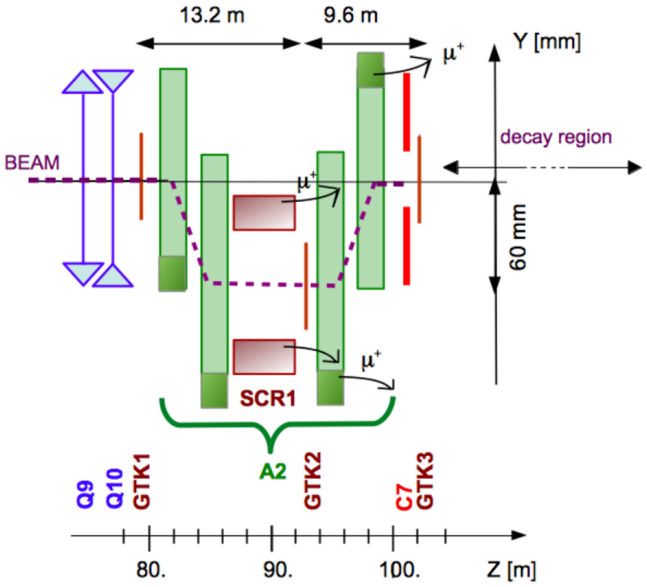

Figure 2.4: Schematic layout of the momentum measurement in the second achromat (A2). The beam arrives to the first GTK station, then it is deflected vertically by 60 mm by two C-shaped dipole magnets. Then it passes through the second GTK station and returns to its nominal direction by another pair of dipoles. Before reaching the third GTK station, the beam crosses the collimators C6/C7 and is deflected by TRIM5. Inside the achromat, there is a toroidally magnetized scraping iron collimator (SCR1) sweeping away muons together with return yokes of the last two magnets of the achromat (dark shaded areas) [45, 46].

2.2.3 CHANTI

The Charged Anticounter (CHANTI) is installed just after the last GTK station, 28 mm downstream, inside the same vacuum vessel. The CHANTI is composed of six stations, each being a square hodoscope with size of 300×300 mm^2 with a 95×65 mm^2 hole in the center to leave room for the beam. Its purpose is to detect the charged particles produced in inelastic interactions of the beam with the last GTK station and collimator, emitted at relatively large angles with respect to the beam. It covers hermetically the angular region from 49 mrad to 1.34 rad. The stations are made of two layers of triangular scintillator bars, 22 in horizontal and 24 in vertical direction, adding to a total of 488 bars. They are read out by wavelength-shifting fibers coupled to silicon PMs on one side of the bar.

The single bar time resolution has been measured to be 1.14 ns and a single layer efficiency is greater than 99% [50]. A CHANTI candidate is defined as a set of the bars within one station where the hits are compatible in time. The time resolution of the CHANTI candidate is 900 ps [49].

2.2.4 Straw Spectrometer

The downstream spectrometer (STRAW) measures the trajectories and momenta of the charged particles originating from the K^+ decays. To minimize multiple scattering, the detector is made of an ultra-light material and is installed inside the vacuum tank, with the total material budget of 1.8% X_0. The detector consists of four chambers and a large aperture dipole magnet (MNP33) in the middle, which provides a horizontal momentum kick of 270 MeV/c. The first chamber is located about 20 m after the decay region, while the last chamber is 35 m downstream the beam line from the first one.

Each chamber is equipped with 1792 straw tubes, oriented in four directions (views) rotated by 45°. The geometry of the straws within the single view is shown in Fig. 2.5. The arrangement of the straws ensures a high detection redundancy, which guarantees at least two hits per view. In each view, there is a 12 cm hole in the center, so the undecayed component of the beam can go through. The hit rate is unevenly distributed within the chamber, with the highest number of hits being around the center.

The straws have diameter of 9.82 mm, they are 2160 mm long and filled with a mixture of Ar and CO_2 gases in 70:30 ratio. They are coated from the inside with copper and gold to ensure a good conductivity and have the gold-plated tungsten anode wires in the middle. The straw tube and the wire are kept at the potential of 1750 V, giving a maximum drift time in the straws of about 140 ns.

STRAW reconstruction

The leading edge of the signal is used to measure the drift time, which gives the lateral position of a crossing track. The trailing edge gives a measurement of the absolute time of a hit, used to group the hits belonging to the same track. The drift time is translated using the GARFIELD [51] simulation into the radius R of the particle trajectory crossing the straw from the anode wire. At least two hits in the consecutive planes within the same view, compatible with the staggering of the planes, form a so-called view-hit. Its position is transformed into the NA62 reference frame applying a pattern recognition algorithm. View-hits are then clustered into the space-points to give the particle position in each chamber. The pattern recognition algorithm groups the space-points into the track segments of chambers 1 and 2 (before the magnet), and 3 and 4 (after the magnet), respectively. It then combines the segments, taking into account the momentum kick of the MNP33 magnet in the XZ-plane. To measure the track parameters, a fit that uses recursive Kalman filter technique is applied [52]. It takes into account the 3-dimensional measured map of the MNP33 magnetic field and the fringe magnetic field between chambers. The χ^2 of the fit is used as one of the quality criteria of the track.

The track momentum resolution is:

$$\frac{\sigma_p}{p} = 0.30\% \oplus 0.005\% \cdot p, \tag{2.1}$$

where p is in GeV/c and the track time resolution is at the level of 6 ns. The angular resolution varies from 60 μrad at 10 GeV/c to 20 μrad at 50 GeV/c momentum.

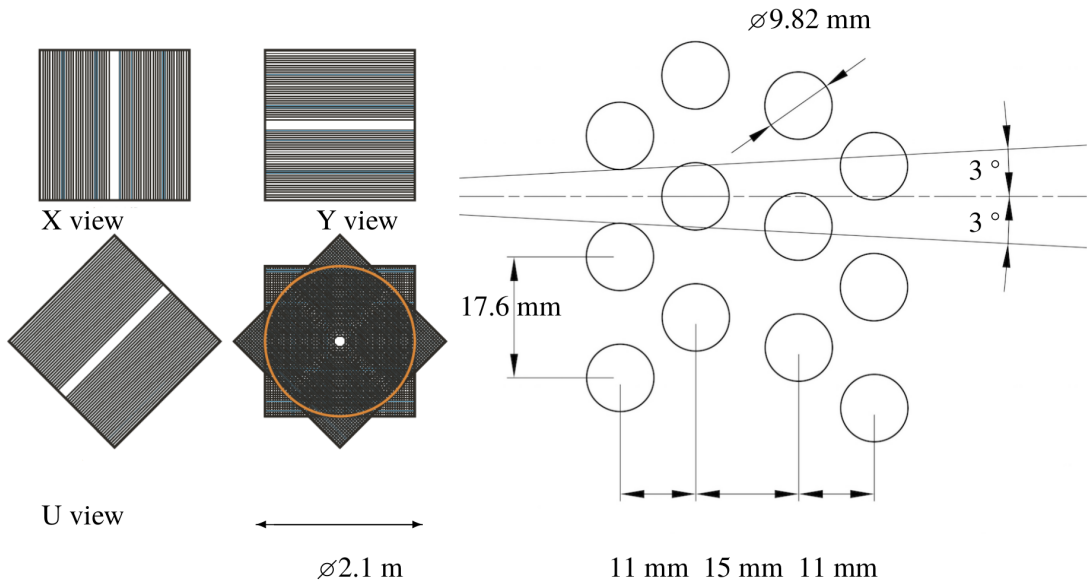

Figure 2.5: Left: Orientations of the views inside the chamber, with the 12 cm hole for the passage of the beam. Right: The arrangement of the straws in a single view. This geometry was chosen to ensure that passing particle will always cross at least two straws per view, as needed to resolve the left-right ambiguity. The 3°angle represents the angular range of tracks produced in kaon decays and detected within the geometrical acceptance of the spectrometer [45].

2.2.5 LAV

The system of 12 annular large-angle photon vetos (LAV) is a part of the photon veto system of the experiment. It covers the angular region between 8.5 mrad and 50 mrad. They are placed between 120 and 240 m from the target along the beam line, and have an increasing diameter from 2.1 m on the upstream end up to 3.3 m in the downstream region. The first 11 stations are contained inside the vacuum tank, while the last one is located outside vacuum, in between the hodoscopes CHOD and CHOD48.

Radially aligned lead glass crystals, forming an inward-facing ring, are located inside each station. The lead glass crystals have PMs and light guide attached, as shown in Fig. 2.6 together with the arrangement inside the station. The LAV stations have either 5 (first eight station) or 4 rings (last four stations), staggered in the azimuth to provide the complete hermeticity. This geometry ensures that incident particle will cross at least three blocks in the longitudinal direction, with a total minimum effective depth of 21 X_0.

To minimize a random veto due to an accidental rate, the time resolution of the LAVs must be around 1 ns for a 1 GeV photon. To reach the desired resolution, the slewing correction extracted from the hit charge is needed. However the charge of the hit is not measured, as only the time over threshold is recorded, which is still affected by the slewing in the leading edge of the signal. To overcome this problem, the signals are recorded at two thresholds and the resulting correct hit time is:

$$T_0 = T_L - L_{THR} \cdot \frac{T_H - T_L}{H_{THR} - L_{THR}}, \tag{2.2}$$

where H_{THR}, L_{THR} are the values of high and low thresholds in mV and T_H, T_L

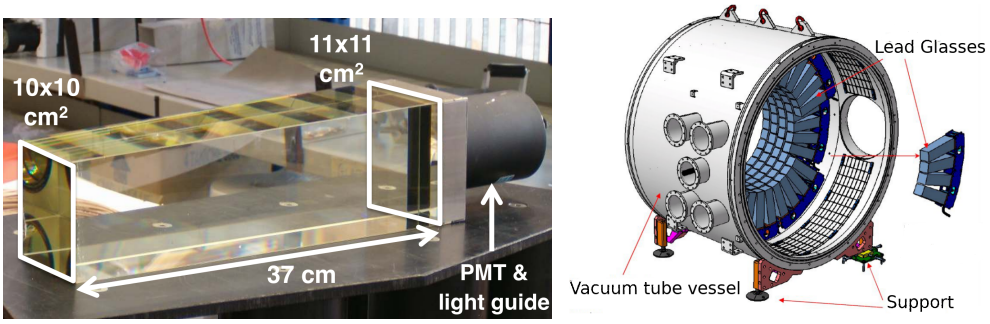

Figure 2.6: Left: The lead glass crystal with attached PM and light guide [45]. Right: The schematic drawing of the LAV station [46].

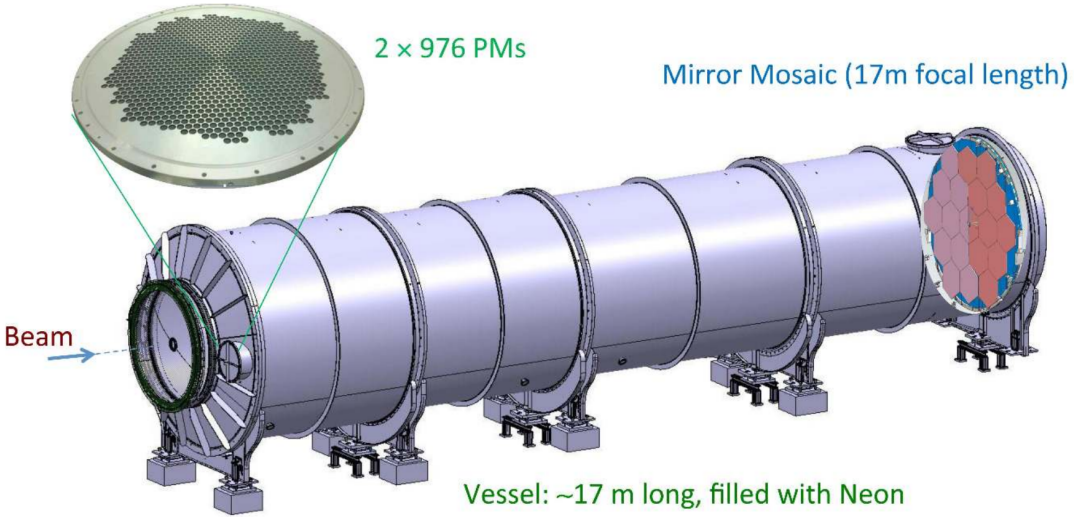

Figure 2.7: The schematic view of the RICH detector [45].

are the corresponding crossing times of the leading edge [46].

2.2.6 RICH

The Ring Imaging Cherenkov counter (RICH), following the vacuum tank, is used primarily for π/μ separation in the $15-35$ GeV/c momentum range . It is made of 17 m long structural steel vessel, divided in 4 cylindrical sections of decreasing diameter (from 4 m to 3 m in the direction of the beam) and different lengths. In the middle a beam pipe with a diameter of 16.8 cm is placed transporting the undecayed component of the beam in the vacuum. The vessel is filled with 200 m^3 of neon gas with a small over-pressure with respect to the atmospheric one (refractive index $(n-1) = 62.8 \times 10^{-6}$), corresponding to the Cherenkov threshold for pions $p_{thr} = m/\sqrt{n^2-1} \simeq 12.5$ GeV/c. The Cherenkov light cone is reflected by a mosaic of 20 spherical mirrors, located on the downstream end of the vessel, to two disks (left and right), with 976 PMs each, on the other end of the vessel. The two disks design, one on the left side and one on the right side, is chosen to prevent light absorption in the beam pipe. The schematic view of the detector is shown in Fig. 2.7.

The measurement of resolution was performed using a positron sample reconstructed from the $K^+ \to \pi^0 e^+ \nu_e$ events, fully in the RICH geometrical acceptance.

The positrons were chosen, since the momentum dependence for e^+ momenta above 10 GeV/c is negligible. The positron passing the detector gives on average 13.8 hits and the ring radius is $R_e = 189.6$ mm with $\sigma_{R_e} \simeq 1.47$ mm. The single hit space resolution is 4.7 mm and the ring time resolution is 70 ps.

The RICH is one of the detectors providing information for the level-0 trigger (see section 2.3.1), with an efficiency higher than 99%.

2.2.7 CHOD

The charged hodoscope (CHOD) detects charged particles passing through its 152 scintillator tiles (of 30 mm thickness along the z axis) arranged in four quadrants. The CHOD detector is symmetric with respect to the beam axis and has a single layer of tiles mounted on a common frame. The tiles are arranged in rows mounted in alternating pattern on different sides of the frame with 1 mm overlap. This reduces the probability of a signal transfer from one tile to another and provides an opportunity to bring the signal reading WLS fibers out to the detector periphery, where the signal is read out with silicon PMs. The tiles differ in size to ensure the consistency of count rates per channel. Smallest tiles with a size of 134×108 mm^2 are located in the central region with the highest count rate, while the larger tiles with a size of 268×108mm^2 are at the periphery, where the count rate is much lower.
The time resolution is at the level of ~ 600 ns and a detection efficiency $\sim 98\%$ [53].

The CHOD is a part of the level-0 trigger system (see section 2.3.1).

2.2.8 NA48 CHOD

The NA48 CHOD (CHOD48) is also a charged hodoscope inherited from the NA48 experiment, placed 80 cm in front of LKr. It is made of 128 scintillator slabs in two perpendicular planes (64 vertical and 64 horizontal), whose lengths vary from 60 cm (outer slabs) to 121 cm (inner slabs). Their thickness is 2 cm and their width is either 6.5 cm in the central region, where the flux is higher, or 9.9 cm at the periphery. The planes are subdivided into 4 quadrants, each having 16 slabs as shown in Fig. 2.8. The slabs are read out on each side by the PM, collecting light via a Plexiglas light guide.

The CHOD48 is provides a track time resolution at the level of 200 ps.

The signals from CHOD48 are used to generate the control trigger (see section 2.3.1).

2.2.9 MUV0

The MUV0 is a peripheral detector attached on the downstream flange of the RICH, perpendicular to the beam, on the positive X side. It is a charged hodoscope aiming to detect negative pions from $K^+ \to \pi^+\pi^+\pi^-$ decays with momentum below 10 GeV/c, deflected towards positive X by the spectrometer magnet and leaving the geometrical acceptance of downstream detectors.

The MUV0 detector consists of 48 tiles of 20 mm thick plastic scintillator tiles (20×20 cm^2) grouped in 9 super-tiles forming a pattern shown in Fig. 2.9. The

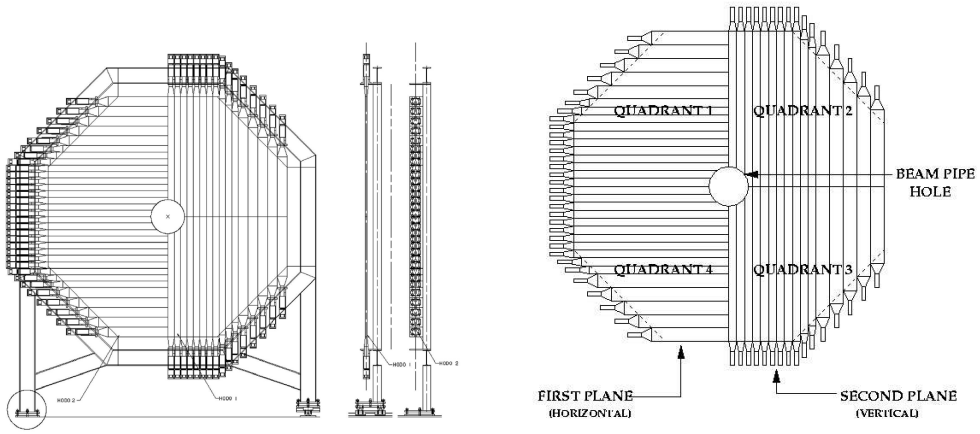

Figure 2.8: Schematic sketch of the CHOD planes [45].

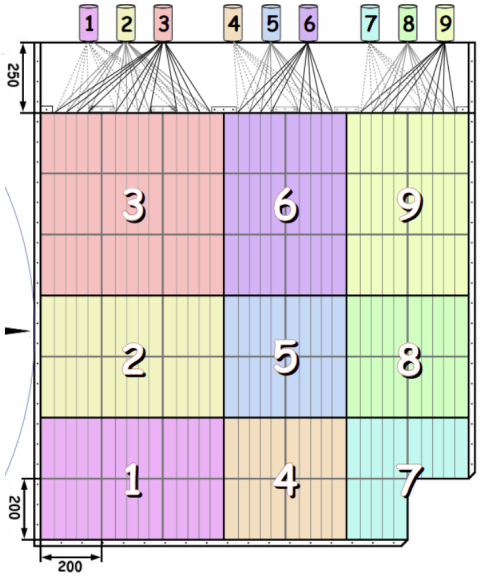

Figure 2.9: The schematic sketch of the MUV0 detector. The arrow on the left indicates the position of the RICH vessel [45].

light output of the 9 super-tiles is brought via bundles of WLS fibers to PMs (same type as for RICH).

2.2.10 IRC

The Intermediate Ring Calorimeter (IRC) encircles the beam pipe in front of the LKr, see Fig. 2.10. It is designed to detect photons emitted at small angles (0-1 mrad) and hence out of the LKr geometrical acceptance. Due to the proximity of the beam pipe, a high rate of muons from beam particle decays is present in IRC, inducing a non-negligible probability of random vetoing $\pi\nu\nu$ signal events due to accidental activity. The IRC is a shashlyk type calorimeter with lead and plastic scintillator ring-shaped plates, with total depth of 19 X_0, traversed by WLS fibers connected to four PMs.

The detector read-out consists of two independent chains. The first one is a

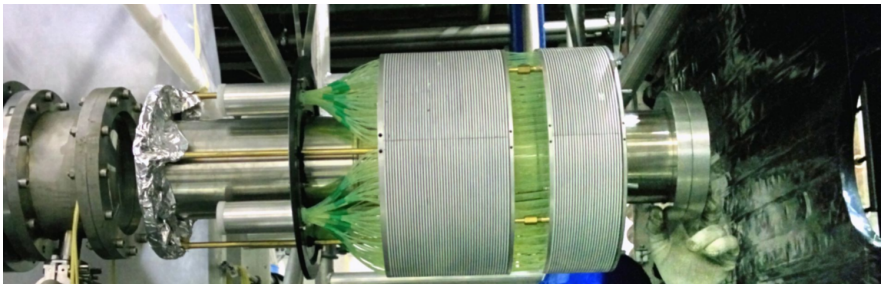

Figure 2.10: IRC detector installation in front of the LKr cryostat (left side), prior to wrapping in black paper for light tightness [45].

TDC (time to digital converter) based module, measuring the time over threshold with a double threshold setting, used also for the LAV modules. The other one is a FADC (fast analog to digital converter) module, the same as used for LKr.

The time resolution of IRC is around 1.6 ns for muons and around 1 ns for photons.

2.2.11 LKr

The Liquid Krypton calorimeter is a quasi-homogeneous electromagnetic calorimeter that measures energy, time and position of impinging electromagnetic particles. It is a part of photon-veto system, covering angles between 1 and 8.5 mrad. Its active volume is 127 cm long, it has an octagonal shape and is filled with 9 m^3 of liquid krypton. The total radiation length is 27 X_0, which is covering 50 GeV shower at the level of 99%. The passive material of the cryostat in front of the active region adds $\sim 0.65X_0$, corresponding to 50 MeV loss in reconstructed photon energy. The inner part is subdivided into 13248 (2×2 cm^2) cells, each having a ribbon made of Cu-Be-Co (98%-1.8%-0.2%) alloy serving as a cathode. The ribbons are installed with a projective geometry from a point 90 m upstream the LKr front face to ensure a higher accuracy of the measurement of the angles between electromagnetic showers. They are installed with the so called accordion geometry (see Fig. 2.11) to keep the inefficient ionization from the showers developing along them at the minimum level. The stability of the ribbons is secured by five spacer plates installed in the longitudinal direction, giving them a a zig-zag shape along the beam axis, as shown in Fig. 2.12 This fitting assures a local positioning precision at the level of 50 μm. In 2017, there were 94 permanently bad cells, mostly caused by hardware problems. More than a half of them are placed on top of the LKr, out of geometrical acceptance of other detectors. Another 45 cells are marked bad due to their inadequate response, which can be caused by the oscillations in the read-out electronics chain or bad connection of the signal cables.

LKr reconstruction algorithm

The reconstruction program is building hits, assigning them an energy and time from the calibration constants and subtracts the pedestals (an offset of the pulse). It then builds clusters from the hits and calculates the cluster energy and position. It treats the dead cells and splits the clusters with more than one seed, evaluating

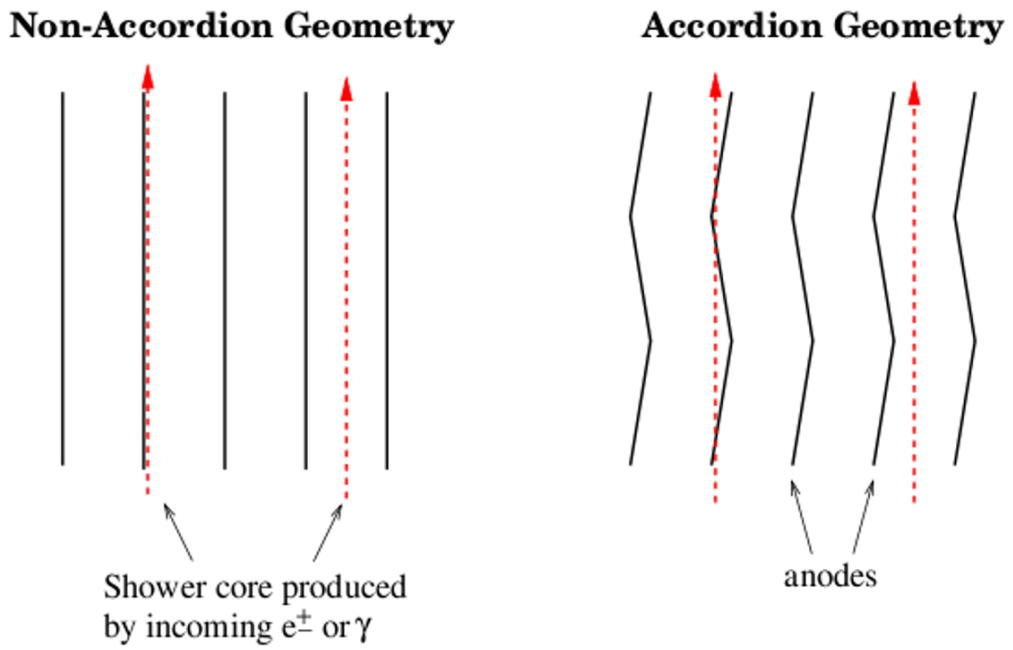

Figure 2.11: The accordion geometry of ribbons inside the LKr.

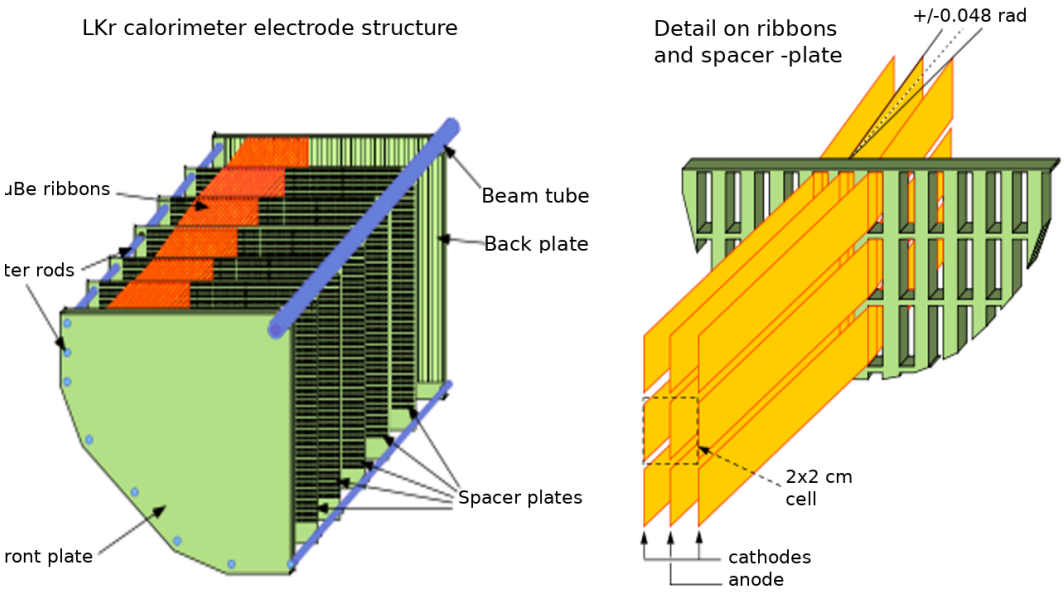

Figure 2.12: Position of spacers in the LKr used to assure stability and permanent tension of about 20 N of ribbons [45].

a correct energy sharing. It contains the following steps (simplified):

- checking the cell status - discarding dead cells;
- selecting cluster seed candidates: E_{hit} >0.25 GeV and $E_{seed} > (0.18 + 1.8 \cdot E_{ave})$, where E_{ave} is the average energy of the surrounding cells;
- estimating the cluster position from 3×3 (5×5 if there is a dead cell next to the seed) box of cells with the cluster seed in the center, using the barycenter of the energy deposition;
- getting a rough estimate of cluster energy;
- the cluster time is defined as the time of the seed;
- checking each cell, whether it belongs to more than one cluster (checking for cluster seeds in 19×19 cells around);
- computing the cluster energy:
  - if there is only one cluster, add energies of all cells within 11 cm cluster radius to that cluster;
  - if the cell belongs to more than one cluster, apply the energy sharing:

$$E_i = E_{cell} \frac{W_i}{\Sigma W_i},$$

    where W_i is the expected energy in the cell from the cluster i in the cell.

The energy resolution is:

$$\frac{\sigma(E)}{E} = \frac{0.032}{\sqrt{E}} \oplus \frac{0.09}{E} \oplus 0.0042; \quad E \text{ in GeV}, \tag{2.3}$$

which corresponds to $\sigma(E) \approx 142$ Mev for $E = 10$ GeV [54].
The space resolution is:

$$\sigma_x = \sigma_y = \frac{0.42}{\sqrt{E}} \oplus 0.06 \text{ cm}, \tag{2.4}$$

corresponding to $\sigma_x = \sigma_y \approx 1.5$ mm for $E = 10$ GeV [54].

Simplified LKr signals are used as an input for the level-0 trigger (see section 2.3.1).

2.2.12 MUV1

The MUV1 detector is the first of the set of muon veto detectors seen by the beam. It is placed right after LKr and is succeeded by MUV2, iron wall and MUV3 detectors, see Fig. 2.13.

MUV1 is a hadronic calorimeter made of 24 layers of iron (2.7 cm thick) and 23 layers of scintillator (0.9 cm thick). The layers follow an alternating horizontal and vertical alignment pattern, resulting in 12 layers with horizontal and 11 layers with vertical strip direction. In each scintillator layer there are 44 strips, 6 cm wide and read-out at both ends through the WLS fibers by PMs, except the central region through which the beam pipe passes, where the flux of particles is higher and the PM is only at one side of the strip.

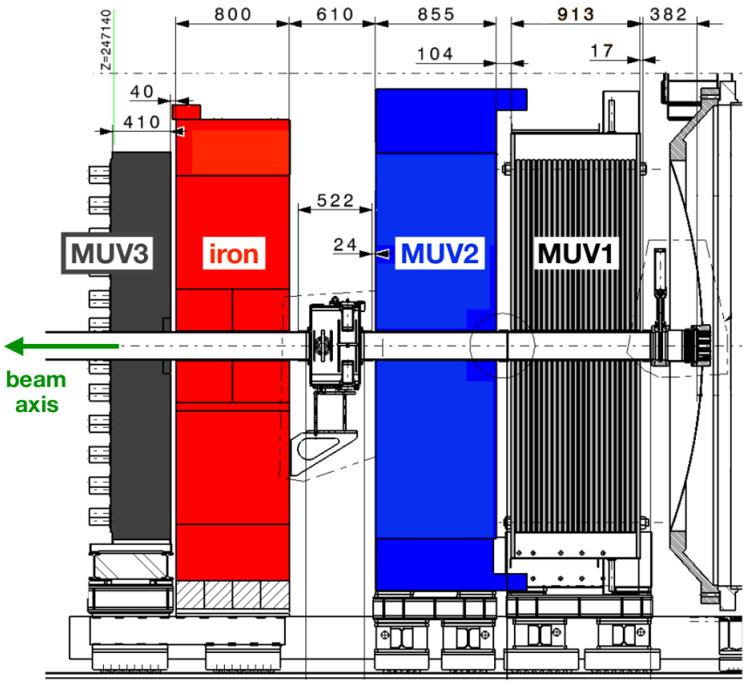

Figure 2.13: Schematic view of the muon veto detectors. First two, MUV1 and MUV2, are hadronic calorimeters, then followed by 80 cm iron wall and the fast scintillator detector MUV3 [55].

2.2.13 MUV2

The MUV2 is also a sandwich calorimeter with 24 iron plates of 25 mm thickness interleaved with scintillator (0.45 mm thick). There are 2×22 strips, 12 cm wide, spanning over a half of detector in each scintillator layer. Again, an alternating horizontal and vertical alignment in consecutive planes is applied. The light is collected to the PM through the light guide, directly attached to the strip.

The energy resolution is:

$$\frac{\sigma\left(E\right)}{E} = 0.115 \oplus \frac{0.38}{\sqrt{E}} \oplus \frac{1.37}{E} \quad E \text{ in GeV}. \tag{2.5}$$

The time resolution with the value 0.9 ns was measured with sample of muons from $K^+ \to \mu^+\nu$ decays, with respect to CHOD48.

2.2.14 MUV3

The fast muon detector MUV3 sits behind 80 cm thick iron wall (see Fig. 2.13). The purpose of the iron wall is to absorb all residuals of hadronic showers from calorimeters before, so only the muons can reach MUV3. The MUV3 is made of 148, 5 cm thick scintillator tiles. Out of them, 140 are regular tiles of $220 \times 220\text{mm}^2$ transverse dimensions, while the innermost region is occupied by 8 smaller tiles due to higher particle rates. Each tile is simultaneously read out by two PMs to suppress possible erroneous signals from Cherenkov radiation of particles crossing a PM window (see Fig. 2.14). The PMs are inside a light-tight box to avoid cross talk between tiles and the distance between the scintillator and

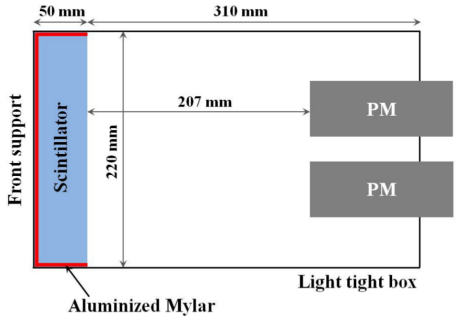

Figure 2.14: Profile view of MUV3 cell, with scintillator tile and two PMs inside a light tight box [45].

the PM windows is 207 mm. The PM bases in the central region are equipped with Zener diodes to allow for more current in the voltage divider, if needed. This is achieved by using an additional -800 V power supply feeding the last three PM base stages. The extra power supply is connected to 24 bases near the beam pipe (the 16 PMs of the 8 cells adjacent to it, and 8 additional PMs on the negative X side), to help withstand high current loads during the beam spill. The MUV3 PM signals are fed to 20 Constant Fraction Discriminators (CFD) to provide optimal time resolution with no slewing (no dependence of the CFD output time on the input signal amplitude).

The MUV3 candidate is reconstructed if there is a coincidence (5 ns) of two PMs in the same tile (tight candidate) or if there is a single PM signal (loose candidate). The time of a tight candidate is defined as the latest of the two hit times. This definition is necessitated by the possibility of a muon hitting a PM window, generating a Cherenkov light that is about 2 ns before the light from scintillator.

The time resolution is in the 0.4-0.6 ns range and the muon identification efficiency measured on halo muons exceeds 99.5% for muon momenta above 15 GeV/c.

The MUV3 detector also provides fast level-0 trigger signals 2.3.1.

2.2.15 SAC

This detector is located at the end of experimental hall, registering the neutral particles from kaon decays flying inside the beam pipe. The charged particles are deflected by the bend dipole just after MUV3 into the beam dump (see Fig. 2.2). Therefore, only neutral particles, including photons from kaon decays reach the SAC detector. The SAC is a shashlyk type calorimeter with 70 layers of lead and 70 layers of plastic scintillator plates traversed by WLS fibers connected to four PMs.

The readout is the same as for IRC, composed of two independent chains.

The energy resolution was measured to be:

$$\frac{\sigma(E)}{E} = \frac{8.8\%}{\sqrt{E}} \oplus \frac{7.1\%}{E}, \quad E \text{ in GeV}, \tag{2.6}$$

and the inefficiency 3×10^{-5} for 25 GeV electrons.

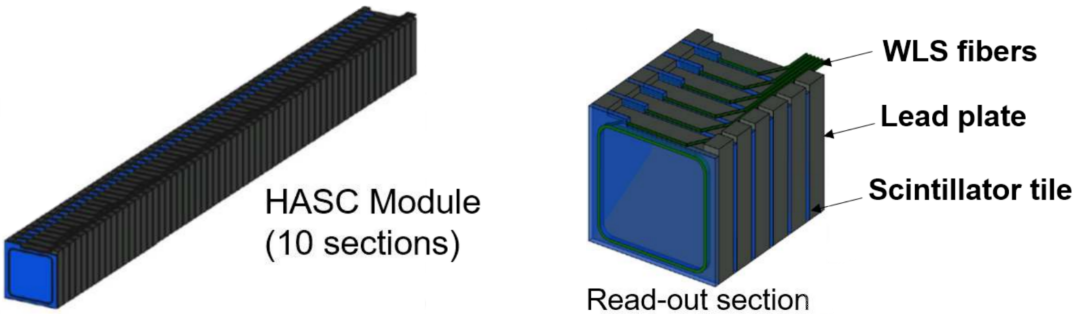

Figure 2.15: One HASC module made of 60 scintillator and 60 lead plates (left) and one read out section made of 6 scintillator plates interleaved with lead (right) [45].

2.2.16 HASC

One of the possible backgrounds to $\pi\nu\bar{\nu}$ is from $K^+ \to \pi^+\pi^+\pi^-$ decays, where one of the positive pions flies inside the beam pipe and the negative pion is not detected. To detect this kind of events, a small hadronic sampling calorimeter (HASC) is attached to the beam line (towards negative X coordinate) in front of the beam dump. As these pions have lower momentum than the beam, they are deflected more by the bend dipole after MUV3 and thus hit HASC. The HASC consists of 9 identical modules, each being a sandwich of 60 lead (16 mm thick) and 60 scintillator plates (4 mm thick) of 100×100 mm^2 transverse dimensions. One read-out section is made of six consecutive scintillators, so one module has 10 sections (see Fig. 2.15). Each section is connected to one optical fiber read out with a SiPM, whose time over threshold signal is sampled with 4 thresholds.

2.3 Trigger

The intense flux of particles in NA62 experiment requires a high-performance trigger. It has to reduce the event rate of ~ 6 MHz to about 3×10^5 events/spill written on tapes. In 2017 the trigger was segmented in two levels: level-0 (L0) and level-1 (L1). Level-2 trigger was not used during 2017 data taking.

2.3.1 Level-0 trigger

The L0 is a hardware trigger, receiving a simplified information, called trigger primitives, from a set of detectors. The trigger primitives are 64 bit words containing the time and detector-specific information. After the L0 trigger processor receives the primitives, it makes a decision based on a set of predefined conditions (trigger masks). The detector-specific primitives relevant for $\pi\nu\nu$ analysis in 2017 were:

- Q1: a primitive is issued by NA48 CHOD, if a charged particle crosses the horizontal and vertical slabs in coincidence. Q1 trigger was used as a control trigger useful for trigger efficiency calculations and for the normalization.
- RICH: a primitive is generated when at least 4 SuperCells are in coincidence, where SuperCell signal is computed from the output of 8 channels digital

adders.

- CHOD: a primitive is generated if there is at least one and no more than four hits in the detector.
- QX: a primitive is present if at least two diagonally-opposite quadrants in CHOD are hit.
- LAV12: tags events with activity inside the last LAV station and generates the primitive if the event contain signals from one or more LAV12 blocks.
- MUV3: tags events with muons. The primitive is generated if there is any hit in MUV3.
- UTMC: the primitive is generated in the CHOD detector if the event satisfies the upper tight-hit-multiplicity cut (event has less than 5 tight hits), where the tight hit is defined as a coincidence of both PMs of the tile.
- CALO: the primitives are based on the super-cells corresponding to 4×4 LKr cells. The CALO trigger primitive contains the information about the energy and number of clusters.

The trigger mask1, used to record $\pi\nu\bar{\nu}$ was defined as:

- RICH & UTMC & !Qx & !LAV12 & !MUV3 & !CALO> 20 GeV up to run number 7977;
- RICH & UTMC & !QX & !MUV3 & !CALO(E> 30||NC> 1) from run 7980 on,

where the exclamation mark means a veto condition. The control trigger defined as Q1 was down-scaled by factor 400.

2.3.2 Level-1 trigger

The L1 trigger is an online software reducing further the event rate to 100 kHz. The $\pi\nu\nu$ relevant L1 triggers in 2017 were:

- KTAG: at least four KTAG sectors are in coincidence and within ± 5 ns of the L0 trigger time;
- LAV: maximum two hits in any of the LAV station within ± 10 ns with respect to L0 trigger time. After run 8025 the LAV1 was removed from L1 trigger;
- STRAW: selects at least one reconstructed track, where the track definition is:
  - longitudinal track momentum is smaller than 50 GeV/c;
  - closest distance of approach to the beam axis is smaller than 20 cm;
  - Z position of the vertex is within 100 m and 180 m;

if a pair of tracks is reconstructed, their mutual CDA must be greater than 30 mm.

The L1 triggers were applied sequentially, after the L0 trigger. A fraction of 2% of the events were recorded through the *autopass* stream, meaning that no L1 cut was applied, only the L1 flag is assigned to the event. For the $\pi\nu\bar{\nu}$ mask *autopass* accounts for 25% of events recorded on tape.

2.4 Data processing

After passing all trigger conditions the data are written to local disks, then copied on the magnetic tapes and stored at the CERN Advanced STORage manager (CASTOR) in the raw data format [56]. The data are collected in the so called runs, where a set of runs defines a data sample. The data sample represents a period of data taking with the same experimental setup. In 2017, four data samples for $\pi\nu\nu$ studies were collected: A, B, C and D. The run has typically 1500 bursts, each burst corresponds to one SPS spill, however shorter runs occur when the data taking conditions change. Next, the data undergo several steps of "Data Processing". During this process, various time alignments, corrections and data quality criteria are applied. These steps, described below in more detail, are necessary to prepare the raw data for the analysis. The data processing is done centrally on the CERN HTCondor batch system.

2.4.1 Time calibration

The first step of the time calibration computes the so-called Coarse T0s, corresponding to a set of channels, based on 100 bursts randomly distributed within the run. During this step the time shift with respect to the trigger time is evaluated for a set of channels of each sub-detector. Next step computes the so called Fine T0s, corresponding to single channels, for KTAG, which provides a reference time for all other detectors. Then a global time offset for spectrometer is calculated, by comparing the sum of hit positions in two consecutive straw planes to the design value. Finally, Fine T0s for all other detectors with respect to KTAG time are produced and applied. Besides of timing related procedures, some other corrections of mis-behaving firmware of LKr are applied.

2.4.2 Reconstruction

With the time calibration in hand, the data reconstruction runs on the raw data files and applies detector specific routines to translate the raw information into the format more suitable for the analysis. The Coarse T0s are redone on the burst-by-burst basis together with the trigger time drift corrections. The reconstruction first constructs the hits in the detectors, which are subsequently used to build the candidates. The standard FORTRAN based LKr clusterization algorithm runs at this step. The reconstruction output files contain root trees and typically occupy double the disk space compared to the raw data.

2.4.3 Data filter

To reduce the amount of data written on the disk and to speed-up the analysis, various data filters run on the reconstructed data. For this analysis, PNN filter stream is used. Only the L0 trigger mask1 ($\pi\nu\bar{\nu}$) and Control trigger enter the the PNN filter sample. For the mask1, to pass the PNN filter, events must satisfy the following conditions:

- no global reconstruction error in any of the detectors;
- no GTK reconstruction errors;
- at least one hit in vertical and one hit in horizontal plane in the same quadrant of CHOD48;
- at least one and less than 10 reconstructed Spectrometer candidates, with at least one fulfilling:
  - hits in all 4 chambers;
  - $\chi^2 \leq 30$;
  - $|p_{beforefit} - p_{afterfit}| \leq 25\text{MeV}/c$;
  - in geometrical acceptance of CHOD48 (125 mm inner radius), CHOD, LKr (145 mm inner radius) and MUV3;
  - horizontal-vertical pair of CHOD48 hits matched;
  - the track should not form a vertex with another good track, where good track has signal in all 4 Straw chambers and $\chi^2 \leq 30$; the vertex is defined as an intersection between the two tracks in the region $[80, 180]$ m, with CDA below 10 mm and with the time difference of the tracks measured by Straw less than 30 ns;
  - track momentum in the range $[8, 50]$ GeV/c;
  - at least one KTAG kaon candidate with at least 4 sectors must be present within ± 5 ns of $T_{CHOD48} = 0.5 \cdot (t_V + t_H)$, where $t_{V,H}$ are the hit times in vertical (V) and horizontal (H) slabs of CHOD48;
  - at least one hit in each GTK station within ± 2 ns of the time of the KTAG candidate associated to the track;
  - no associated MUV3 candidates to the track within ± 4 ns of T_{CHOD48};
  - no standard LKr cluster more than 180 mm away from the extrapolated track position and within ± 5 ns of T_{CHOD48};
  - no hits in LAV in any of the stations within ± 2 ns of T_{CHOD48};
  - a CHOD48 hit pair matching the track, where the condition $D_{C48} \leq 20$ identifies the matching, with

$$D_{C48} = \left(\frac{|\mathbf{X}_{H-V} - \mathbf{X}^{C48}_{track}|}{2\sigma_X}\right)^2 + \left(\frac{T_{CHOD48} - T^{Straw}_{track}}{3\sigma_T}\right)^2 + \left(\frac{t_V - t_H}{3\sigma_t}\right)^2, \tag{2.7}$$

    where $\mathbf{X}^{C48}_{track} = (x, y)$ is the extrapolated position of the track at the CHOD48 H and V planes, $\mathbf{X}_{H-V}$ are the (x, y) H-V hit coordinates in the corresponding slabs and $\sigma_X = 13$ mm, $\sigma_T = 7$ ns, $\sigma_t = 3$ ns are the spatial and time resolutions, respectively;

– the time of the CHOD48 hit pair T_{CHOD48} needs to be within 30 ns with respect to the time measured by Straw.

For the control trigger stream, only events complying with these conditions pass the PNN filter:

- no global reconstruction error in any of the detectors;
- no GTK reconstruction errors;
- at least one hit in vertical and one hit in horizontal plane in the same quadrant of CHOD48;
- at least one track satisfies the following conditions:
  - track reconstructed with all 4 Straw chambers;
  - track within geometrical acceptance of CHOD48 (125 mm inner radius), LKr (140 mm inner radius) and MUV3;
  - a CHOD hit pair matching the track, where the condition $D_{CHOD} \leq 50$ identifies the matching;
  - at least one hit in each GTK station within ± 2 ns of the reference time, where the reference time is the KTAG time if there is a KTAG candidate associated to the track within ± 5 ns of T_{CHOD48}, otherwise is used the CHOD48 track time itself.

A sub-sample of control trigger stream, down-scaled by factor 10, not passing the PNN filter criteria is kept in the filtered data.

At the end of the filtering, the first step of the track momentum corrections is computed.

2.5 Corrections

Track momentum corrections

Spectrometer mis-calibration corrections Each charged particle with momentum (p) and charge (q) is corrected for mis-calibration of the spectrometer:

$$p_{corr} = p\,(1+\beta)\,(1+\alpha p \cdot q)\,, \tag{2.8}$$

where β corrects for the magnetic field mis-calibration and α for the spectrometer mis-alignment as monitored from fully reconstructed $K_{3\pi}$ decays. Mis-calibration of the spectrometer magnetic field is observed as an offset to the K^+ reconstructed masses.

Blue tube correction The momentum of track is corrected for the residual magnetic field, mostly originating from the Earth's magnetic field, present in the vacuum tank. The tank is painted in blue color, hence the name "blue tube". The blue tube field has been mapped using a Hall probe. The effect of the blue field correction on the 25 GeV/c track corresponds to $\Delta\theta \sim 35$ μrad in direction of deflection and the transverse momentum kick at the level of 0.875 MeV/c.

GTK corrections

Different GTK corrections are performed in the following steps:

- comparing reconstructed GTK kaon candidate position (x, y) in the GTK planes with predicted "downstream kaon" from $K_{3\pi}$ decays from STRAW tracks - extrapolating the "downstream kaon" trajectory upstream to the GTK planes accounting for blue tube and TRIM5 magnetic fields;
- comparing reconstructed GTK kaon candidate slopes $(dx/dz, dy/dz)$ depending on position in GTK_3 with the "downstream kaon";
- comparing reconstructed GTK kaon candidate momentum with the "downstream kaon" momentum.

LKr corrections

Corrections are applied to LKr cluster energies and positions. The corrections to cluster energy include corrections for the overall energy scale, non-linearity and energy loss in the beam hole. Two types of LKr energy corrections are centrally calculated during the data processing. Firstly, the overall scaling factor for the charged track energies and secondly the photon cluster energy corrections [57]. The corrections for the charged tracks are obtained from the E/p measurement from the reconstructed K_{e3} events. They are obtained by the condition of E/p for the electron track equals one. This scaling leads to an overestimation of the photon cluster energies, which are independently corrected based only on the PDG value of the π^0 mass. These corrections are calculated from the reconstructed $K_{2\pi}$ events in several steps:

- The symmetric π^0 case, where the condition $|E_{\gamma 1} - E_{\gamma 2}| < 1$ GeV is required. From the $R_S = \dfrac{M^{reco}(\pi^0)}{M^{PDG}(\pi^0)}$ distribution in 1-GeV bins of $E_\gamma = (E_{\gamma 1} + E_{\gamma 2})/2$, the correction as a multiplicative factor R_S is obtained and applied as $E^{true} = \dfrac{E_{reco}}{R_S(E^{reco})}$. The symmetric case works only in the energy range (10-30) GeV.
- The asymmetric π^0 case takes one photon cluster, supposingly corrected in the previous iteration, and predicts an energy of the second cluster: $E^{exp}_{\gamma 2} = \dfrac{(Z_{LKr} - Z_{vertex})^2}{D^2} \cdot \dfrac{(m^{PDG}_{\pi^0})^2}{E_{\gamma 1}}$, where Z_{LKr} is a z coordinate position of the front face of LKr, Z_{vertex} is a z coordinate of the reconstructed $K_{2\pi}$ vertex and D^2 is a distance between the clusters in LKr. The multiplicative factor $R_A = E^{reco}_{\gamma 2}/E^{exp}_{\gamma 2}$ is obtained from the Gaussian fit of R_A distribution in each 1 GeV bin of $E^{reco}_{\gamma 2}$. Finally the seventh order polynomial fit is performed to get $R_A(E^{reco})$, therefore $E^{true} = E^{reco}/R_A(E^{reco})$. The asymmetric step is repeated in three iterations, expanding the validity range up to (2-50) GeV.

The effect of the correction is depicted in Fig. 2.16.

These corrections are produced run by run and applied at the analysis level.

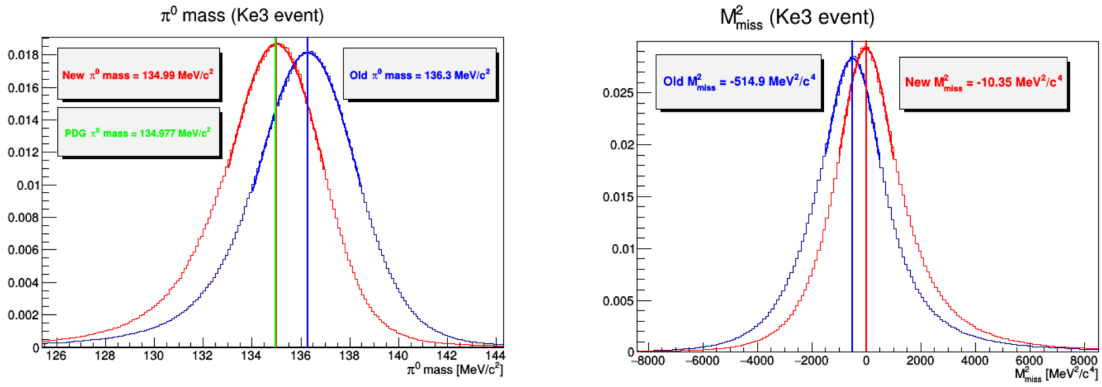

Figure 2.16: Illustration of the LKr corrections based on π^0 mass. Left: The reconstructed π^0 mass before (blue) and after (red) the corrections are applied. Right: Reconstructed missing mass from the $K^+ \to e^+\pi^0\nu$ events before (blue) and after (red) the corrections are applied.

2.5.1 Beam parameters

Beam parameters, defining an average beam estimation, are computed based on the reconstructed $K_{3\pi}$ events.

2.5.2 Data Quality monitoring

The last step is running the data quality analyzers, whose output is used to define the bad bursts for each sub-detector. The bad bursts can be optionally skipped at the analysis level.

3. Analysis procedure

3.1 Analysis strategy for $K^+ \to \pi^+ \nu\bar{\nu}$

The signature of the signal event in the detectors is a single charged track compatible with the pion hypothesis from the particle identification detectors (RICH and calorimeters) and no other activity. In the following, the downstream track will refer to the charged track detected in the detectors after the decay region. The momentum of the downstream track needs to be within the range from 15 to 35 GeV/c, as the RICH has the best performance within this region, see Fig. 4.13. Owing to the 15-35 GeV/c momentum range, the missing energy left is larger than 40 GeV for signal and it can be detected with a high efficiency for background events. The strategy of the analysis is the following:

- applying all the detector and environment (e.g. earth magnetic field) corrections;
- selection of one track events and precise measurement of the squared missing mass, definition of the kinematic regions based on the resolution (precise STRAW tracker pion momentum with GTK kaon momentum matching);
- particle identification based on RICH, MUV3 and calorimetric information ($\pi/\mu/e$ separation);
- powerful ($\mathcal{O}(10^8)$) photon rejection to suppress radiative decays ($K_{2\pi\gamma}$) and ($K_{\mu 2\gamma}$) in the kinematic intervals relevant for signal events;
- study of kaon decays with electrons in final state, determination of the electron rejection;
- definition of signal regions based on the background suppression and detector efficiencies;
- computation of geometrical, detector and analysis acceptances based on MC simulations;
- determination of all background processes and subsequent estimation of their contribution to the signal sample;
- evaluation of systematic uncertainties;
- evaluation of the single event sensitivity and number of expected events.

The so called "Blind analysis" approach is used throughout the analysis to minimize the unintended biasing of the result. The analysis is performed in two kinematic regions to suppress the main background from $K^+ \to \pi^+\pi^0$ ($K_{2\pi}$) and to not to be affected by other abundant decays like $K^+ \to \mu^+\nu_\mu$ ($K_{\mu 2}$) and $K^+ \to \pi^+\pi^+\pi^-$ ($K_{3\pi}$). They enter the signal regions through the non-Gaussian resolution tails and for $K_{2\pi}$, $K_{\mu 2}$ also through the radiative tails of the missing

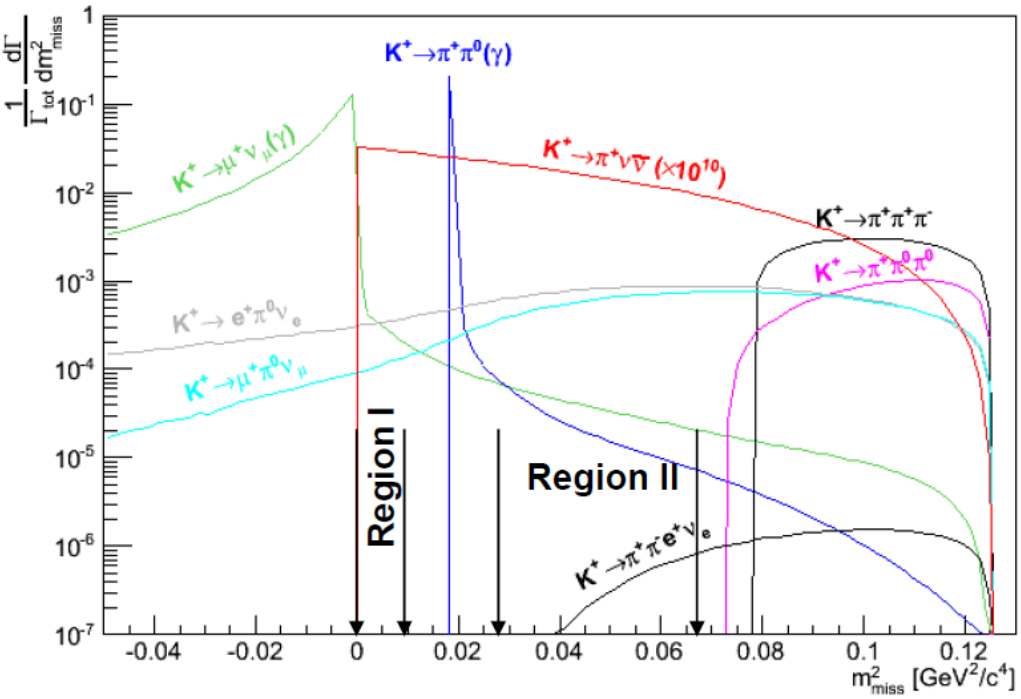

Figure 3.1: Distribution of m^2_{miss} for the signal and background processes. Note that the signal curve is enhanced by a factor 10^{10} [45].

mass. The illustration of various background processes, shown in the context of the missing mass, is in Fig. 3.1, where the missing mass is defined as

$$m^2_{miss} = (P_{K^+} - P_{\pi^+})^2. \tag{3.1}$$

Here, P_{K^+} is a kaon 4-momentum, where the 3-momentum is measured by the GTK and K^+ mass is assumed, and P_{π^+} is a downstream track 4-momentum, where the 3-momentum is measured by the STRAW and the π^+ mass is assumed.

To achieve a sufficient kinematic background suppression ($\mathcal{O}(10^4)$), a precise measurement of the squared missing mass is needed. The Fig. 3.2 is showing the overall m^2_{miss} resolution with the break-down of its contributions:

$$\frac{\sigma(p_{\pi^+})}{p_{\pi^+}} = 0.30\% \oplus 0.0005\% \cdot p_{\pi^+}; \tag{3.2}$$

$$\frac{\sigma(p_K)}{p_K} = 0.2\%; \tag{3.3}$$

$$\sigma(\theta_{\pi^+}) = 20 \div 100\ \mu\text{rad}, \qquad \sigma(\theta_K) = 15\ \mu\text{rad}, \tag{3.4}$$

where p_{π^+}, p_K are the 3-momenta of downstream and upstream tracks and θ_{π^+}, θ_K are the slopes of the momenta vectors with respect to the $Z-$axis measured by the STRAW and by the GTK, respectively. The overall resolution of the squared mass is:

$$\sigma_{m^2_{miss}} = 1 \times 10^{-3}\ \text{GeV}^2/c^4. \tag{3.5}$$

The definition of the $\pi\nu\nu$ signal region is not based only on the kinematic variable m^2_{miss} from GTK-STRAW matching, but also on the variables $m^2_{miss}(RICH)$

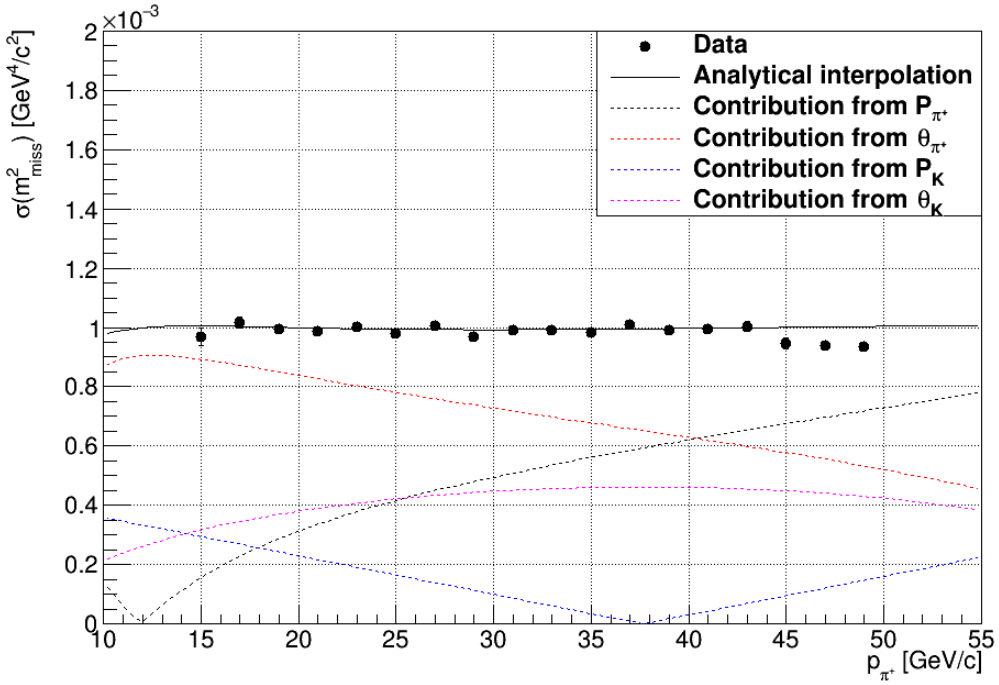

Figure 3.2: Resolution of the squared missing mass as a function of the π^+ momentum with a break-down of the contributions.

and $m^2_{miss}(Beam)$ defined in the following way:

$$m^2_{miss}(Beam) = (P_{Beam} - p_{\pi^+})^2; \tag{3.6}$$
$$m^2_{miss}(RICH) = (P_{K^+} - p_{\pi^+}(RICH))^2, \tag{3.7}$$

where P_{K^+}, p_{π^+} were defined in (3.2), P_{Beam} is a beam nominal 4-momentum (the average $p_{K^+} = 74.9$ Gev/c, $\theta_{K_X} = 1.22$ mrad and $\theta_{K_Y} = 0$ as measured on the $K_{3\pi}$ data sample) and $p_{\pi^+}(RICH)$ is a 4-momentum of the downstream track, where the slopes are obtained from the STRAW and magnitude measured by the RICH, under the π^+ mass assuption. Control regions verifying the background treatment are defined around the signal regions. The specification of signal, control and background regions in the momentum/missing mass plane is shown in Fig. 3.3 and the numerical values can be found in table 3.1. In the table, $m^2_{\mu-kin}$ stands for the analytic expression of the squared missing mass of $K_{\mu 2}$ events, when the π^+ mass hypothesis is made:

$$m^2_{\mu-kin} = \left(m^2_{\pi^+} - m^2_{\mu^+}\right)\left(1 - \frac{75}{P_{\pi^+}}\right); \qquad P_{\pi^+} \text{ in GeV}/c. \tag{3.8}$$

The strategy is to keep the signal regions masked, estimate and check the background in control regions, estimate the background in the signal regions, assert the systematic uncertainties and finaly look at the data in the masked signal regions.

Region	m^2_{miss} [GeV$^2/c^4$]	$m^2_{miss}(Beam)$	$m^2_{miss}(RICH)$
R1 $p_{\pi^+} \leq 20$	(0, 0.01)	(-0.005, 0.0135)	(0, 0.01)
R1 $p_{\pi^+} \in (20, 25)$	(0, 0.01)	(-0.005, 0.0135)	(0, 0.02)
R1 $p_{\pi^+} \geq 25$	(0, 0.01)	(0, 0.0135)	(-0.005, 0.02)
R2	(0.026, 0.068)	(0.024, 0.068)	(0.02, 0.07)
CR1 $K_{2\pi}$	(0.01, 0.015)	-	-
CR2 $K_{2\pi}$	(0.021, 0.026)	-	-
$CR_{K_{\mu 2}}$	$(m^2_{\mu-kin} + 3\sigma,\ 0)$	-	-
$K_{2\pi}$	(0.015,0.021)	-	-
$K_{\mu 2}$	$(-0.05, m^2_{\mu-kin} + 3\sigma)$	-	-
$K_{3\pi}$	> 0.068	-	-

Table 3.1: Definition of two signal regions (R1, R2), two control regions for $K_{2\pi}$ (CR1 and CR2), control region for $K_{\mu 2}$ ($CR_{K_{\mu 2}}$) and background regions for $K_{\mu 2}$, $K_{2\pi}$ and $K_{3\pi}$. Downstream track momentum p_{π^+} is in GeV/c and m^2_{miss}, $m^2_{miss}(Beam)$ and $m^2_{miss}(RICH)$ are defined in (3.2), (3.6), and the missing mass resolution σ is defined in (3.5).

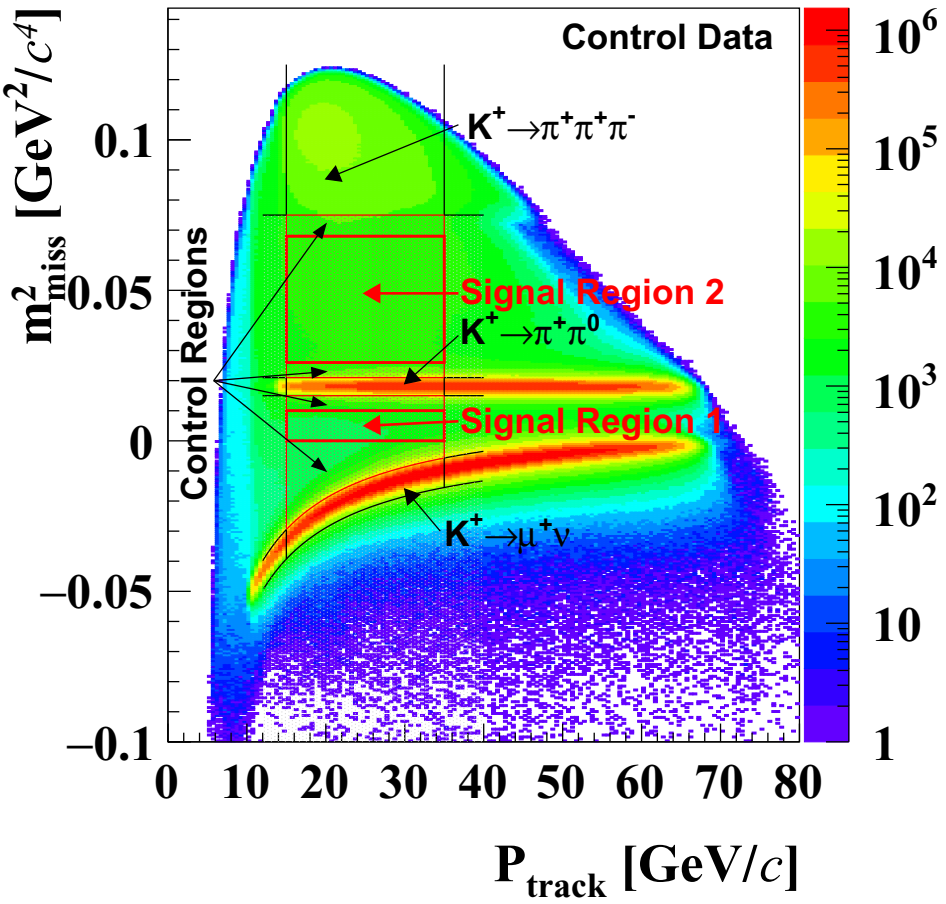

Figure 3.3: Signal, control and background regions marked in the p_{π^+}, m^2_{miss} plane.

4. Event selection

The event selection is performed within the NA62 software framework (na62fw) [58], starting from the filtered data streams. Then a set of the so called Analyzers is used to extract signal and normalization events, employing the output from the Algorithms specific for the sub-detectors. All the Analyzers and Algorithms used in this analysis are in the na62fw git repository, on the PnnAnalysis_RM branch.

4.1 Downstream track - detectors association

The loop over the reconstructed STRAW candidates (downstream tracks) is performed, assigning to each of them the corresponding information from the downstream sub-detectors.

4.1.1 STRAW Selection

There must be at least one good track reconstructed in the STRAW detector. The time correction of -2.1 ns (+1.85 ns) is applied to the STRAW candidates for data (MC). A good track fulfills the following conditions:

- $\chi^2 \leq 20$;
- the momentum difference before and after the fit is below 20 GeV/c;
- the number of chambers (N_{CH}) hit by the track is 4;
- no fake track, where the fake track is defined as track with $N_{CH} = 3$ and at least one of these conditions:
  - there is more than one hit in common with another track;
  - $\chi^2 > 30$;
- the track must be within the sub-detectors geometrical acceptance. The detectors required are: STRAW, CHOD, CHOD48, RICH, LKr, RICH, MUV1, MUV2 and MUV3;
- the event must be outside geometrical acceptance of the last LAV station and IRC.

4.1.2 CHOD48 - STRAW association

The track is extrapolated to the CHOD48 plane and checked against the reconstructed candidates if they match both, in time and in space. The matching is based on the discriminant (D_{CHOD48}) defined in (2.7) and its distribution is shown in Fig. 4.1. The pair of CHOD48 hits (from horizontal and vertical planes) is associated to the track if $D_{CHOD48} < 15$. If there are more candidates matching the track, the one with minimal discriminant is chosen. The time distribution $T_{CHOD48} - T^{STRAW}_{track}$ is shown in Fig. 4.1.

The T_{CHOD48} must be within ± 25 ns with respect to the trigger time to keep the event.

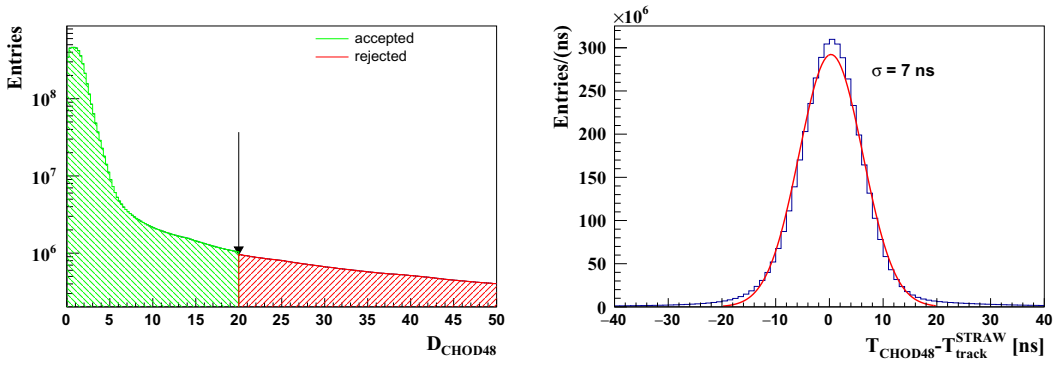

Figure 4.1: Left: The distribution of the CHOD48 discriminant with marked cut. Right: The distribution of the time difference between the CHOD48 candidate and the track time as measured by STRAW; the cut is set at ±20 ns.

4.1.3 CHOD - STRAW Association

For the CHOD - track matching, a standard na62fw tool SpectrometerNewCHODAssociation [58] is used, which provides a geometrical association of CHOD reconstructed hits to STRAW candidates. The track is extrapolated to the CHOD front plane and the geometrical compatibility is determined by the hit tile overlaps with a search circle around the track impact point. The *SearchRadius* is inversely proportional to the track momentum p to account for multiple scattering:

$$SearchRadius\ [\text{mm}] = 6 \cdot \left(0.07 + \frac{47300}{p}\right); \quad p \text{ in MeV}/c, \tag{4.1}$$

where the values in parenthesis correspond to the STRAW resolution $\sigma(x, y) = (0.07 + 47300/p)$ mm. The associated candidate is the tile closest in space to the extrapolated track and its time is the hit time of that candidate. If there are more candidates with the same distance, a single association is chosen randomly.

A discriminant is build based on the time difference between the CHOD candidate time (T_{CHOD}) and the track time measured by STRAW, and the distance of the candidate from the track extrapolation:

$$D_{CHOD} = \left(\frac{|\mathbf{X}_{tile} - \mathbf{X}^{CHOD}_{track}|}{3\sigma_X}\right)^2 + \left(\frac{T_{CHOD} - T^{Straw}_{track}}{2\sigma_T}\right)^2, \tag{4.2}$$

where $\mathbf{X}^{CHOD}_{track} = (x, y)$ is the extrapolated position of the track at the CHOD plane, $\mathbf{X}_{tile}$ represents the (x, y) coordinates of the CHOD candidate tile and $\sigma_X = 16$ mm, $\sigma_T = 7$ ns are the spatial and time resolutions, respectively (see Fig. 4.2). The CHOD candidate matches the track if:

- the discriminant is smaller than 10;
- the CHOD candidate is within ±5 ns of the T_{CHOD48}.

Figure 4.2 shows the discriminant distribution and time difference between CHOD candidate and the track.

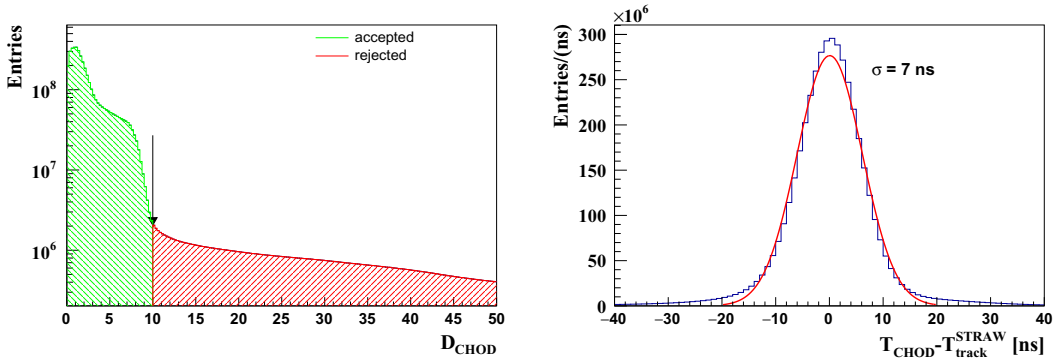

Figure 4.2: Left: The distribution of the CHOD discriminant with marked cut. Right: The distribution of the time difference between the CHOD candidate and the track time as measured by STRAW.

4.1.4 RICH - STRAW association

The RICH - STRAW association is done in two different ways:

- a likelihood-based algorithm assigning each track a probability being e^+, μ^+, π^+, K^+ or a fake track;
- an extrapolated track matching a RICH ring candidate reconstructed with a single ring pattern recognition algorithm.

The likelihood-based algorithm takes a downstream track extrapolated to the RICH, predicting the ring center. Knowing the momentum of the track, it calculates the expected ring radii for every particle hypothesis (e^+, μ^+, π^+, K^+, fake). The algorithm also calculates the expected number of signal hits taking into account ring radius, geometrical coverage of the Cherenkov light on the mirrors and on the PM plane. It looks around the expected ring radius for observed hits (within ±3 ns of the T_{CHOD48}) with Gaussian weights and compares them with the expected number of hits for each hypothesis. The result is a probability of each track being e^+, μ^+, π^+, K^+ or a fake track, where the fake track represents a "dummy" particle (below Cherenkov threshold) accounting for the possible noise.

The single ring algorithm groups the hits in time and fits a ring under the assumption of a single particle passage, with χ^2 of the fit being a quality criterion. The downstream track is extrapolated to the RICH mirror plane, virtually reflected onto the focal plane with the PMs and compared with the reconstructed rings. Each ring is re-fitted, taking into account only the hits within (80, 240) mm from the extrapolated center of the track on the focal plane and within 2 ns of the ring time (T_{RICH}). At least 4 hits must be present, otherwise the ring candidate is discarded. If the fit probability is smaller than 0.005, the hit with the largest contribution to the χ^2 is discarded and the fit is repeated. The track - single ring matching is based on the discriminant:

$$D_{RICH} = \left(\frac{T_{CHOD48} - T_{RICH}}{\sqrt{2}\sigma_T}\right)^2 + \left(\frac{|\mathbf{X}_{center} - \mathbf{X}_{PM}|}{\sigma_X}\right)^2, \qquad (4.3)$$

where $\mathbf{X}_{PM}$ is the (x, y) position of the extrapolated track at the focal plane, $\mathbf{X}_{center}$ is the (x, y) position of the ring center and $\sigma_T = 0.3$ ns, $\sigma_X = 3$ mm

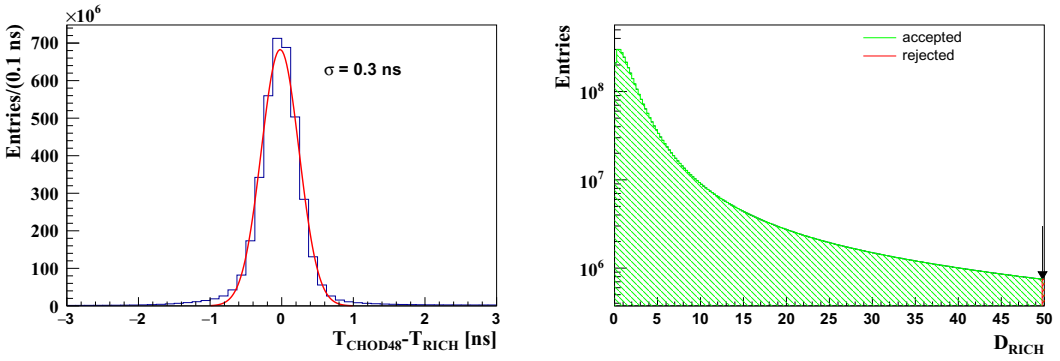

Figure 4.3: Left: Distribution of the time difference between RICH single ring time and CHOD48 time. Right: Distribution of the RICH discriminant D_{RICH}, as defined in eq. (4.3).

are the time and spatial resolutions. The track is matched to the single ring candidate if:

- $D_{RICH} < 50$;
- the fit probability is above 0.01;
- T_{RICH} is within ± 2 ns of T_{CHOD48}.

The time difference of $T_{RICH} - T_{CHOD48}$, together with the discriminant D_{RICH} distribution, are shown in Fig. 4.3.

4.1.5 LKr - STRAW association

Three different methods are used for the LKr signal clusterization:

- The first method (the standard reconstruction) was described in section 2.2.11 and its main features are handling of dead cells and treatment of energy sharing between clusters in time and space. The track extrapolated to the LKr front face is matching a cluster if the cluster time is within ± 5 ns of the T_{CHOD48}, ± 20 ns of the T_{STRAW} and the track impact point is less than 100 mm from the cluster position. The time distributions for cluster time and CHOD48/STRAW times are shown in Fig. 4.4.
- The second method is building the LKr cluster around the impact point of the extrapolated track. The cell energies closer than 100 mm are added to the cluster energy if there is at least one with energy above 40 MeV and if the cells are within ± 20 ns with respect to the STRAW time. The cluster time is defined as a time of the most energetic cell. The new cluster is matched to the track if it is within ± 5 ns of the T_{CHOD48} and ± 20 ns of the T_{STRAW}. This algorithm can recover an efficiency if the first method fails.
- The third method (the auxiliary reconstruction) is building a cluster from geometrically adjacent cells (less than 100 mm apart) if their deposited energy is at least 40 MeV. This method is the most efficient one and it is used for the photon rejection, not for the track-cluster matching.

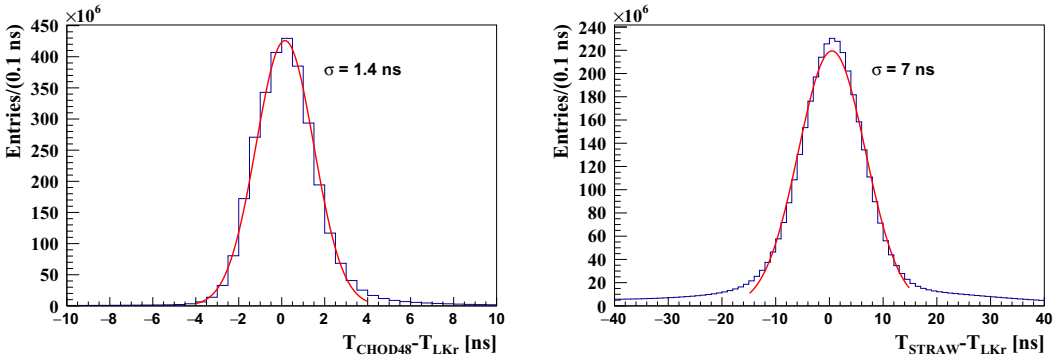

Figure 4.4: The difference between the LKr cluster time and CHOD48 time.

Only events with more than one and less than 2000 LKr hits are considered. The cluster corrections (non-linearity, energy scale, LKr alignment and rotation) are applied to all clusters, regardless of the method. The downstream tracks with associated candidates in LKr, CHOD, CHOD48 and RICH are called the *pion candidates*. The *pion candidate* time is calculated as follows:

$$T_{pion} = \frac{\sum_{i=1}^{3} T_i/w_i^2}{\sum_{i=1}^{3} 1/w_i^2}, \tag{4.4}$$

where i runs over STRAW, CHOD48 and RICH detectors and w_i are the weights related to their resolutions. The weight factors are: $w_{STRAW} = 10$ ns, $w_{CHOD48} = 0.5$ ns and $w_{RICH} = 0.2$ ns. To ensure consistency between the *pion candidate* and the trigger, T_{pion} must be within ± 25 ns of the trigger time.

4.1.6 Calorimetric energy reconstruction

For each *pion candidate*, the information from LKr is combined with the signals in MUV1 and MUV2 to form a calorimetric energy.

The energy reconstruction in MUV1(2) is looking for a seed (strip with largest energy deposit) within 15 cm from the extrapolated track and within ± 20 ns of the horizontal and vertical (views) strip times. If the seed in at least one view is found, it groups all the hits within 7(3) scintillators (40 cm) and within ± 15 ns with respect to the seed position and time, unless two empty strips are found. In the double sided readout scintillators, the energy is the mean of energies recorded by two sides.

A na62fw tool SpectrometerCalorimeterAssociation [58] is used to match the downstream track to the LKr, MUV1,2 and provide a particle identification (PID) based on the Multi-Variate Analysis (MVA). The MVA algorithm [59] is implemented within the ROOT framework [60]. The MVA method used for the PID is Boosted Decision Trees (BDT), because it has the best performance. The training samples of e^+, μ^+, π^+ were obtained from the leading kaon decays $K_{\mu 2}$, $K_{2\pi}$ and $K_{e3}(\mathrm{K}^+ \to \pi^0 e^+ \nu_e)$. The full description of the implementation of the MVA for the PID is given in [55]. For each sample, the following variables are reconstructed and used as an input for the BDT classifier:

- E_{tot}/p where E_{tot} is a sum of energies from LKr, MUV1 and MUV2 associated to the track and p is the track momentum;

- E_{LKr}/p where E_{LKr} is the LKr energy associated to the track with momentum p;
- fractions of energies: E_{LKr}/E_{tot}, E_{MUV2}/E_{tot}, where E_{MUV2} is the energy reconstructed in MUV2;
- Linear Combination of MUV1 and MUV2 weights, defined as a geometrical sum of fractions of energies in single channels with respect to the cluster energy;
- LKr shower RMS $\left(\sqrt{RMS_x^2 + RMS_y^2}\right)$;
- $E_{seed}/E_{cluster}$, where E_{seed} is a cluster seed energy for the LKr and $E_{cluster}$ is its energy;
- $N_{hits}/E_{cluster}$, where N_{hits} is a number of cells in the cluster for the LKr and $E_{cluster}$ is its energy;
- distance between the impact point of the track and cluster position in LKr, MUV1 and MUV2.

The output of the MVA algorithm is the probability that the given track is e^+, μ^+, or π^+. On top of the probabilities, the following variables are used independently of MVA to identify the pion:

- E_{tot};
- the time of the deposited energy, computed as an average of the cluster times in calorimeters;
- Minimum Ionizing Particle (MIP) discriminant:

$$D_{MIP} = \frac{1}{3} \cdot \sqrt{D_{MIP-LKr}^2 + D_{MIP-MUV1}^2 + D_{MIP-MUV2}^2}, \tag{4.5}$$

  where (energies in MeV)

$$D_{MIP-LKr} = (E_{LKr} - 561.3)/(1.5 \cdot 54.9) \tag{4.6}$$
$$D_{MIP-MUV1} = (E_{MUV1} - 1183.8)/(1.5 \cdot 165.8) \tag{4.7}$$
$$D_{MIP-MUV2} = (E_{MUV2} - 1042.5)/(1.5 \cdot 141.1); \tag{4.8}$$

- the extra non-associated energy in MUV1 and MUV2 is within ± 15 ns of the associated energy.

4.1.7 MUV3 - STRAW association

The *pion candidate* has an associated MUV3 candidate if the time of any MUV3 candidate, T_{MUV3}, is within ± 7 ns of T_{pion}.

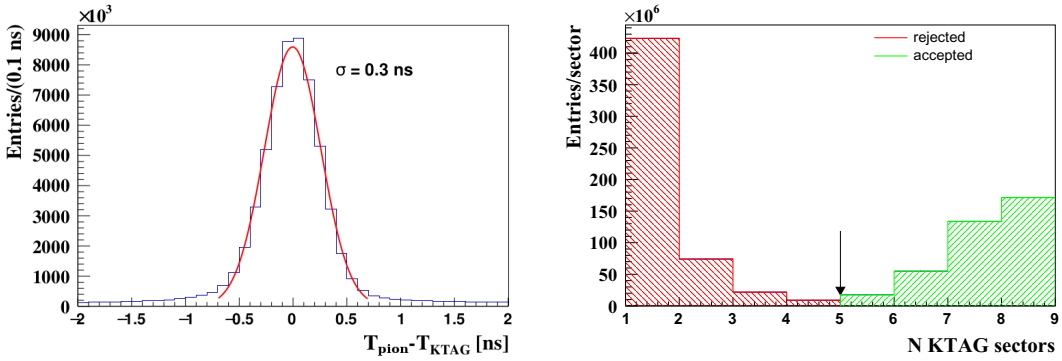

Figure 4.5: Left: The time difference between the KTAG candidate and the *pion candidate*. Right: Distribution of number of active KTAG sectors, with highlighted cut.

4.2 Upstream - Downstream candidate matching

4.2.1 Upstream candidate definition

The upstream candidate must have an in-time signal in KTAG with respect to T_{pion} and a GTK candidate around the reference time provided by the selected KTAG candidate.

KTAG candidate matching

The KTAG candidate must have signal in at least 5 sectors and its time, T_{KTAG}, is the closest in time to T_{pion}. If T_{KTAG} is within ± 1 ns of T_{pion} the KTAG candidate is associated to the *pion candidate*. The distributions of number of sectors and the time difference between KTAG and the *pion candidate* are shown in Fig. 4.5.

GTK candidate

The GTK candidate is reconstructed around the KTAG time of the selected KTAG candidate. First, the spatial alignment to the STRAW reference system is applied to the GTK stations based on the reconstructed $K_{3\pi}$ events. Then, the GTK candidates are built using T_{KTAG} as a reference time by the GigaTracker-RecoAlgorithm [58]. The hits within 10 ns are considered and if the event has more than 100 in-time hits, it is discarded. The in-time hits must be present in each station, giving an upstream track momentum vector. The time of the GTK candidate is a weighted average of times from three stations, where the weights reflect the number of pixels of the hit. The quantity χ^2_T assesses the quality of a GTK candidate timing. Similarly, quantities χ^2_X, χ^2_Y result from a least squared fit to test the consistency of the $x_{1,2,3}$, $y_{1,2,3}$ coordinates with a straight trajectory. The reconstructed momentum needs to fulfill these conditions:

- reconstructed upstream track momentum P_K between 72 and 78 GeV/c;
- slope $\theta_X = dx/dz \in (0.0009,\ 0.0016)$ rad;

- slope $\theta_Y = dy/dz \in (-0.0003,\ 0.0004)$ rad;
- $\chi^2_T < 13.82$.

The GTK candidate must be compatible with the beam kinematics. The beam nominal values are:

- the nominal beam momentum $P_{beam} = 74.9$ GeV/c with the resolution $\sigma_P = 0.9$ GeV/c;
- the nominal beam slope $\theta_X^{beam} = 1.22$ mrad, with the resolution $\sigma_{\theta_X^{beam}} = 0.12$ mrad;
- the nominal beam slope $\theta_Y^{beam} = 0.025$ mrad, with the resolution $\sigma_{\theta_Y^{beam}} = 0.1$ mrad.

The condition $\chi^2_{event} < 20$, where

$$\chi^2_{event} = \left(\frac{P_K - P_{beam}}{\sigma_P}\right)^2 + \left(\frac{\theta_X - \theta_X^{beam}}{\sigma_{\theta_X^{beam}}}\right)^2 + \left(\frac{\theta_Y - \theta_Y^{beam}}{\sigma_{\theta_Y^{beam}}}\right)^2, \tag{4.9}$$

assures the compatibility of reconstructed GTK candidate with the nominal beam values.

CHANTI candidate matching

The CHANTI candidate matches the signal event if there is a coincidence in the horizontal and vertical bars and if it is within 3 ns of any of the GTK, KTAG or *pion candidate* times. The event with matching CHANTI candidate is discarded.

4.2.2 Association of the GTK candidate with the *pion candidate*

The association of the GTK candidate and the *pion candidate* is based on two matching discriminants, taking into account time differences $\Delta T = T_{GTK} - T_{KTAG}$ and $\Delta T_{RICH} = T_{GTK} - T_{RICH}$, and the closest distance of approach (CDA) between GTK and STRAW tracks. The decay vertex is defined as the position of a median point at CDA and the vertex is indicated by the coordinates X_{vertex}, Y_{vertex} and Z_{vertex}. The matching discriminants are:

$$D_1(CDA, \Delta T) = [1 - p(CDA)] \cdot [1 - p(\Delta T)] \tag{4.10}$$

$$D_2(CDA, \Delta T_{RICH}) = [1 - p(CDA)] \cdot [1 - p(\Delta T_{RICH})], \tag{4.11}$$

with

$$p(CDA) = \frac{1}{N_{CDA}^{Norm}} \left[\int_0^{CDA} f(CDA')dCDA'\right]; \tag{4.12}$$

$$p(\Delta T) = \frac{1}{N_{\Delta T}^{Norm}} \left[\int_{-\Delta T}^{\Delta T} f(\Delta T')d\Delta T'\right]; \tag{4.13}$$

$$p(\Delta T_{RICH}) = \frac{1}{N_{\Delta T_{RICH}}^{Norm}} \left[\int_{-\Delta T_{RICH}}^{\Delta T_{RICH}} f\left(\Delta T'_{RICH}\right) d\Delta T'_{RICH}\right]. \tag{4.14}$$

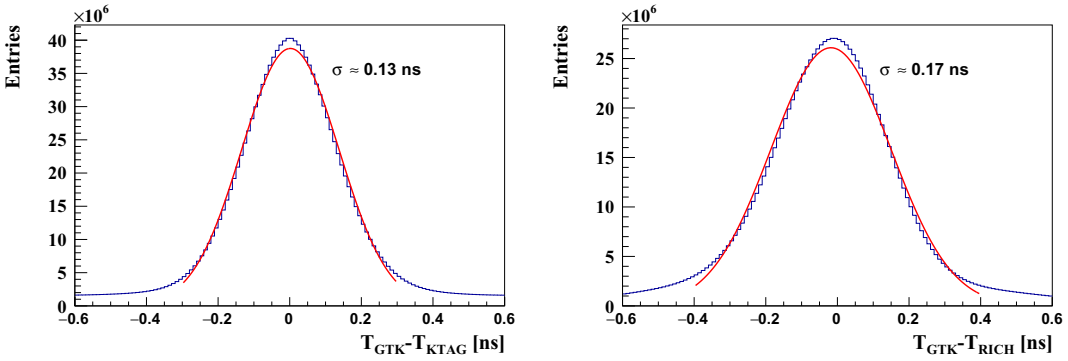

Figure 4.6: The time difference distributions between GTK track time and KTAG (left), RICH (right) candidate times.

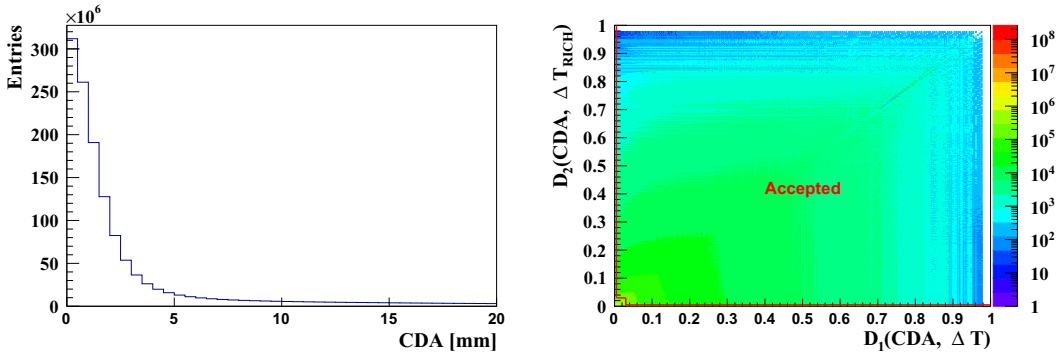

Figure 4.7: Left: The closest distance of approach (CDA) between GTK and STRAW tracks. Right: A 2D plane with discriminants defined in eq. (4.10), with selection cut marked by the red line and highlighted signal region.

The normalization factors N_{CDA}^{Norm}, $N_{\Delta T}^{Norm}$ and $N_{\Delta T_{RICH}}^{Norm}$ are computed in the ranges $CDA \in (0, 100)$ mm and $\Delta T, \Delta T_{RICH} \in (-0.95, 0.95)$ ns. The time difference distributions between T_{GTK} and T_{KTAG}, T_{RICH} are shown in Fig. 4.6. The discriminants and distribution of CDA are shown in Fig. 4.7.

Functions f_{CDA}, $f(\Delta T)$ and $f(\Delta T_{RICH})$ represent the Probability Density Functions (PDFs) for CDA, ΔT and ΔT_{RICH}. The signal template functions are obtained from the reconstructed $K_{3\pi}$ (see Appendix A.2) events and have the following form:

$$f(CDA) = \frac{0.25}{e^{0.5\cdot\left(\frac{CDA}{1.27}\right)^2}} + \frac{0.039}{e^{0.5\cdot\left(\frac{CDA}{2.23}\right)^2}} + \frac{0.0033}{e^{0.145\cdot CDA}} + 0.0000151\cdot CDA - 0.00046 \tag{4.15}$$

$$f(\Delta T) = \frac{0.027}{e^{0.5\cdot\left(\frac{\Delta T}{0.13}\right)^2}} + \frac{0.0017}{e^{0.5\cdot\left(\frac{\Delta T}{0.23}\right)^2}} \tag{4.16}$$

$$f(\Delta T_{RICH}) = \frac{0.026}{e^{0.5\cdot\left(\frac{\Delta T_{RICH}}{0.141}\right)^2}} + \frac{0.001}{e^{0.5\cdot\left(\frac{\Delta T_{RICH}}{0.279}\right)^2}}. \tag{4.17}$$

The pileup template functions are derived from the reconstructed $K_{3\pi}$ events

using the out-of-time GTK hits:

$$f_{pileup}(CDA) = \frac{0.0122}{e^{0.5\cdot\left(\frac{CDA}{5.95}\right)^2}} + \frac{0.0235}{e^{0.5\cdot\left(\frac{CDA}{13.87}\right)^2}} \tag{4.18}$$

$$f_{pileup}(\Delta T) = 3.65 \cdot 10^{-3}. \tag{4.19}$$

Fig. 4.8 shows the distributions of the ΔT and CDA together with the pileup GTK tracks obtained from the $K_{3\pi}$ events by shifting the kaon time by 15 ns. These distributions are used to infer the PDF functions.

Reconstructed GTK tracks are sorted for the increasing discriminant value D_1, with the *kaon track* being the GTK track with the highest D_1 and the *associated tracks* the others. To minimize the probability of matching a pileup track to the *pion candidate* a special treatment is applied to the *kaon track* and the *associated tracks*. Specifically, two probability ratios are defined:

$$R_{CDA} = \frac{1-p(CDA)}{1-p_{pileup}(CDA)}; \tag{4.20}$$

$$R_{\Delta_T} = \frac{1-p(\Delta_T)}{1-p_{pileup}(\Delta_T)}. \tag{4.21}$$

Further, for the *kaon track* (KT) and for the best *associated track* (BA) following ratios are computed:

$$R^{TOT}_{CDA} = \frac{R^{KT}_{CDA}}{R^{BA}_{CDA}}, \qquad R^{TOT}_{\Delta_T} = \frac{R^{KT}_{\Delta_T}}{R^{BA}_{\Delta_T}}. \tag{4.22}$$

Value close to one means that the tracks are very similar. Events are rejected if:

- $R^{TOT}_{CDA} < 1.5$;
- $R^{TOT}_{\Delta_T} < 1.5$.

In addition, if there is only one reconstructed GTK candidate, further requirements on the extra GTK hits are applied. An extra GTK hit is counted if:

- the hit do not belong to the matched GTK track;
- $|X^{station}_{track} - X^{station}_{hit}| > 0.5$ mm;
- $|Y^{station}_{track} - Y^{station}_{hit}| > 0.5$ mm;
- $|T_{GTK} - T_{Hit}| \leq 0.4$ ns.

If the extra GTK hits are present in at least two stations, the event is rejected.

Finally, to associate the *kaon track* to the STRAW track, they must obey these conditions:

- $D_1(CDA, \Delta T) > 0.005$ and $D_2(CDA, \Delta T_{RICH}) > 0.005$;
- $D_1(CDA, \Delta T) > 0.03$ or $D_2(CDA, \Delta T_{RICH}) > 0.03$;
- the time difference between GTK and KTAG is less than 0.6 ns.

The matching efficiency using a *pion candidate* is at the level of 80%. The kaon mis-matching probability estimated from the $K_{3\pi}$ events is around 2% (2.7%) if the kaon is (not) present in GTK and depends linearly on the instantaneous beam intensity. The vertex position, GTK and STRAW momenta are corrected for the blue tube fringe field effect described in section 2.5.

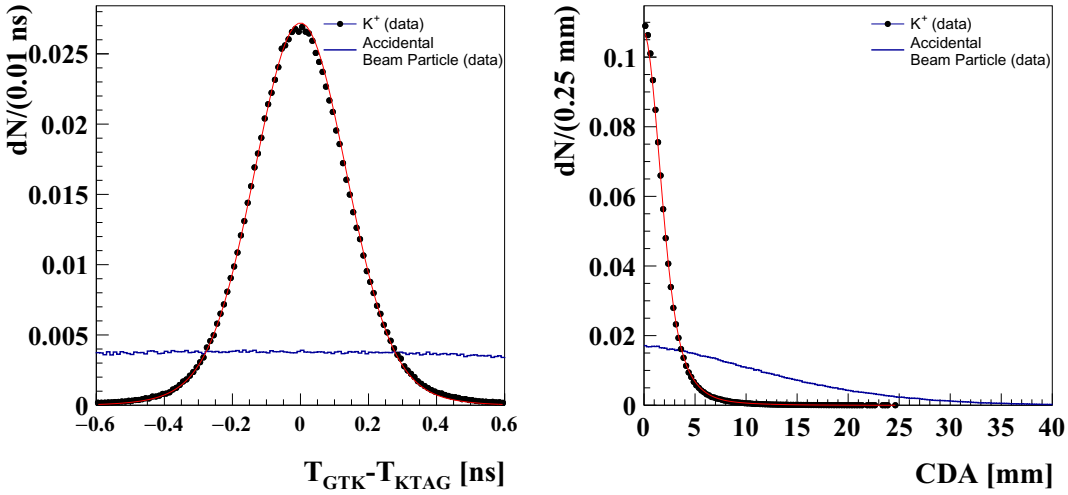

Figure 4.8: Left: Distribution of $\Delta T = T_{GTK} - T_{KTAG}$ for GTK tracks tagged by $K_{3\pi}$ events with the corresponding PDF function, with the same distribution for the pileup tracks using kaon time shifted by 15 ns. Right: Comparison of the CDA distributions for the kaon track and pileup GTK track.

4.3 $\pi\nu\bar{\nu}$ sample selection

The following criteria select the events forming a $\pi\nu\bar{\nu}$ candidate and suppress various backgrounds.

4.3.1 Beam kinematics conditions

An event must have the $Z-$position of the decay vertex within the (105, 165) m range. The beginning of the decay region is chosen at this point to suppress the backgrounds from the early kaon decays. The end of the decay region at 165 m assures a good reconstruction of the downstream track. To ensure the decay vertex compatibility with the beam profile along the decay region, an additional requirement is imposed on the (X_{vertex}, Y_{vertex}) coordinates:

$$X_{vertex} \leq -93.9 + 0.0012 \cdot Z_{vertex}; \tag{4.23}$$
$$X_{vertex} \geq -148.53 + 0.00122 \cdot Z_{vertex}; \tag{4.24}$$
$$Y_{vertex} \leq 3.6 + 0.0000112 \cdot Z_{vertex}; \tag{4.25}$$
$$Y_{vertex} \geq -5.4 - 0.00009464 \cdot Z_{vertex}. \tag{4.26}$$

Fig. 4.9 shows the beam profile at the beginning ($Z_{vertex} = 105$ m) and at the end ($Z_{vertex} = 165$ m) of the decay region.

To retain the event, it needs to have:

- upstream candidate momentum $P_K \in (72.7, 77.2)$ GeV/c;
- $\theta_{ellipse} \leq 0.00035$; $\theta_{ellipse}$ is:

$$\theta_{ellipse} = \sqrt{(\theta_X^K - \hat{\theta}_X)^2 + (\theta_Y^K - \hat{\theta}_Y)^2}, \tag{4.27}$$

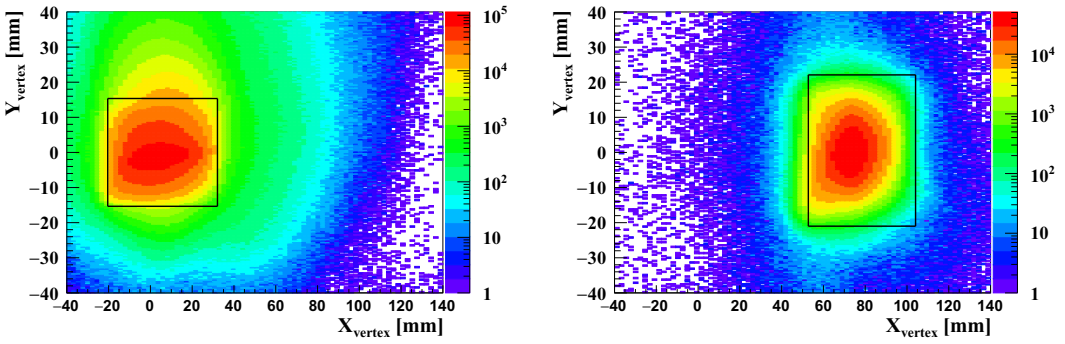

Figure 4.9: Projection of the decay vertex in (x, y) plane at $Z_{vertex} = 105$ m (left) and at $Z_{vertex} = 165$ m (right). The reconstructed vertex coordinates must be compatible with the beam profile at a give Z_{vertex} position, marked with the black box.

where $\theta^K_{X,Y}$ are the X, Y kaon candidate slopes, $\hat{\theta}_X = \hat{\theta}_Y = 0.00002$ rad and θ^K_X is computed assuming that the beam particles enter the fiducial decay region with a 1.22 mrad slope in the XZ plane.

4.3.2 Cuts against upstream backgrounds

An *upstream event* is any event not originating from the beam kaon decay in the fiducial volume (105, 165) m from the T10 target. A typical example is a $K_{2\pi}$ early decay, where the charged pion passes to the downstream part, while the photons from the π^0 decay are absorbed in the collimator ($Type$ 1). At the beginning of the beam line, there is a kaon, so KTAG will positively identify it. It decays after the KTAG, between the GTK stations. Then, if the pion from the decay is matched with an accidental track from the GTK, it will mimic the $\pi\nu\bar{\nu}$ signal. This situation is illustrated and explained in more detail in the upper plot of Fig. 4.10. Another possible passage of the pion from the early kaon decay is through the gaps in the last dipole of the achromat ($Type$ 2), see lower plot in Fig. 4.10. The suppression of background from these *upstream events* is described in the following sub-sections 4.3.2 and 4.3.2.

The distribution of $Type$ 1 and $Type$ 2 events in the plane of the last collimator is shown in Fig. 4.11.

In addition, these types of the upstream processes may resemble the signal events:

- the downstream pion promptly produced in the beam pion or proton inelastic interactions in the second and third GTK stations and combined with the accidental kaon track ($Type$ 3);
- prompt π^+ produced in the kaon-GTK3 inelastic collision ($Type$ 4);
- π^+ from a decay of a long living particle K_S, K_L or K^+ produced in kaon-GTK3 inelastic collisions ($Type$ 5).

To further restrain the upstream backgrounds, the events must fulfill these conditions:

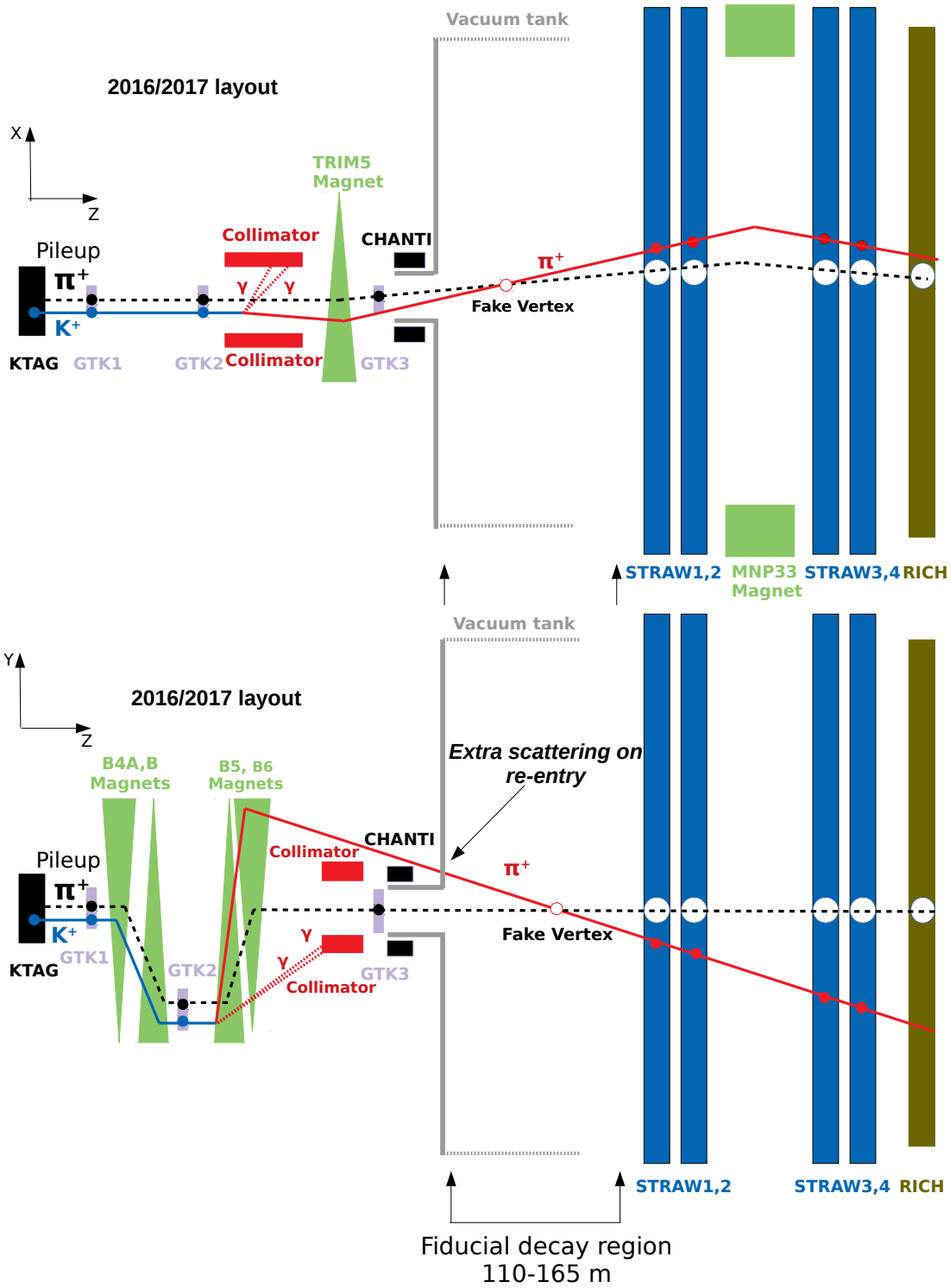

Figure 4.10: Illustration of the early decays producing the *upstream events*. The kaon (blue line) decays after the second GTK station and all products of the decay, except a pion (red line), are absorbed in the collimator. A pileup pion track (dashed black line), giving a good GTK candidate, is associated to the pion from the decay, reconstructing a fake vertex. The pion from the decay can pass through the inner part of the collimator (upper plot), or through the gaps in the last dipole of the achromat (lower plot).

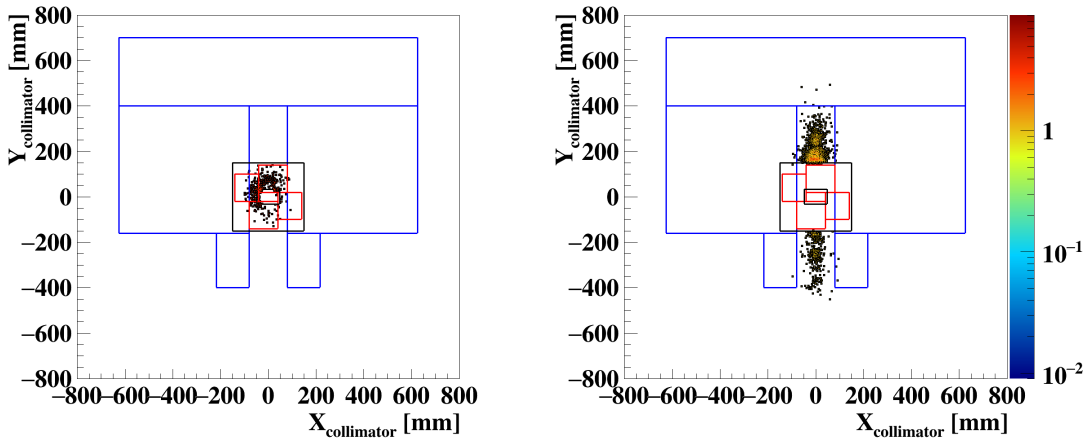

Figure 4.11: Position at TRIM5 of downstream track from a data sample enriched for upstream events. Left plot represents the *Type* 1 events, while right plot illustrates the distribution of the *Type* 2 events. Blue lines indicate the contour of the last dipole of the second achromat, four red boxes represent the four blocks of the final collimator and black line correspond to the acceptance region covered by CHANTI.

- the number of hits in each GTK station is less than 50;
- each GTK hit must have its time over threshold smaller than 24 ns;
- no events with GTK upstream candidate within 0.6 ns with respect to KTAG time associated to the *pion candidate*, if it is giving a positive match within $Z_{vertex} \in (100, 105)$ m range;
- less than 5 GTK track candidates within 0.6 ns compared to KTAG candidates;
- the downstream track extrapolated backwards to the GTK3 plane must be outside of the GTK3 acceptance;
- the cut against the scattering tails in the STRAW: it cuts the events which have the downstream track extrapolated backwards to GTK3 within 24 mm of the hit position in GTK3.

Type 1 **upstream background cut**

The *Type* 1 cut suppresses the background represented by pions originating upstream of the fiducial volume, illustrated in the upper plot of Fig. 4.10. First, the the following variables are defined, dependent on the Z component of the vertex:

$$cut_1 = a_1 + b_1 \cdot Z_{vtx}, \qquad a_1 = 315 - b_1 \cdot 105000, \qquad b_1 = -0.004; \tag{4.28}$$

$$cut_2 = a_2 + b_2 \cdot Z_{vtx}, \qquad a_2 = 900 - b_2 \cdot 105000, \qquad b_2 = \frac{a_1 - 900 - b_1 \cdot 115000}{10000}; \tag{4.29}$$

$$cut_3 = a_3 + b_3 \cdot Z_{vtx}, \qquad a_3 = 780 - b_3 \cdot 105000, \qquad b_3 = -0.00983333333. \tag{4.30}$$

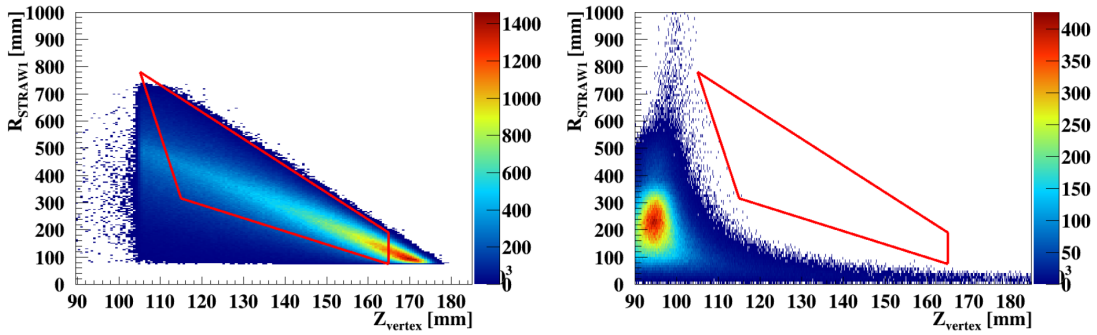

Figure 4.12: Distribution of the Z_{vertex} as a function of the radius of the downstream track in the first STRAW chamber. On the left the $\pi\nu\bar{\nu}$ MC simulation is shown, while plot on the right is obtained from the $K_{2\pi}$ MC where the kaons are decaying upstream the fiducial volume. The red contours specify the cut.

These are compared to the radius in the first STRAW chamber R_{st_1} in the following way:

$$R_{st_1} > cut_1, \quad R_{st_1} > cut_2, \quad R_{st_1} < cut_3. \tag{4.31}$$

The graphical illustration of the cut is in Fig. 4.12.

Type 2 **upstream background cut**

The early decays with the pion passing through the gaps in the last dipole of the achromat (Fig. 4.10 down) have a specific distribution when extrapolated backwards to the plane of the last achromat (TRIM5), see Fig. 4.11.

The π^+ *candidate* extrapolated back to TRIM5 must be outside a box defined by:

$$|X_{TRIM5}| < 100 \text{ mm and} |Y_{TRIM5}| < 500 \text{ mm}, \tag{4.32}$$

where (X_{TRIM5}, Y_{TRIM5}) are the $(x,\ y)$ coordinates of the π^+*candidate* at TRIM5. This cut (called *box cut*) removes all *Type* 2 events, but also reduces the $\pi\nu\bar{\nu}$ acceptance by about 50%.

4.3.3 Kinematics criteria

To suppress the kinematic tails from the main background contributions, these cuts are applied:

- the difference between *pion candidate* slope along $X(Y)$ measured before and after the spectrometer track fit is less than $\pm 0.3(1.0)$ mrad;
- the quality of the *pion candidate* track is ≤ 4, where the quality variable ranks the degree of goodness of the straw pattern recognition algorithm;
- at least 15 and not more than 42 straw hits form the *pioncandidate* track.

4.3.4 Single-track kaon decay

The $\pi\nu\bar{\nu}$ event has only one single track, originating in the kaon decay, as a visible signal in the final state. The track must carry a positive charge. If there

are several *pion candidates*, the one with the minimal time difference with respect to the trigger time is selected. To reject the possible background from a multi-track events, the selected *pion candidate* must have the minimal time difference with respect to the trigger time in all sub-detectors. Only events with no more than two tracks reconstructed by the STRAW detector are considered. If a pair of STRAW tracks is reconstructed, both of them must have a positive charge and their mutual CDA must be grater than 30 mm.

4.3.5 Charged multiplicity rejection

Charged multiplicity rejection refers to a set of cuts rejecting extra charged particles from the kaon decays, not fully reconstructed by the STRAW spectrometer, or from the inelastic interactions of photons before they reach LKr. The rejection conditions are based on the extra hits reconstructed in the hodoscopes, LKr, HASC and MUV0 detectors around the reference time provided by the CHOD48. The hits in STRAW not belonging to the reconstructed track, are covered in reconstruction of STRAW segments. Events with extra STRAW segments are removed.

Further suppression of $K_{3\pi}$ background is ensured by the condition:

$$R_{st_1} > -0.00436 \cdot Z_{vertex} + 830 \quad [\text{mm}], \tag{4.33}$$

where R_{st_1} is the distance of the downstream track from the first STRAW chamber center.

Extra activity in LKr

The extra hits in the LKr must cope with these conditions:

- energy of the hits are above 45 MeV;
- distance of the hits from the *pion candidate* track is more than 100 mm;
- hits with energy below 300 MeV are within ± 4 ns of the reference time;
- for energies within (300, 2000) MeV range, the time difference of the hit and reference time is within (-7, 10) ns;
- for energies above 2 GeV, the time difference between the hit and reference time is within ± 10 ns.

When products of events like $\mathrm{K}^+ \to \pi^+\pi^- e^+ \nu_e$ or $K_{3\pi}$ hit the LKr, the clusters produced by the charged particles can be close to each other. Owing to the standard clusterization procedure 2.2.11, they will be distinguished and they will have a proper energy sharing. To fully exploit the capability of cluster separation in rejecting the possible backgrounds from multi-track events, if an extra standard cluster is within (40, 100) mm and within ± 6 ns of the *pion candidate* associated cluster, the event is discarded.

Extra hits in hodoscopes

Extra hits in CHOD (CHOD48) are collecting all non-associated hits within ±5 ns (±7 ns) with respect to the reference time.

The matching of the extra hits between CHOD and CHOD48 is defined as:

- $dx < 250$ mm, $dy < 140$ mm, where dx, dy are the spatial differences of the extra hit positions in CHOD and CHOD48;
- their extra hits are within ±15 ns.

A CHOD48 extra hit is matched to LKr extra hit if it is:

- within ±15 ns of the LKr hit time;
- less than 130 mm away from the CHOD48 hit position.

A CHOD extra hit is matched to LKr in-time activity if it is:

- inside a rectangle defined by ±250 mm in x and ±140 mm in y.

The event is discarded if:

- there are more than three CHOD48 in-time hits;
- there is a matching between any combination of LKr, CHOD and CHOD48 as described above.

STRAW segments

The STRAW segments are built following a 2-steps procedure:

- first, the chamber-hits which do not belong to the pion track are reconstructed;
- second, the segments are reconstructed using vertex and chamber-hits in chambers 1 and 2 or vertex and chamber-hits in chambers 3 and 4.

Only first 500 hits, not associated to the pion track are taken. Chamber-hits which are not part of the pion track are reconstructed as follows:

- STRAW hits not belonging to the pion track are selected;
- STRAW hits are sorted per plane, keeping only those with the drift time within (0, 170) ns range;
- view-clusters of 2 and 3 hits belonging to different view-planes are formed in each view applying the same pattern recognition algorithm as in the standard spectrometer reconstruction; the staggering of the planes of the clustered hits solves the left-right ambiguity inherent of a straw signal and provides a measurement of the coordinate of a track passing through a straw in a local reference system of the view; a measurement of the coordinate of a track passing through a straw in the local reference system of the view is provided exploiting the staggering of the planes of the clustered straws to solve the left-right ambiguity;

- unpaired hits are also saved as 1-hit view-clusters, with the position of the straw used as coordinate of the track passing through;
- groups of two, three or four view-clusters belonging to different views per chamber are combined together to form the chamber-hits, adapting the pattern recognition algorithm used in the standard reconstruction to the additional presence of 1-hit view-clusters; in this respect the condition on the cluster time measured with the trailing has been broadened to ±200 ns instead of ±100 ns and the condition on the quality of the straw intersections softened to maximize the reconstruction efficiency.

The steps below outline the procedure used to reconstruct segments:

- least squared fits in two planes (xz and yz) are performed on all the triplets formed by two chamber-hits in chamber 1 and 2 and the vertex;
- a triplet is accepted if:
  - the fitted slopes are lower than 20 mrad in both the projections;
  - the fitted segments are at least 30 mm distant from the pion at chamber 1 and 2;
- the triplet with the minimum χ^2 satisfying the above conditions is defined as a segment in chamber 1-2 ($segment12$);
- the same steps as above are applied using chamber-hits in chambers 3 and 4 together with the vertex ($segment34$), with the difference that:
  - the fit and the condition on the slope are not applied in the xz plane;
  - the direction of the segment must be compatible with a negative particle with momentum not greater than 90 GeV/c or with a positive particle with momentum lower than 10 GeV/c.

Let $\Delta T_{segment}$ be the difference between T_{GTK} and the average of the trailing time of the two chamber-hits and χ^2 segment the value of the χ^2 of the corresponding triplet Then an event has an extra segment in the spectrometer if:

- $segment12$: $|\Delta T_{segment}| < 34 - 1.4 \cdot \chi^2_{segment}$;
- $segment34$: $|\Delta T_{segment}| < 40 - 5.7 \cdot \chi^1_{segment}$.

All the information in this section were obtained from an NA62 internal note, and are publicly accessible from a doctoral thesis [61].

HASC rejection

HASC can detect $K_{3\pi}$ events, where one of the positive pions is collinear with the beam. The dipole magnet after MUV3 will deflect it more than a beam, as it has lower momentum. Thus it will hit the HASC detector and produce in-time signal. Similarly, high energy photons, flying at low angles with respect to the beam, can shower in the beam pipe material and produce charged particles that can hit HASC. If HASC has a signal within ±3 ns of the reference time, the event is rejected.

MUV0 rejection

When a kaon decays to three pions and the negative pion has low momentum, or is followed by the subsequent decay to muon, it will be deflected by the spectrometer magnet out of the geometrical acceptance of the downstream detectors, but inside the MUV0 active area. If MUV0 detects a signal within the (-8, 10) ns of the reference time, the event is rejected.

4.3.6 Particle identification

The particle identification (PID) is performed independently with the RICH, calorimeters and MUV3. Its main purpose is to suppress the muons to the level of $\mathcal{O}(10^{-8})$, while keeping the pion efficiency as high as possible.

Pion identification with RICH

For the PID with RICH, information from both methods explained in section 4.1.4 is used. The cut using the likelihood-based algorithm method, which provides the probability of a downstream track being a specific particle, identifies the π^+ if the probabilities for the other types of particles are all below 0.12.

The *pion candidate* must also have an associated candidate reconstructed by the single ring algorithm. The particle mass derived from this method is computed in the following way:

$$M_{RICH} = P_\pi \cdot n \cdot \sqrt{\cos^2\left(\tan^{-1}\left(\frac{R_{ring}}{f_{length}}\right)\right) - 1}; \tag{4.34}$$

where R_{ring} is the reconstructed ring radius, $f_{length} = 17020$ mm is the focal length of the mirrors and n is the refraction index of the radiator gas. It is calculated as:

$$n = \frac{1}{\cos\left(tan^{-1}\left(\frac{R_{electron}}{f_{length}}\right)\right)}, \tag{4.35}$$

with $R_{electron}$ being a ring radius of $\beta = 1$ particle provided by the standard NA62 burst-by-burst dependent database. The particle, to be identified as a pion, needs to have M_{RICH} in the range of (0.125, 0.2) GeV/c^2. The RICH also provides the particle momentum, P_π^{RICH} used for signal region definition, according the relation:

$$P_\pi^{RICH} = m_{\pi^+} \cdot \frac{f_{length}}{\sqrt{R_{electron}^2 - R_{ring}^2}}, \tag{4.36}$$

where the π^+ mass hypothesis is made.

The performance of the RICH PID has been evaluated using the fully reconstructed $K_{\mu 2}$ and $K_{2\pi}$ events with omitted RICH information. The distinction between π, μ and e is the best within (15-35) GeV/c range, as is clearly visible in Fig. 4.13. The performance as a function of the momentum is shown in Fig. 4.14. The overall muon rejection is $(1.95 \pm 0.01) \times 10^{-3}$ at (83.75 ± 0.02) pion efficiency.

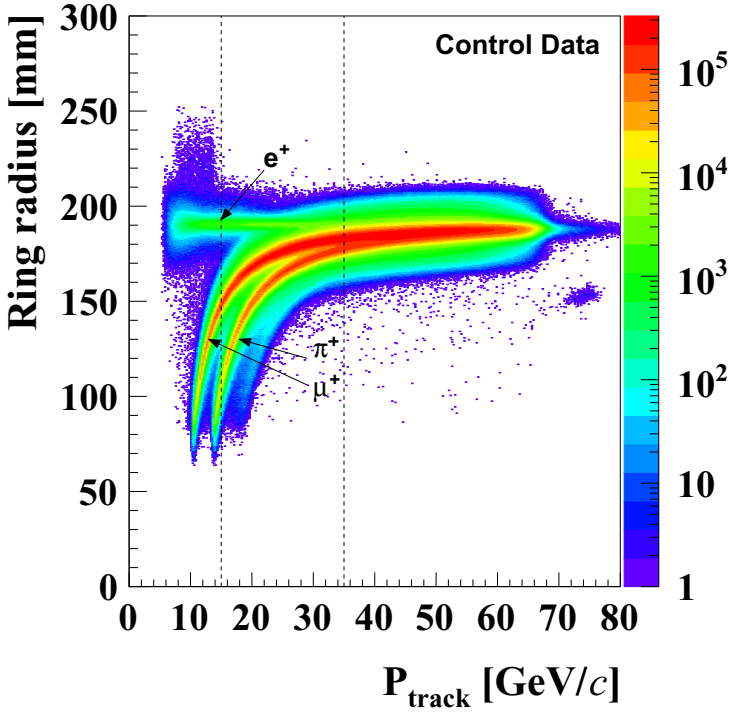

Figure 4.13: Ring radius measured by RICH as a function of momentum for positrons, muons and pions. The dashed lines mark the signal region of the $\pi\nu\bar{\nu}$ analysis, owing to best performance of the particle identification.

Pion identification with calorimeters

The conditions for a positive pion identification in the calorimeters are:

- a momentum dependent cut on the pion probability provided by the MVA algorithm:

$$Prob(\pi^+) > Max\left(0.7, 0.98 - 0.4596e^{\frac{-(p_\pi - 11.44)}{5.27}}\right), \tag{4.37}$$

  where p_π is the momentum of the *pion candidate*;

- there is no MUV2 energy if no MUV1 energy is associated to the *pion candidate*;

- the sum of energy in MUV1 and MUV2 not associated to the *pion candidate* does not exceed 5 GeV;

- $E_{LKr}/p < 0.8$ (positron rejection cut);

- $E_{tot}/p < 1.2$.

Further, there are cuts against a catastrophic bremsstrahlung of the muons in LKr and against muon decays before LKr, which can contaminate the pion sample. In that case no signal is expected in MUV1 and MUV2. If there is no significant energy associated to the pion in the MUV1 and MUV2, the pion

identification proceeds through the examination of the shower shape in LKr. It is based on the quantities of the associated LKr cluster:

$$R_{seed} = \frac{E_{seed}}{E^{LKr}_{cluster}}, \quad R_{cell} = \frac{N_{hits}}{E^{LKr}_{cluster}}, \tag{4.38}$$

where E_{seed} is an energy of the most energetic cell of the cluster, N_{hits} is a number of cells in the cluster and $E^{LKr}_{cluster}$ is the cluster energy. In case of a small associated energy in the hadronic calorimeters, expressed by the conditions $E_{MUV1}/E_{tot} < 0.01$ and $E_{MUV2}/E_{tot} < 0.01$, the following conditions identify an electro-magnetic shower in LKr:

- $R_{seed} > 0.2$ and $R_{cell} \leq 3$ GeV^{-1};
- $R_{seed} \leq 0.2$ and $R_{cell} < 1.8$ GeV^{-1};
- $R_{seed} < 0.05$;
- $R_{seed} > 0.35$.

Events with electro-magnetic like showers are rejected. Finally, events are kept only if these conditions are fulfilled:

- $R_{seed} \in (0, 0.8)$;
- $R_{cell} < 1.4$.

The performance of the PID in calorimeters has been tested with samples of fully reconstructed $K_{\mu 2}$ and $K_{2\pi}$ events, without using information from calorimeters. The overall performance as a function of momentum is depicted in Fig. 4.14. The average muon rejection is $(8.2 \pm 0.5) \times 10^{-6}$, while keeping the pion efficiency at the level of $77.37 \pm 0.02\%$.

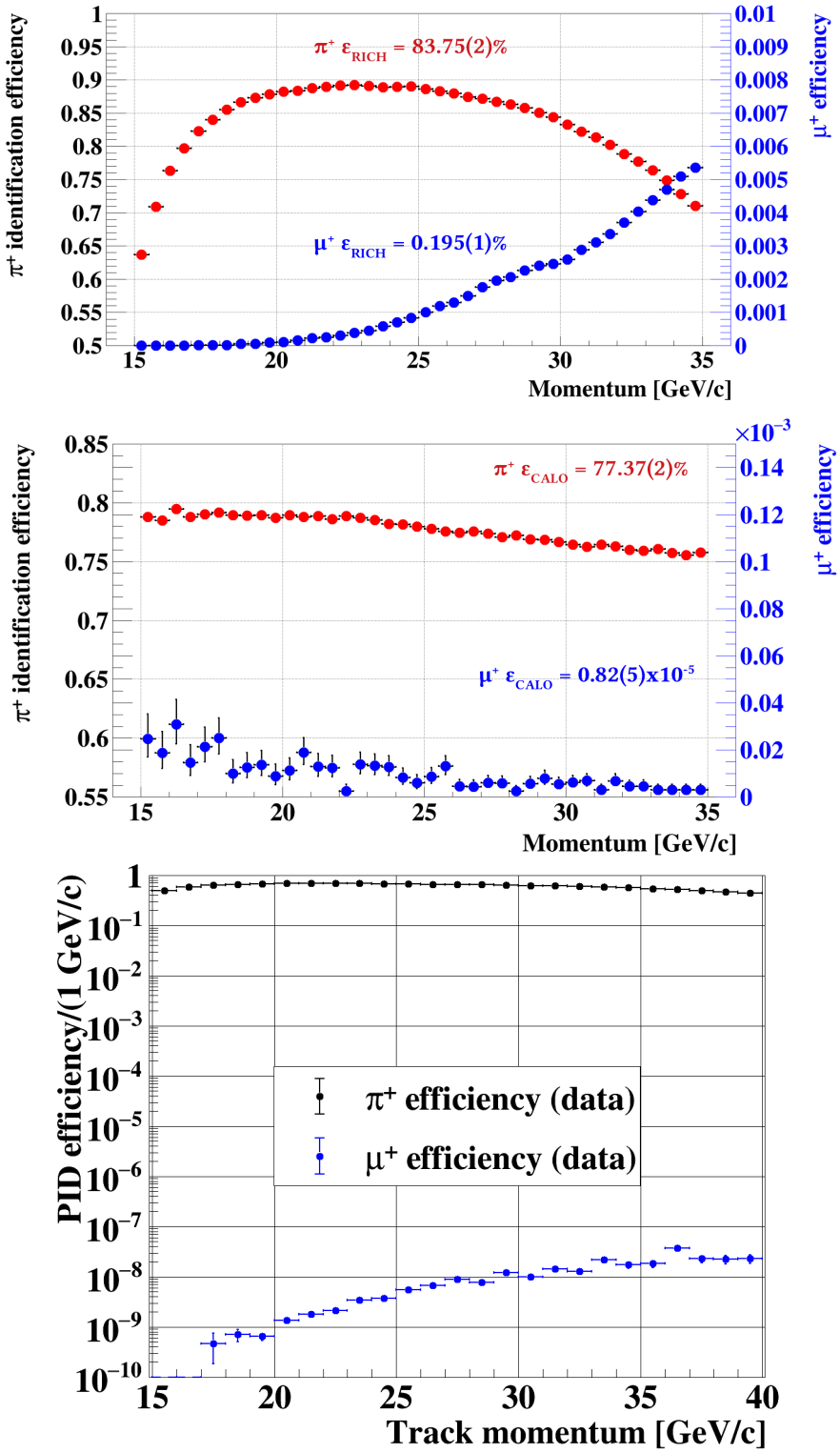

Figure 4.14: Top: RICH efficiency for the pions and muons as a function of their momentum. Middle: Pion and muon efficiencies after applying calorimetric particle identification as a function of their momentum. Bottom: The combined particle identification efficiencies for pions and muons measured on control data samples.

Cluster energy range	Timing condition
$E < 1$ GeV	$\lvert\Delta T_{LKr}\rvert < 5$ ns
$E \in (1,\ 2\rangle$ GeV	$\lvert\Delta T_{LKr}\rvert < 5 \cdot \sigma$ ns
$E > 10$ GeV	$\lvert\Delta T_{LKr} + 25\rvert < 2.5$ ns
$E > 10$ GeV	$\lvert\Delta T_{LKr} - 25\rvert < 2.5$ ns
$E \in (2,\ 15\rangle)$ GeV	$\lvert\Delta T_{LKr}\rvert < 15 \cdot \sigma$ ns
$E > 15$ GeV	$\lvert\Delta T_{LKr}\rvert < 70 \cdot \sigma$ ns

Table 4.1: The energy dependent timing cuts to classify the extra LKr clusters as photons.

4.3.7 Photon rejection

The signal events have single pion track in the final state and no other detectable energy. Hence, if there is any extra energy not associated with the pion track, or the activity in any of the LAV, IRC or SAC, the event is considered as a background event.

Photons in LKr

A cluster in LKr of energy $E_{cluster}$ and time $T_{cluster}$ is defined to be a photon cluster in time with the pion if it is at least 100 mm distant from the track extrapolated to the LKr surface and meets the timing conditions summarized in Table 4.1. The term $|\Delta T_{LKr}|$ is the time difference between the LKr cluster time and pion time T_π defined in eq. (4.4) and

$$\sigma = \left(0.56 + \frac{1.53}{E} - \frac{0.233}{\sqrt{E}}\right) \text{ ns}; \qquad E \text{ in GeV}, \tag{4.39}$$

is an energy dependent time resolution. The 25 ns shifts in time are accounting for the event with time wrongly assigned to a neighboring readout time slot. The value of 25 ns is due to 40 MHz sampling rate of the readout modules. The auxiliary cluster must have energy larger than 1 GeV to be classified as a photon cluster.

Photons in LAV

The standard na62fw tool LAVMatching [58] is used to veto events with an activity in the LAV detector. The event is rejected if any hit block in any LAV station is within 3 ns of the *pion candidate* time.

Photons in IRC and SAC

The photon veto conditions for IRC and SAC, dependent on the time over threshold (ToT) measurement provided by TDC readout module, are summarized in Table 4.2. The IRC and SAC hit times are corrected for slewing. If case of double signals in IRC and SAC, the measured ToT can be longer. When it reaches 30 ns (45 ns) for the IRC (SAC), the event is rejected.

The information from the FADC readout is exploited to reject the photons not detected by TDC readout. If the measured energy grater then 1 GeV in either IRC or SAC is within ± 7 ns of the pion time T_π, the event is discarded.

ToT range	Time cut [ns]
$ToT < 2$	$\lvert T_{IRC} - T_\pi \rvert < 7$ $\lvert (T_{IRC} - 7) - T_\pi \rvert < 7$ $-7 < (T_{SAC} + 3) - T_\pi < 10$
$2 \leq ToT < 25$	$\lvert T_(SAC) - T_\pi \rvert < 7$ $\lvert T_{SAC} - T_\pi \rvert < -8.3524 + 0.2105 \cdot ToT$
$2 \leq ToT < 30$	$-7 < T_(IRC) - T_\pi < 4$
$25 \leq ToT \leq 45$	$-7 < T_{SAC} - T_\pi < 4$

Table 4.2: Summary of time cuts for IRC and SAC. The times T_{IRC} and T_{SAC} represent the IRC and SAC hit times. ToT is the time over threshold measured by the TDC readout module.

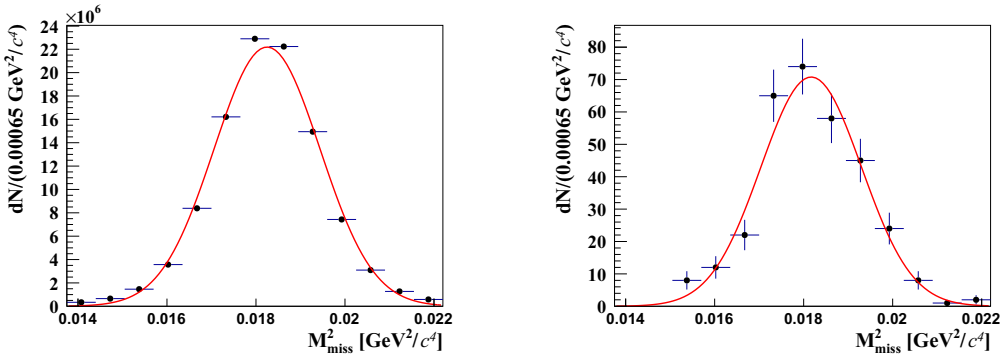

Figure 4.15: Left: The m^2_{miss} distribution of the $K_{2\pi}$ events selected on control trigger before applying photon rejection and multiplicity cuts. Right: The same distribution for the $K_{2\pi}$ events selected on $\pi\nu\nu$ trigger after applying photon rejection and multiplicity cuts.

Performance of photon rejection

The photon rejection performance is measured on data comparing the number of selected $K_{2\pi}$ events on control trigger ($N^{control}_{\pi^+\pi^0}$) before photon and multiplicity rejection with the number of selected $K_{2\pi}$ events on $\pi\nu\nu$ trigger ($N^{\pi\nu\nu}_{\pi^+\pi^0}$) after photon and multiplicity rejection. Fig. 4.15 illustrates the m^2_{miss} distribution around the $\pi + \pi^0$ peak for $N^{control}_{\pi^+\pi^0}$ and $N^{\pi\nu\nu}_{\pi^+\pi^0}$.

The π^0 rejection inefficiency is calculated in the following way:

$$\varepsilon_{PR} = \frac{N^{\pi\nu\nu}_{\pi^+\pi^0}(after\ \gamma - rejection)}{D \cdot N^{control}_{\pi^+\pi^0}(before\ \gamma - rejection) \cdot \varepsilon_{RV} \cdot \varepsilon_{trigger}}, \tag{4.40}$$

where $D = 400$ is a down-scaling factor for control trigger, ε_{RV} is the effect of random veto and $\varepsilon_{trigger}$ is the $\pi\nu\nu$ trigger efficiency. The random veto is measured on the control $K_{\mu 2}$ sample, with the positive muon identification and will be discussed in the later section 6.2.2. The variation of the π^0 rejection efficiency with momentum and intensity is shown in Fig. 4.16. The inefficiency ε_{PR} does not depend on the instantaneous beam intensity, but vary with momentum. This is expected, because at low track momentum the leftover energy for photons is higher, so they can travel closer to the beam pipe and cause the increase of π^0 rejection inefficiency.

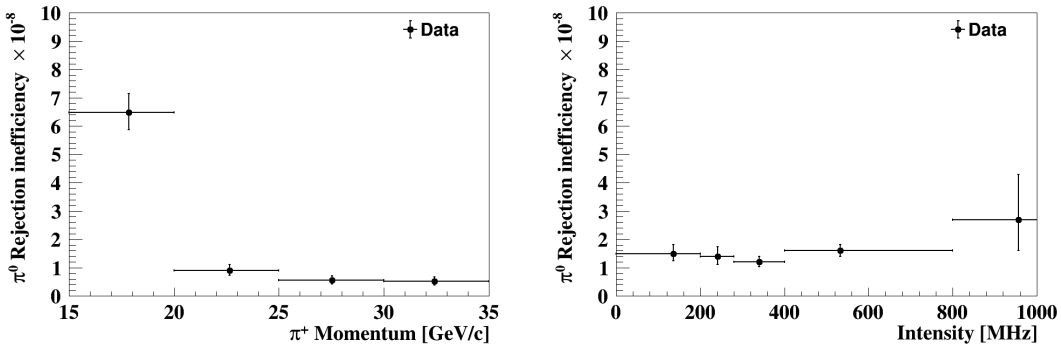

Figure 4.16: Rejection of π^0 as a function of momentum (left) and instantaneous beam intensity (right) [62].

The overall value within (15-35) GeV/c momentum is [62]:

$$\varepsilon_{PR} = (1.4 \pm 0.1) \times 10^{-8}. \tag{4.41}$$

The single photon efficiencies are evaluated by the tag and probe method on control $K_{2\pi}$ events separately for LAV, LKr, IRC and SAC.

4.4 Kinematic selection

The final step in the event selection is the choice of kinematic region. As outlined in chapter 3, the analysis proceeds only in a part of the kinematically allowed $\pi\nu\bar{\nu}$ region. Namely, the pion momentum must be within (15, 35) GeV/c range to maximize the performance of PID and only a specific m^2_{miss} regions are considered (see section 3.1). The strategy of the analysis is to keep the signal regions masked, perform the background estimation, calculate the number of expected signal events and unmask the signal regions. The distribution of events after the full selection is shown in Fig. 4.17. Here, the control regions which are used for background validation are still masked. They will be examined in the following chapter.

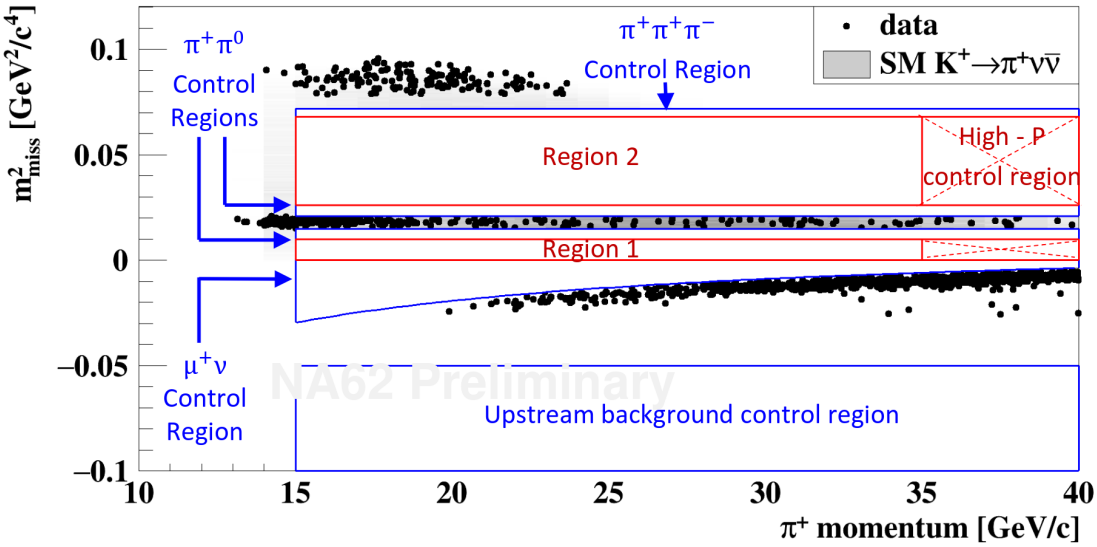

Figure 4.17: The distribution of the events after the full $\pi\nu\bar{\nu}$ selection. Signal and control regions are kept masked.

5. Background estimation

Processes which can mimic the signal events are summarized in Table 5.1. Procedures used for estimation of distinct background components in signal regions (R1, R2) will be described in this chapter. Validation of backgrounds is done in several control regions, which are defined in Table 3.1 and indicated in Fig. 4.17.

The $K_{e3}(K^+ \to e^+\pi^0\nu)$ decay is used to estimate the RICH rejection power for the electrons. The background estimation for this decay is also presented. The final estimations also take into account the trigger efficiency (ε^{Trig}), the random veto efficiency (ε^{RV}) and the total number of kaon decays (N_K), while all are estimated from the 2017 data and summarized in table 5.2.

Process	BR	Suppression mechanism
$K^+ \to \pi^+\pi^0(\gamma)$ IB	20.67%	Kinematic tails, π^0 rejection
$K^+ \to \mu^+\nu_\mu(\gamma)$ IB	63.56%	Kinematic tails, PID
$K^+ \to \pi^+\pi^-e^+\nu_e$	4.247%	Multiplicity rejection
$K^+ \to \pi^+\pi^-\pi^+$	5.583%	Kinematic tails, multiplicity rejection
$K^+ \to \pi^+\gamma - \gamma$	1.01×10^{-6}	π^0 rejection
$K^+ \to \pi^0\mu^+\nu_\mu$	3.352%	π^0 rejection, PID
$K^+ \to \pi^0e^+\nu$	5.07%	π^0 rejection, PID
$K^+ \to \pi^+\pi^0_D$ $\pi^0_D \to e^+e^-\gamma$;	20.67% 1.174%	Kinematic tails, γ rejection
$K^+ \to \mu^+\nu_\mu$; $\mu^+ \to e^+\nu_e\bar{\nu_\mu}$	63.56% $\approx 100\%$	Kinematic tails, PID
$K^+ \to e^+\nu_e$	1.582×10^{-5}	
Upstream backgrounds		$K - \pi$ matching, π^0 rejection, CHANTI, *Type* 1 and *Type* 2 cuts

Table 5.1: List of all considered backgrounds, with corresponding branching ratios (BR) [63] and mechanism used to suppress them.

ε^{Trig}	ε^{RV}	N_K
0.87	0.63	$(12 \pm 1) \times 10^{11}$

Table 5.2: Trigger efficiency (ε^{Trig}), random veto efficiency (ε^{RV}) and total number of kaon decays (N_K) estimated from the 2017 data.

The estimation of background from $K_{2\pi}(\gamma)$, $K_{\mu 2}(\gamma)$ and $K_{3\pi}$ proceeds through the evaluation of the kinematic tails in the m^2_{miss} distributions. They are present due to the mis-reconstruction caused by the material present in the particle path and subsequent multiple scattering of the pion in STRAW1, kaon scattering in GTK3 or by their combination resulting in the wrong $K - \pi$ association. The components of the m^2_{miss} resolution as a function of momentum are shown in Fig. 3.2. The kinematic tails depend on the beam intensity, as the GTK-STRAW mis-matching probability increases quadratically with the intensity.

Momentum [GeV/c]	15-20	20-25	25-30	30-35	35-40
$N(\pi^+\pi^0)$	160	34	21	27	15

Table 5.3: Number of observed events in given momentum bins.

5.1 Background from $\mathrm{K}_{2\pi}(\gamma)$

The contamination of R1, R2 with $\mathrm{K}_{2\pi}(\gamma)$ decays is estimated from the number of selected events in the $\pi^+\pi^0$ region after the $\pi\nu\nu$ selection ($N(\pi^+\pi^0)$), multiplied by the kinematic suppression factor. The number of expected events in the signal and control regions is given by the relation:

$$N^{\pi\pi}_{expected}(region) = \sum_j \left[N(\pi^+\pi^0)_j \cdot f^{kin}_j(region) \right], \tag{5.1}$$

where the index j runs over four momentum bins (15-35 GeV with 5 GeV step) and $f^{kin}_j(region)$ is the kinematic suppression factors in the specific region. The factors $f^{kin}_j(region)$ represent the fractions of $\mathrm{K}_{2\pi}$ events entering either the signal or control regions through the tails of the m^2_{miss} peak. Their meaning is the probability that a pion track is wrongly reconstructed in a given region. The kinematic tails, $f^{kin}_j(region)$, are defined in the full R1+R2, including the constraints put on $m^2_{miss}(RICH)$ and $m^2_{miss}(beam)$. In eq. (5.1) no correlation between π^0 rejection and kinematic rejection is assumed. Consequently, this treatment cannot be used for the background estimation of the radiative decay $\mathrm{K}^+ \to \pi^+\pi^0\gamma$.

The kinematic tails are measured using the control data sample, with the "full" $K_{2\pi}$ selection (see App. A.1) including the π^0 tagging with two photons in LKr (two in-time clusters without associated track reconstructing m_{π^0}). The distributions of the full $K_{2\pi}$ selection and the "normalization" $K_{2\pi}$ selection ($\pi\nu\nu$-like, i.e. without π^0 tagging) are shown superimposed in Fig. 5.1. The tagging of π^0 does not modify the kinematic properties as can be seen in R1, where no radiative component is present. The agreement in R1 between the full $K_{2\pi}$ and the "normalization" $K_{2\pi}$ selections proves that one can extract $f^{kin}_j(region)$ in the outlined procedure. The comparison between the control $K_{2\pi}$ sample, used to measure the kinematic tails, and MC simulation is shown in Fig. 5.2. The simulation is consistent with data within the systematic uncertainties over five orders of magnitude, once the effect of beam pileup is included.

The values of f^{kin} as functions of momentum and intensity are shown in Fig. 5.3. There is no variation with momentum, but it changes with intensity. Such a behavior is expected, as higher intensity implies higher mis-match probability in the $K^+ - \pi^+$ association.

Number of events in the $K_{2\pi}$ background region, after the complete $\pi\nu\nu$ selection, in bins of momentum is presented in Table 5.3.

Radiative $K_{2\pi\gamma}$ decays

The photon from the radiative $\mathrm{K}_{2\pi\gamma}$ event spoils the kinematic distribution and causes a shift of m^2_{miss} towards the R2. It results in worsening of the kinematic rejection power by a factor ~ 6. This decrease is overcompensated by the increase of the photon rejection power by a factor ~ 30, as an extra photon is present, and makes the radiative $K_{2\pi}$ component much smaller compared to $K_{2\pi}$ one.

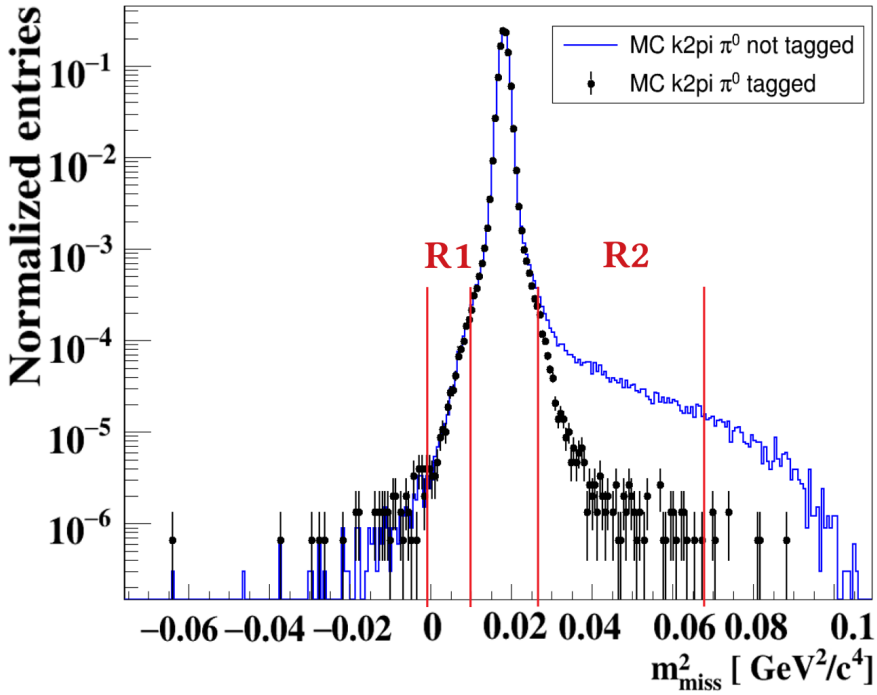

Figure 5.1: The effect of the π^0 tagging studied on MC. It has no bias in the tails in R1 and it reduces significantly the background in R2.

Region	CR1	CR2	R1	R2
$N^{\pi\pi}_{expected}$	2.6(3)	5.1(6)	0.11(6)	0.16(2)
$N^{\pi\pi\gamma}_{expected}$	-	-	-	0.02(2)

Table 5.4: Number of expected events in control (CR1, CR2) and signal (R1, R2) regions.

Background validation and final estimation

Combining the number of observed events with the kinematic tails result in the expected number of events in the kinematic regions. The Poissonian statistical uncertainty is obtained from the number of events used for the kinematic tails, f^{kin}, measurement and from number of events in Table 5.3. The systematic error originates from the π^0 tagging and represents the half difference between Data and MC in R1. The estimate of number of events in the CR1, CR2, R1 and R2 regions for $K_{2\pi}$ and its radiative decay is given in Table 5.4, with the error budget detailed in Table 5.5.

Source	Relative uncertainty
Statistical (tails)	3%
Statistical $N(\pi^+\pi^0)$	9%
π^0 tagging bias	5%
Radiative contribution	8%

Table 5.5: The error budget for the $N^{\pi\pi}_{expected}$.

After estimating $N^{\pi\pi}_{expected}$ in the CR1 and CR2, the corresponding areas are unmasked to validate the procedure. The result is shown in Fig. 5.4 and the

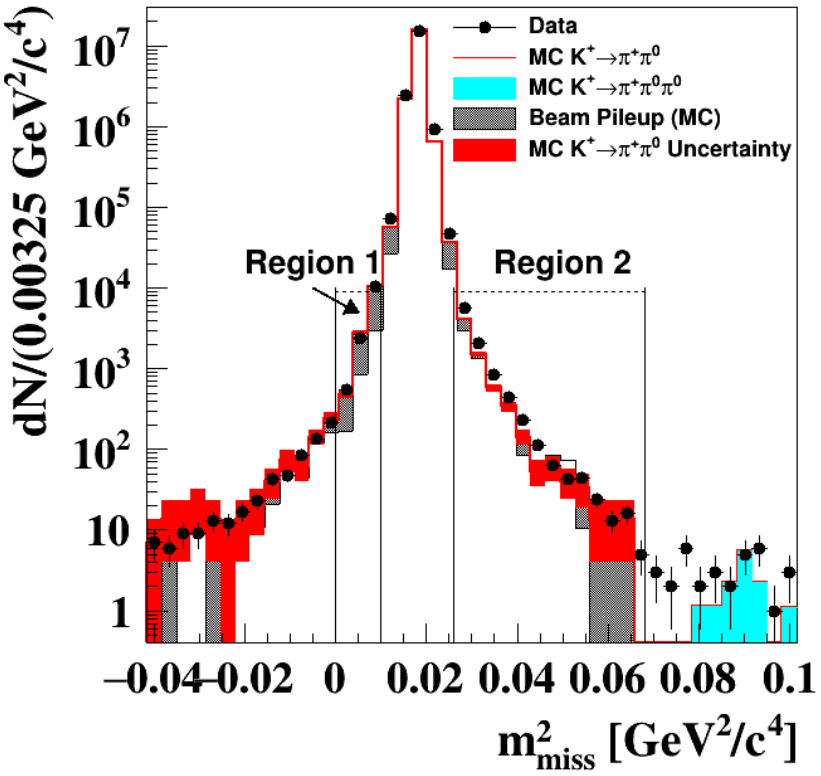

Figure 5.2: Distribution of m^2_{miss} of the selected $K_{2\pi}$ control events using data, with two γ from π^0 tagged in the LKr (black dots). MC distribution of $K_{2\pi}$ with tagged π^0 is superimposed (red line), with the 1 σ systematic uncertainty (red band). The simulated pileup contribution to m^2_{miss} is illustrated by the gray bands. A small contribution of $K_{3\pi}$ events is visible in the large m^2_{miss} region.

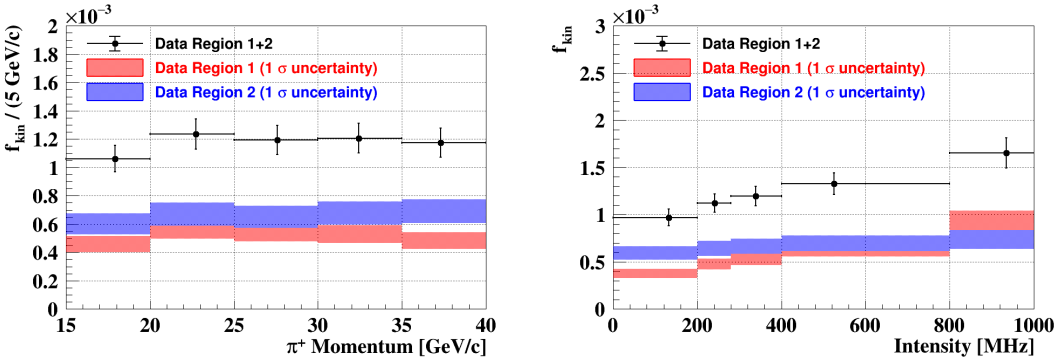

Figure 5.3: Kinematic tails f^{kin} variations with respect to momentum (left) and beam intensity (right).

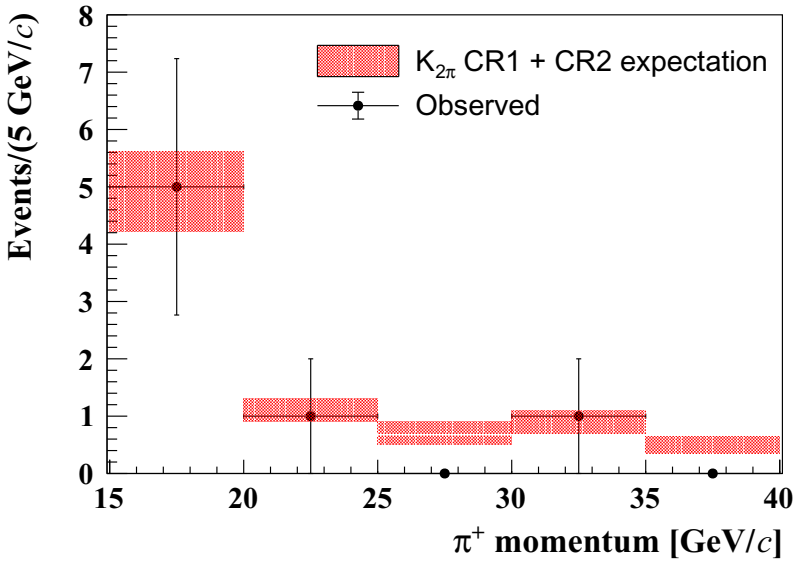

Figure 5.4: Validation of the $K_{2\pi}(\gamma)$ background as a function of momentum. The red boxes represent the expected number of $K_{2\pi}(\gamma)$ events with errors (area of the box) in the control regions around the $\pi^+\pi^0$ peak. The black dots correspond to number of events observed, with the statistical uncertainties, after unmasking the control regions.

number of expected events agrees with the number of observed events within the uncertainties.

The total number of expected $K_{2\pi}(\gamma)$ events in the R1 and R2 is:

$$0.29 \pm 0.03_{stat} \pm 0.03_{syst}. \tag{5.2}$$

5.2 Background from $K_{\mu 2}(\gamma)$

Similarly to $K_{2\pi}(\gamma)$, the background estimation of $K_{\mu 2}(\gamma)$ proceeds through the rejection induced by the kinematic distribution:

$$N^{\mu\nu}_{expected}(region) = \sum_j \left[N(\mu^+\nu)_j \cdot f_j^{kin}(region) \right], \tag{5.3}$$

where $N(\mu^+\nu)_j$ is the number of $K_{\mu 2}$ events passing the $\pi\nu\nu$ selection in the $\mu\nu$ region, f_j^{kin} is the fraction of $K_{\mu 2}(\gamma)$ entering either control or signal region and the index j runs over the four momentum bins, 5 GeV/c wide. Fig. 5.5 shows the distribution of the m^2_{miss} of $K_{\mu 2}$ used for the kinematic tails measurement. The variation of the kinematic tails with momentum and beam intensity is depicted in Fig. 5.6. The strong momentum dependence in R1 is caused by the worsening of PID in RICH towards higher momentum and because the center of m^2_{miss} peak moves to zero with momentum. The background contamination is at 1% level in R2 from $K^+ \to \pi^0\mu^+\nu_\mu$ decays.

The use of RICH likelihood can correlate PID and kinematics if $K_{\mu 2}$ events enter signal regions because of a mis–measurement of the particle 3–momentum in the STRAW. To remove the correlation between RICH likelihood and good

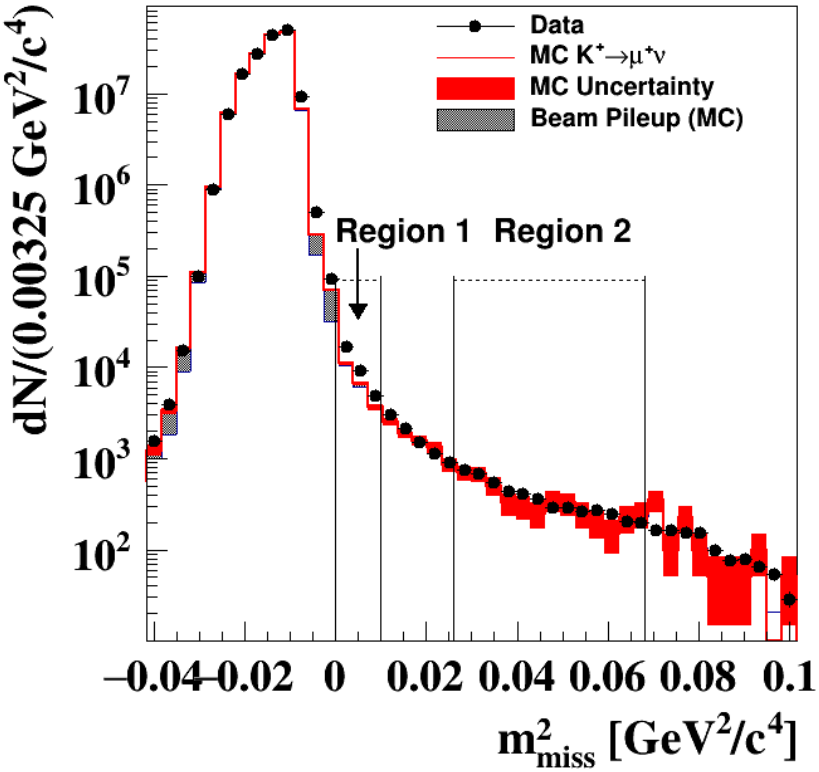

Figure 5.5: Distribution of m^2_{miss} of the selected $K_{\mu 2}$ control events using data (black dots). MC distribution is superimposed (red line), with the 1 σ systematic uncertainty (red band). The simulated pileup contribution to m^2_{miss} is illustrated by the gray bands.

STRAW candidate, two alternative methods are used for $K_{\mu 2}(\gamma)$ background estimation:

- the first method assumes that the RICH PID and kinematics are uncorrelated;
- the second method assumes that the RICH PID and calorimetric PID are uncorrelated.

In the first method, the kinematic tails are measured independently of RICH PID.

The latter method measures the kinematic tails together with RICH PID. The eq. (5.3) is modified:

$$N^{\mu\nu}_{expected}(region) = \sum_j \left[N(\mu^+\nu)^{!RICH}_j \cdot f^{kin+RICH}_j(region) \right], \qquad (5.4)$$

where $f^{kin+RICH}_j$ is measured as the ratio between events in R1$\vee$R2 after RICH PID and events in the $K_{\mu 2}$ background region before RICH PID.

Number of events in the $K_{\mu 2}$ background region after the complete $\pi\nu\nu$ selection in bins of momentum for both methods is presented in Table 5.6.

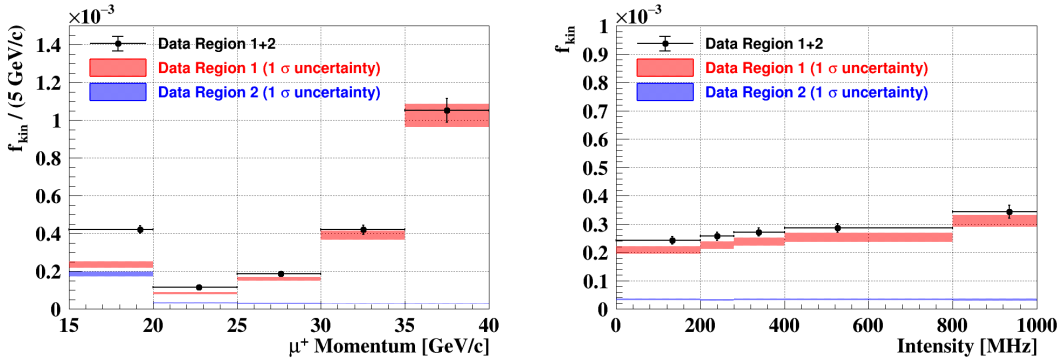

Figure 5.6: Kinematic tails f^{kin} variations with respect to momentum (left) and intensity (right).

Momentum [GeV/c]	15-20	20-25	25-30	30-35	35-40
$N(\mu^+\nu)$	1	48	143	287	472
$N^{!RICH}(\mu^+\nu)$	18426	102382	79249	58081	45986

Table 5.6: Number of observed events in bins of momentum.

Background validation

The total expected background from $K_{\mu 2}(\gamma)$ in the R1 and R2 obtained from both methods is:

$$\text{Method 1}: N^{\mu\nu}_{expected} = 0.14 \pm 0.01; \quad \text{Method 2}: N^{\mu\nu}_{expected} = 0.08 \pm 0.01. \quad (5.5)$$

The average of the two methods is taken as the final background estimation:

$$N^{\mu\nu}_{expected} = 0.11 \pm 0.02_{stat} \pm 0.03_{syst}. \quad (5.6)$$

Half of the difference between the two estimations is assigned as a systematic uncertainty. The contributions in control and signal regions are listed in Tab. 5.7 The statistical uncertainty is obtained from the number of events used for the kinematic tails f^{kin} measurement and the Poissonian fluctuation of the events of Table 5.6. The break-down of the uncertainties is listed in Tab. 5.8.

After estimating $N^{\mu\nu}_{expected}$ in the $\text{CR}_{K_{\mu 2}}$, the corresponding area is unmasked to validate the procedure. The result is shown in Fig. 5.7 and the number of expected events agrees with the number of observed events within the uncertainties.

Region	CR	SR1	SR2
$N^{\mu\nu}_{expected}$	11(1)	0.11(4)	0.002(2)

Table 5.7: Number of expected events in control (CR) and signal (SR) regions.

Source	Relative uncertainty
Statistical (tails)	18%
Statistical $N(\mu^+\nu)$	5%
PID bias of the tails sample	5%
Use of two different methods	27%
Background contamination	1%

Table 5.8: The error budget for the $N^{\mu\nu}_{expected}$.

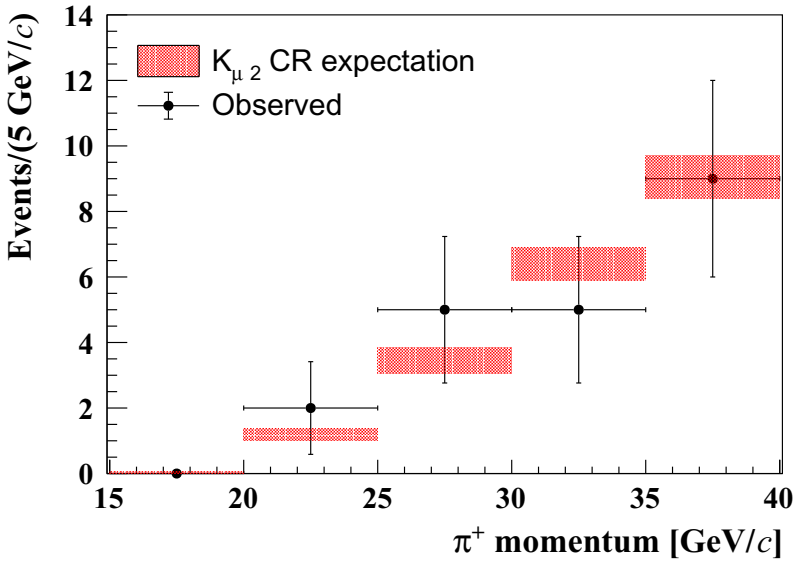

Figure 5.7: Validation of the $K_{\mu 2}(\gamma)$ background as a function of momentum. The red boxes represent the expected number of $K_{\mu 2}(\gamma)$ events in the $CR_{K_{\mu 2}}$. The black dots correspond to number of events observed after unmasking the $CR_{K_{\mu 2}}$.

Region	$CR_{3\pi}$	Observed $CR_{3\pi}$
$N^{\pi\pi\pi}_{expected}$	< 0.48	0

Table 5.9: Number of expected and observed events in the control (CR) regions.

5.3 Background from $K_{3\pi}$

The upper limit of R2 is specifically set to exclude the $K_{3\pi}$ decay, which starts beyond the mass of $4m^2_{\pi^+}$, and to leave some space for the $\pi^+\pi^+\pi^-$ control region ($CR_{3\pi}$). The $K_{3\pi}$ component of background is again estimated through the kinematic tails,now on the other side of the m^2_{miss} spectrum without momentum dependence:

$$N^{expected}_{\pi\pi\pi} = N(\pi\pi\pi) \cdot f^{kin}(region), \tag{5.7}$$

with $N(\pi\pi\pi)$ being the number of reconstructed $K_{3\pi}$ events using control data after $\pi\nu\nu$ selection in the $\pi\pi\pi$ region and f^{kin} representing the fraction of $K_{3\pi}$ events entering either control or signal regions. Kinematic tails measurement proceeds through the selection of a $K_{3\pi}$ sample on control data by tagging $\pi^+\pi^-$ pair. This method biases the distribution of m^2_{miss} and affects the tails, so the conservative limit at the level of 10^{-4} has been set and 100% systematic uncertainty assigned. Table 5.9 informs about the expected and observed number of events in various regions.

The total number of expected events in signal regions is:

$$N^{expected}_{\pi\pi\pi} = 0.02 \pm 0.02. \tag{5.8}$$

5.4 Background from $K^+ \to \pi^+\pi^- e + \nu_e (K_{e4})$

This process can mimic the $\pi\nu\nu$ event if the e^+ has momentum below 5 GeV/c, π^- interacts inelastically in the beam pipe and its products are lost, and only a single π^+ remains detectable. It is a 4-body decay spread over the whole $\pi\nu\nu$ kinematic regions, making the data driven approach practically impossible. Hence, K_{e4} background is estimated purely from the MC studies, based on the sample of 1.5 billion decays generated in the fiducial volume. Five validation samples, enriched for K_{e4} and orthogonal to the standard $\pi\nu\nu$ selection, are defined:

1. $\pi\nu\nu$ selection with STRAW multiplicity inverted;
2. $\pi\nu\nu$ selection with negative downstream track and STRAW multiplicity inverted (RICH PID not applied);
3. $\pi\nu\nu$ selection with negative downstream track and STRAW multiplicity inverted (RICH PID applied);
4. $\pi\nu\nu$ selection with negative downstream track and RICH PID not applied;
5. $\pi\nu\nu$ selection with negative downstream track and RICH PID applied.

Validation sample	Acceptance	$N_{expected}$	$N_{Observed}$
1	$2.7(1)\times10^{-7}$	8(1)	12
2	$3.7(1)\times10^{-6}$	109(7)	94
3	$4.5(2)\times10^{-7}$	13(1)	23
4	$8.3(2)\times10^{-7}$	25(2)	30
5	$1.1(1)\times10^{-7}$	3(1)	6
$\pi\nu\nu$ selection	$4(2)\times10^{-9}$	0.12(6)	-

Table 5.10: Number of expected and observed events for various K_{e4} validation samples.

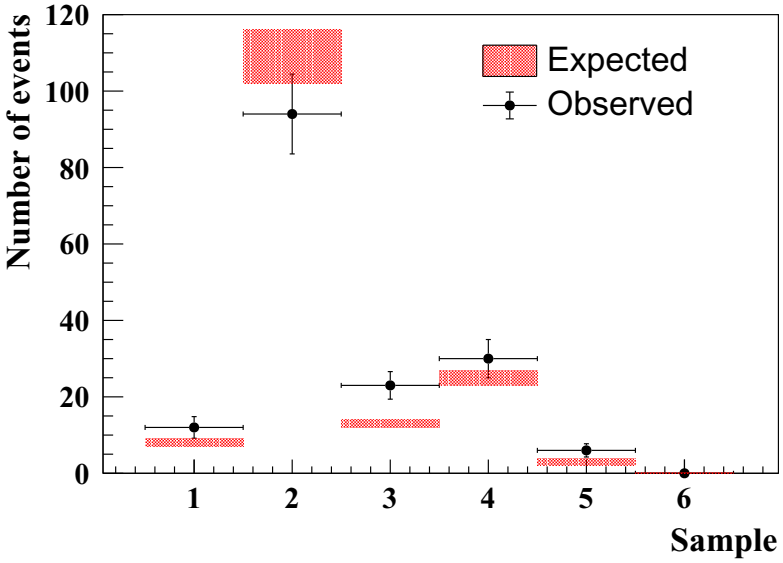

Figure 5.8: Validation of the K_{e4} background of the samples. The red boxes represent the expected number of K_{e4} events in the $0.026 < m^2_{miss} < 0.072$ GeV$^2/c^4$ control region. The black dots correspond to number of events observed after unmasking this control region.

Background validation

The validation region is defined in the range $0.026 < m^2_{miss} < 0.072$ GeV$^2/c^4$, as it is free from other background processes. Table 5.10 compares the data and MC simulation results for all samples. In general, a good agreement between data and MC in the validation samples is obtained. The comparison is graphically presented in Fig. 5.8.

The total number of expected K_{e4} in the signal regions is:

$$N_{Ke4}^{expected} = 0.12 \pm 0.05_{stat} \pm 0.03_{syst}. \tag{5.9}$$

The statistical uncertainty is due to limited MC sample. A half of the difference between expectation and observation in validation sample 3 is assigned as a systematic uncertainty.

5.5 Background from $K^+ \to \pi^+\gamma\gamma$

The BR at the level of 10^{-6}, presence of two photons and kinematics suppress the background from $K^+ \to \pi^+\gamma\gamma$ decays. Owing to form factors, the m^2_{miss} is pushed towards the 3π region making the kinematic rejection more powerful. Prior to the photon rejection, the overall acceptance for $K^+ \to \pi^+\gamma\gamma$ after $\pi\nu\nu$ selection is 1.8%.

The total estimated background from $K^+ \to \pi^+\gamma\gamma$ decay is:

$$N^{expected}_{\pi\gamma\gamma} = 0.005 \pm 0.005 \tag{5.10}$$

events.

5.6 Upstream Background

The *upstream events*, described in section 4.3.2, are the main source of background in the 2017 data. It has a purely geometrical origin and depends on the beam line geometry, Z_{vertex} and position of the downstream pion track extrapolated backwards into the TRIM5 plane. Different types of the *upstream events* are classified as follows:

1. *Type* 1 : π^+ from a K^+ decay in the beam line region between GTK2 and GTK3, associated to an accidental GTK track with the π^+ passing through the inner part of the collimator;
2. *Type* 2 : π^+ from a K^+ decay in the beam line region between GTK2 and GTK3, associated to an accidental GTK track with the π^+ passing through the gaps in the last dipole of the achromat;
3. *Type* 3 : π^+ from interactions of a beam pion or proton with GTK2 or GTK3, associated to an accidental K^+ GTK track;
4. *Type* 4: prompt π^+ produced in a kaon-GTK3 inelastic collision;
5. *Type* 5 : π^+ from a decay of a long living particle K_S, K_L or K^+ produced in kaon-GTK3 inelastic collision.

For the first three types of events, a pileup track matching the downstream track is required. In the first two cases, it can be any GTK track, while in the *Type* 3 events it must be a kaon track, as a presence of signal in KTAG is needed. The rejection of these types are primarily provided by:

- $K - \pi$ matching as described in section 4.2.2;
- geometrical cuts as described in sections 4.3.2 and 4.3.2 (*box cut*);
- no matched CHANTI candidate (see section 4.2.1).

Types 1, 2,3 and 4 need to have a scattering in the first STRAW chamber to enter the $\pi\nu\nu$ signal region out of the TRIM5 box. The scattering leads to smearing of the CDA distribution. The number of events in *Type* 2 region is very small and completely removed by the *box cut*.

Events of *Type* 4, 5 involve interactions of beam kaon, hence its track is present in GTK. The main rejection factors come from:

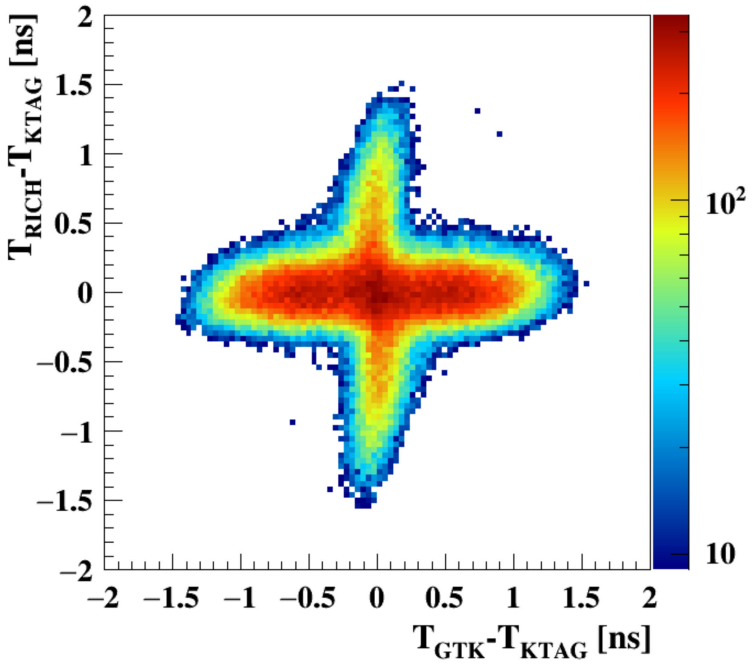

Figure 5.9: Distribution of the *upstream events* in the $T_{GTK} - T_{KTAG}$, $T_{RICH} - T_{KTAG}$ plane. The accidental bands around $T_{RICH} - T_{KTAG} = 0$ and $T_{GTK} - T_{KTAG} = 0$ correspond to *Type* 1, 2 events and *Type* 3 events, respectively. *Type* 4 and 5 events are around the center of the plot.

- no matched CHANTI candidate, because the pion entering the downstream region is produced in association with high particle multiplicity generating signals in CHANTI;
- geometrical cuts of the fiducial decay region and projection in the TRIM5, i.e. the *box cut* (see eq. (4.32));
- CDA related cuts in the $K - \pi$ matching.

Fig. 5.9 shows the distribution of all kinds of the *upstream events* in the $T_{GTK} - T_{KTAG}$, $T_{RICH} - T_{KTAG}$ plane. *Type* 1 and 2 events have a kaon in KTAG matched in time with the corresponding downstream track measured by RICH, matched to the pileup GTK track. Hence, they occupy the horizontal band of the plot, as the accidental GTK track has a random time not centered at zero. The vertical band is consistent with *Type* 3 events, where the kaon gives a coincidence in the KTAG and GTK, to which an accidental downstream track from the beam π^+/p^+ interaction is matched. *Type* 4 and 5 events are expected around the (0, 0) coordinate in the $T_{GTK} - T_{KTAG}$, $T_{RICH} - T_{KTAG}$ plane, but the analysis shows that the first three processes are enough to explain the accumulation of events around the central part of the distribution.

5.6.1 Upstream background evaluation

The *upstream events* passing the $\pi\nu\nu$ selection form the upstream background. The data driven upstream background estimation is used. The events remaining after the $\pi\nu\nu$ selection without $K-\pi$ matching and without *box cut* applied are divided into several sub-samples, according to their behavior under the $K-\pi$ matching and *box cut*:

- Sample A: good $K-\pi$ matching, *box cut* applied, m^2_{miss} in R1 or R2;
- Sample A_{neg}: good $K-\pi$ matching, *box cut* applied, $m^2_{miss} < -0.05$;
- Sample $B1$: good $K-\pi$ matching, extrapolated position in TRIM5 is $|X_{TRIM5}| < 100$ mm, $|Y_{TRIM5}| < 140$ mm and m^2_{miss} in R1 or R2;
- Sample $B2$: good $K-\pi$ matching, extrapolated position in TRIM5 is $|X_{TRIM5}| < 100$ mm, $140 < |Y_{TRIM5}| < 500$ mm and m^2_{miss} in R1 or R2;
- Sample C: $CDA > 4$ mm, *box cut* applied, m^2_{miss} in R1 or R2;
- Sample C_{neg}: $CDA > 4$ mm, *box cut* applied, $m^2_{miss} < -0.05$;
- Sample $D1$: $CDA > 4$ mm, extrapolated position in TRIM5 is $|X_{TRIM5}| < 100$ mm, $|Y_{TRIM5}| < 140$ mm and m^2_{miss} in R1 or R2;
- Sample $D2$: $CDA > 4$ mm, extrapolated position in TRIM5 is $|X_{TRIM5}| < 100$ mm, $140 < |Y_{TRIM5}| < 500$ mm and m^2_{miss} in R1 or R2;

All events can enter Samples A, $B1$, $B2$ and C. Sample A corresponds to the full $\pi\nu\nu$ selection in the signal regions, so it is kept masked. Samples $B2$ and $D2$ are completely dominated by the *Type* 2 events, while Sample $D1$ contains mainly *Type* 1, and *Type* 3 events.

General estimation procedure

The upstream background estimation is calculated as follows:

$$N^{bkg}_{upstream} = N^{upstream}_{\pi^+} \cdot P_{mistag}, \tag{5.11}$$

where $N^{upstream}_{\pi^+}$ refers to events with a downstream pion with 15-35 GeV/c momentum originating upstream of GTK3 and P_{mistag} is a probability that this downstream π^+ is matched to a GTK track, i.e. the $K-\pi$ matching is mis-tagged. The quantity $N^{upstream}_{\pi^+}$ depends on the beam characteristics (momentum, slope and geometry of the beam line) and P_{mistag} depends on the beam and detector characteristics (time resolution and efficiency). The mis-tagging happens if:

- the pileup beam track is present in the time window $|\Delta T| < 0.6$ ns;
- GTK reconstruction provides this track as a *kaon candidate*;
- the event survives the pileup treatment (quality criteria as explained in section 4.2.1);

- the reconstructed pileup track is matched to a downstream π^+ of 15-35 GeV/c momentum ($P_{K-\pi}^{matching}$).

The first three items representing the reconstructed pileup ($P_{pileup}^{reco}(\lambda)$) depend on the beam intensity (λ), while the suppression probability ($P_{K-\pi}^{matching}$) depends only on ΔT and CDA:

$$P_{mistag}(\lambda) = P_{pileup}^{reco}(\lambda) \cdot P_{K-\pi}^{matching}. \tag{5.12}$$

The pion upstream from GTK3 within 15-35 GeV/c momentum range ($N_{\pi^+}^{upstream}$) multiplied by reconstruction pileup (P_{pileup}^{reco}) are already represented by the sample C, used for the upstream background estimation. Hence, the estimation reduces to:

$$N_{upstream}^{bkg} = \sum_{i=0}^{12} N_C(|\Delta T_i|) \cdot P_{K-\pi}^{matching}(|\Delta T_i|) \cdot f_{scale}, \tag{5.13}$$

where the sum over index i runs over twelve 100 ps wide bins $i \times 50$ ps $< |\Delta T_i| < (i+1) \times 50$ ps covering the 1.2 ns window (0.6, 0.6) ns, $N_C(|\Delta T_i|)$ is a number of events in Sample C for the corresponding bin and f_{scale} is a scaling factor to correct for the $CDA > 4$ mm cut in the definition of Sample C.

A special MC simulation, with the kaons decaying to $\pi^+\pi^0$ upstream of GTK3 has been developed to evaluate the mis-matching probability $P_{K-\pi}^{matching}$.This requires to understand the PDF shapes of the KTAG time, GTK time, RICH time and CDA distributions. The RICH and KTAG times are simulated using a Gaussian PDF with resolutions $\sigma_{RICH} = 110$ ps and $\sigma_{KTAG} = 80$ ps. These resolutions are obtained from data. The GTK time is generated uniformly in a 1.2 ns time window centered at 0, which is the expected distribution for the pileup tracks. Different CDA between $Type$ 1 and $Type$ 2 events leads to different suppression from the STRAW-GTK matching. Therefore, the predictions are tested separately. As mentioned before, $Type$ 2 events are, after the *box cut*, not contributing to a background for the $\pi\nu\nu$ measurement. Shape of the CDA from $Type$ 1 MC sample C is used for P_{mistag}. The simulation reproduces the CDA distribution in different geometrical regions with a good accuracy, as illustrated in Fig. 5.10 where data/MC comparison for C, $D1$, $D2$ samples is shown.

The resulting suppression functions $P_{K-\pi}^{matching}$ for $Type$ 1 and $Type$ 2 events are shown in Fig. 5.11. Uncertainty of 10% is assigned to $P_{K-\pi}^{matching}$ due to limited size of the samples from which the CDA PDFs are extracted. Systematic uncertainty induced by the signal PDFs used in $K-\pi$ matching is 6%. The scaling factor f_{scale} for events in sample $D1$, $D2$ and C are 1.11(3), 1.08(3) and 1.10(3), respectively.

Background validation and final estimation

To validate the upstream background estimation procedure based on eq. (5.13), two classes of validation samples are defined. The first class has samples using the complete $\pi\nu\nu$ selection:

- Sample 1: $B1$ prediction obtained from events in sample $D_1 - N_{D_1}(|\Delta T|)$ with CDA distribution of $Type$ 1 events found in geometrical region $D1$ used for $P_{K-\pi}^{matching}(|\Delta T|)$;

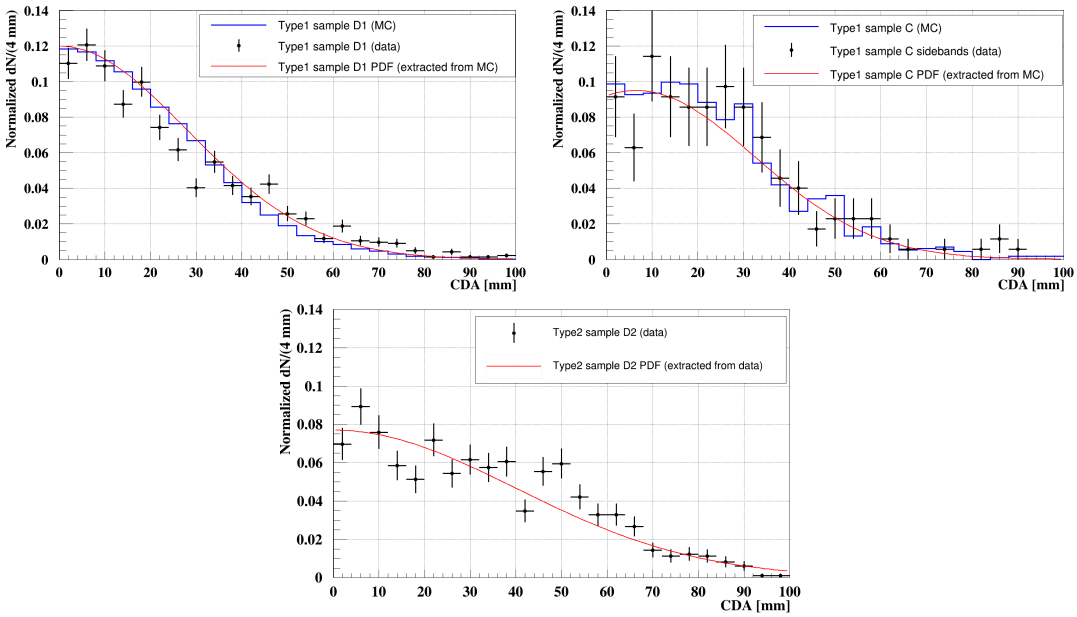

Figure 5.10: Top left: comparison of the CDA distribution between the $Type$ 1 events found in the geometrical region $D1$ extracted from a MC simulation (blue histogram) and a data sample with events from the geometrical region of $D1$ but in the side-bands of the ΔT distribution and with the $K-\pi$ matching inverted (black dots with error bars). The PDF used in the mistagging probability simulation is the fit of the MC distribution (solid red line). Top right: same comparison, but for events in geometrical region C. The resulting PDF (solid red line) extracted from the MC histogram (blue histogram) agrees with the data ($\chi^2/DoF = 0.6$) and it is the one used for the $\pi\nu\overline{\nu}$ background estimation. Bottom: CDA distribution of $Type$ 2 events taken from data in the geometrical region of the $D2$ sample but in the side-bands of the ΔT distribution and with $K-\pi$ matching inverted (blue dots with error bars). The PDF used in the mis-tagging probability simulation is the fit to the distribution (red solid line).

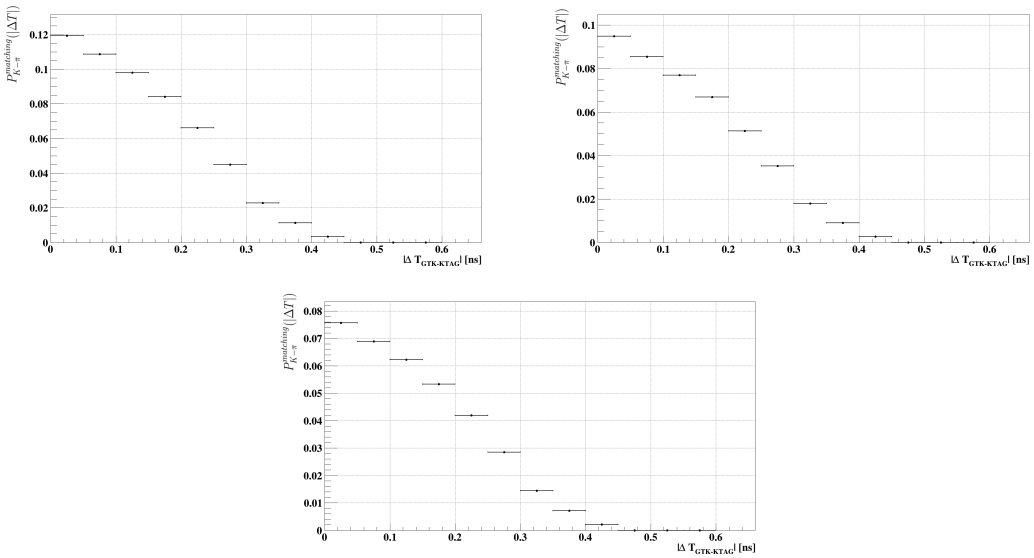

Figure 5.11: Top left: the mis-matching probability $P_{K-\pi}^{matching}$ as a function of $|\Delta T|$ for $Type$ 1 events in sample $D1$. Top left: $P_{K-\pi}^{matching}$ for $Type$ 1 events in sample C used for the upstream background estimation in the $\pi\nu\overline{\nu}$ signal region. Bottom: $P_{K-\pi}^{matching}$ for $Type$ 2 events.

- Sample 2: $B2$ prediction obtained from events in sample $D_2 - N_{D_2}(|\Delta T|)$ with CDA distribution of $Type$ 2 events used for $P_{K-\pi}^{matching}(|\Delta T|)$;
- Sample 3: A_{neg} prediction obtained from events in sample $C_{neg} - N_{C_{neg}}(|\Delta T|)$ with CDA distribution of $Type$ 1 events found in geometrical region C used for $P_{K-\pi}^{matching}(|\Delta T|)$;

The second class has samples using the complete $\pi\nu\nu$ selection with CHANTI veto and GTK extra hits cut not applied:

- Sample 4: $B1$ prediction obtained from events in Sample $D_1 - N_{D_1}(|\Delta T|)$ with CDA distribution of $Type$ 1 events found in geometrical region $D1$ used for $P_{K-\pi}^{matching}(|\Delta T|)$;
- Sample 5: $B2$ prediction obtained from events in Sample $D_2 - N_{D_2}(|\Delta T|)$ with CDA distribution of $Type$ 2 events used for $P_{K-\pi}^{matching}(|\Delta T|)$;
- Sample 6: A_{neg} prediction obtained from events in Sample $C_{neg} - N_{C_{neg}}(|\Delta T|)$ using the CDA distribution of $Type$ 1 events in Sample C extracted from MC for the determination of $P_{K-\pi}^{matching}(|\Delta T|)$;
- Sample 7: signal prediction (Sample A) obtained from events in sample $C_{neg} - N_{C_{neg}}(|\Delta T|)$ using the CDA distribution of $Type$ 1 events in Sample C extracted from MC for the determination of $P_{K-\pi}^{matching}(|\Delta T|)$;

Sample 7 contains the signal regions with the full $\pi\nu\nu$ selection, so it is masked. Comparison between expected and observed number of events is depicted in Fig. 5.12. It shows a good agreement across all 7 validation samples.

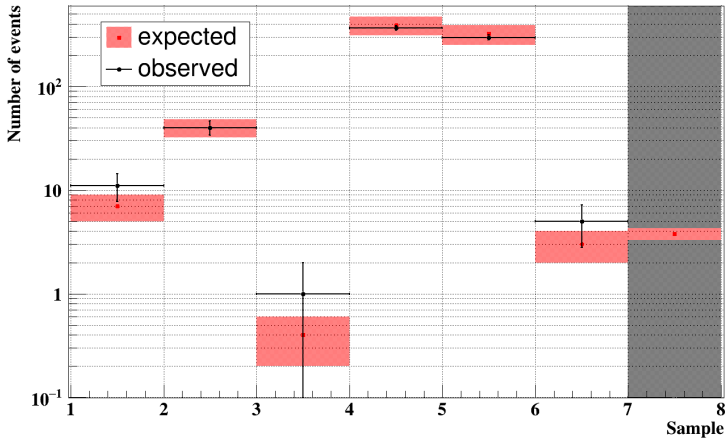

Figure 5.12: Validation of the Upstream background samples. The red boxes represent the expected number of events in the control region. The black dots correspond to number of events observed after unmasking this control region.

The total number of expected events from the upstream background is:

$$N_{upstream}^{expected} = 0.89 \pm 0.22_{stat} \pm 0.21_{syst}, \tag{5.14}$$

where the statistical uncertainty origins from the limited size of sample C, and systematic uncertainty comes from the $P_{K-\pi}^{matching}$ procedure which is dominated by the CDA distribution of $Type$ 1 events. An additional 20% uncertainty is assigned as half of the difference between the expected and observed number of events in Sample $B1$ to account for the accuracy of the method used for background estimation. The uncertainties are listed in Table 5.11.

Source	Relative uncertainty
Statistical (N_C)	25%
$P_{K-\pi}^{matching}$	12%
Validation	20%

Table 5.11: The error break-down for the $N_{upstream}^{expected}$.

5.7 Background with positrons

5.7.1 Study of RICH electron rejection

To reach a sensitivity of the possible electron backgrounds at the level needed for the $\pi\nu\nu$ analysis, it is important to understand differences between the data and simulation of electrons in the RICH. Hence, a clean electron sample from the data is needed, which can be compared with the simulation. As the best source of electrons the π^0 Dalitz decay might appear, but there are more positively charged particles in the final state, which could bias the measurement of the single ring efficiency. The other promising source of electrons is the K_{e3} decay, where one

	MC			
Condition	K_{e3}	$K_{\mu 3}$	$K_{2\pi}$	$K^{00}_{3\pi}$
Generated	26010358	8376139	31425006	40150547
No PID	528480	346	150	69
RICH PID	4	0	73	68
Calo PID	0	0	108	59
Full PID	0	0	62	59
$E/p > 0.8$	523915	0	7	5
BR	0.05	0.034	0.21	0.018
$\mathrm{Acc}_{electron}$	0.0201(3)	0	$(2.2(8)) \cdot 10^{-7}$	$(1.3(6)) \cdot 10^{-7}$

Table 5.12: Particle identification cut efficiencies studied on MC for several different modes. The estimation of acceptances of the K_{e3} selection for signal and the most significant backgrounds after the $E/p > 0.8$ cut is given in the last row.

can estimate the background with high accuracy. The K_{e3} sample selection is described in Appendix A.3.

The contamination of the electron sample by pions and muons from $K_{2\pi}$, $K_{\mu 3}$, $K_{3\pi}$, $K_{3\pi^{00}}$, and $K_{\mu 2}$ decays has been studied, and the acceptance of the signal K_{e3} is estimated with the MC simulation. Several approaches have been tested to maximize signal over background ratio. The best performance has been achieved when the associated LKr cluster energy ratio with the track momentum (E/p) is larger than 0.8. Table 5.12 outlines the major background sources together with the signal acceptance.

The number of kaons from the K_{e3} sample is obtained as $N_K = \dfrac{N_{K_{e3}}}{Acc \times BR}$ and the impurities from other modes as: $N = N_K \cdot Acc \cdot BR$. The impurities in the K_{e3} sample in data are under control when imposing an E/p condition on the track. Table 5.7.1 summarizes the number of reconstructed K_{e3} candidates for different data samples, corresponding impurities from other processes and the final electron rejection of RICH.

The electron sample from the MC was extracted from the $N^{gen}_{<105,165>} \simeq 7 \cdot 10^6$ K_{e3} decays. The selection has a simplified selection criteria, imposing no condition on the π^0 and E/p, to get as large sample as possible. It requires the following:

- Kinematic tails;
- Beam Background cut;
- $Z_{\pi^+} \in (105, 165)$;
- No CHANTI;
- No MUV3 within 7 ns;
- NRings == 1;
- RICH Single ring;
- No Straw segments.

DATA					
Condition	2017A	2017B	2017C	2017D	All
No PID	401387	648411	105213	175369	1330380
RICH PID	491	742	107	198	1538
Calo PID	426	646	92	169	1333
RICH&Calo PID	391	592	85	157	1225
LKr $E/p > 0.8$	396439	641208	103918	173201	1314766
$E/p > 0.8$&RICH	25	31	8	12	76
Pion impurities with electron ID					
$K_{2\pi}$	18.2 ± 6.6	29.5 ± 10.7	4.8 ± 1.7	8.0 ± 2.9	60.4 ± 22.0
$K_{3\pi}^{00}$	0.8 ± 0.4	1.3 ± 0.6	0.2 ± 0.1	0.3 ± 0.2	2.6 ± 1.3
Total	19.0 ± 6.6	30.8 ± 10.7	5.0 ± 1.8	8.3 ± 2.9	63.0 ± 22.0
RICH Eff (10^{-5})	1.6 ± 2.1	0.03 ± 1.9	2.9 ± 3.2	2.1 ± 2.3	< 3.2

Table 5.13: Number of the reconstructed K_{e3} events from different periods, background contamination and the final RICH electron mis-interpretation as pion. The limit on the overall RICH efficiency is obtained with the CLs method at 68% confidence level.

The obtained electron sample contains 5748855 events resulting in the pion mis-identification at the level of $(1 \pm 0.1) \times 10^{-5}$, in agreement with the value obtained from data.

5.7.2 $K^+ \to \pi^+\pi^0_D$ background

The study of the $K^+ \to \pi^+\pi^0_D$ decay is performed on a MC sample containing almost 50M generated events, out of which 37200684 decay within (105,165) m range. The direct approach, i.e. applying run the standard $\pi\nu\nu$ selection, is sets only an upper limit on the expected background at the level of $\sim 2\times10^{-10}$, due to the limited MC sample size. Hence, to get the sensitivity at the level necessary for the $\pi\nu\nu$ analysis, one needs to factorize the background suppression. The $K^+ \to \pi^+\pi^0_D$ is a two body decay, kinematically same as $K_{2\pi}$, so the kinematic suppression factor $\varepsilon^{Kin} = 1.2 \pm 0.1 \cdot 10^{-3}$ measured on the $K_{2\pi}$ data can be used. The photon rejection is expected to be worse compared to the $\pi^0 \to \gamma\gamma$ final state, but one gains a factor ~ 100 owing to the π^0_D branching fraction. The total estimated efficiency of the $K^+ \to \pi^+\pi^0_D$ event reconstruction as a $\pi\nu\nu$ is:

$$\varepsilon^{Total} = BR(\pi^0_D) \times \varepsilon^{Kin} \times \varepsilon^{Selection} \times \varepsilon^{Multi} \times \varepsilon^{PR}, \tag{5.15}$$

where $BR(\pi^0_D) = 0.01174$ is the branching fraction, ε^{Kin} is the kinematic suppression, $\varepsilon^{Selection}$ is the selection efficiency, ε^{Multi}, ε^{PR} are the multiplicity and photon rejections, explained below.

Selection follows the same strategy as the $\pi\nu\nu$ analysis, but photon and multiplicity rejection is applied separately. The efficiency of the selection has been measured to be $\varepsilon^{Selection} = (1.9 \pm 0.002) \cdot 10^{-2}$. After this selection, multiplicity and photon rejection conditions, explained in sections 4.3.5 and 4.3.7, are applied independently on the MC sample. The rejection power for $K_{2\pi_D}$ is $\varepsilon^{Multi} = (2.9 \pm 0.04) \cdot 10^{-2}$. Resulting photon rejection in case of the $K_{2\pi_D}$ is $\varepsilon^{PR} = (9 \pm 3.6) \cdot 10^{-6}$.

ε^{Kin}	$\varepsilon^{Selection}(10^{-2})$	$\varepsilon^{Multi}(10^{-2})$	$\varepsilon^{PR}(10^{-6})$	$BR(K_{2\pi} \cdot \pi^0_D)$
$1.2 \cdot 10^{-3}$	1.9 ± 0.002	2.9 ± 0.04	9 ± 3.6	$2.5 \cdot 10^{-3}$

Table 5.14: Values entering the calculation of ε^{Total} for $K_{2\pi_D}$. The errors not listed are negligible compared to the others and were thus ignored.

Combining the efficiencies summarized in table 5.14 with the branching ratios of K_π and π^0_D leads to the total efficiency:

$$\varepsilon^{Total} = (1.5 \pm 0.6) \cdot 10^{-14}. \tag{5.16}$$

The estimation on the number of expected events in the 2017 data sample is obtained by taking into account also the trigger efficiency:

$$N_{expected} = \varepsilon^{Total} \times N_K \times \varepsilon^{Trig} = 0.016 \pm 0.006. \tag{5.17}$$

5.7.3 $K^+ \to \mu^+\nu;\ \mu^+ \to e^+\nu\bar{\nu}$ background

The background has been studied on a MC sample with a capped muon lifetime, where the proper lifetime of the muon does not exceed 0.73% of the mean muon lifetime ($\tau_\mu = 2.2\mu$s). The scaling introduced by the capped muon lifetime is: $\frac{1}{1 - e^{(-0.73\%)}} = 137.487$. Total number of 50M generated and reconstructed events have been used in this study. This size of the sample is not large enough for a direct background estimation, so one needs to proceed with factorization. The sample is divided into the different Z_{vertex} ranges defined according to the true $\mu \to e$ decay. These ranges correspond to sections before the second STRAW chamber, three 10 meter parts with the chambers 2,3,4 and last part after the fourth chamber. The factorization is done in the following way:

$$\varepsilon^{Total} = BR \times \left[\sum \varepsilon_i^{Decay} \times \varepsilon_i^{Sel} \times \varepsilon_i^{RICH} \times \varepsilon_i^{Calo} \times \varepsilon_i^{Kin}\right] \times \varepsilon^{RV} \times \varepsilon^{Trig} \tag{5.18}$$

where $BR(K_{\mu 2}) = 0.6356$ is the $K_{\mu 2}$ branching fraction, ε^{RV} and ε^{Trig} were defined at the beginning of this chapter, ε_i^{Decay} is a probability of the $\mu \to e$ decay, ε_i^{Sel} includes the geometrical and selection acceptances, ε_i^{RICH} and ε_i^{Calo} are the probabilities of the electron mis-identification as pion in RICH and LKr and finally ε_i^{Kin} is a fraction of events ending up in the $\pi\nu\nu$ kinematic region. The sum runs over the different Z_{vertex} regions represented by the index i. All the ingredients for the background estimation are summarized in Table 5.15. For the full 2017 data set of $(12 \pm 1) \times 10^{11}$ kaon decays, the final expected number of background events in different ranges are reported in Table 5.7.3.

The total expected background from $K_{\mu 2};\ \mu \to e$ is:

$$N_{expected} = 0.07 \pm 0.03 \ \ events,$$

where the last range (> 220) is excluded as it is already taken into account in the $K_{\mu 2}$ background estimation.

Range [m]	ε^{Decay} ($\times 10^{-4}$)	ε^{Sel} ($\times 10^{-3}$)	ε^{RICH} ($\times 10^{-4}$)	ε^{Calo} ($\times 10^{-3}$)	ε^{Kin} ($\times 10^{-2}$)
< 190	3.90 ± 0.01	1.73 ± 0.03	0.3	3.9 ± 1.0	62.8 ± 0.8
$190 - 200$	0.71 ± 0.01	5.6 ± 0.1	0.3	6.6 ± 1.8	52.3 ± 1.1
$200 - 210$	0.72 ± 0.01	7.0 ± 0.1	0.3	2.6 ± 1.0	20.2 ± 0.8
$210 - 220$	0.73 ± 0.01	6.1 ± 0.1	17 ± 8	2.5 ± 1.0	3.1 ± 0.4
> 220	6.00 ± 0.01	11.74 ± 0.06	26 ± 3	2.7 ± 0.3	0.02 ± 0.0007

Table 5.15: Various efficiencies contributing to the evaluation of ε^{Total} as defined by Eq. 5.18 for different ranges.

Range [m]	$[\sum] \times 10^{-14}$	$\varepsilon^{Total} \times 10^{-14}$	$N_{expected}$
< 190	4.9 ± 1.3	1.7 ± 0.5	0.020 ± 0.006
$190 - 200$	4.1 ± 1.1	1.4 ± 0.4	0.017 ± 0.005
$200 - 210$	0.8 ± 0.3	0.3 ± 0.1	0.004 ± 0.001
$210 - 220$	5.9 ± 3.9	2.1 ± 1.4	0.025 ± 0.018
> 220	0.9 ± 0.1	0.3 ± 0.1	0.004 ± 0.002

Table 5.16: Expected background of background events in different ranges.

In the $\pi\nu\nu$ analysis is used not only the kinematic signal region defined by the m^2_{miss} from GTK-STRAW matching, but also the ones from GTK-RICH $m^2_{miss}(RICH)$ and nominal beam momentum with STRAW $m^2_{miss}(Beam)$ matching, as defined in eq. (3.6). It is not possible to perform an exact evaluation of the additional suppression from the $m^2_{miss}(RICH)$, as it is will be correlated with the ε^{RICH} and the factorization in (5.18) would not hold. Due to the limited size of MC sample, it is not feasible to estimate the correlation on this sample. However, it has been studied on the standard $K_{\mu 2}$ control sample. The number of $K_{\mu 2}$ events in $\pi\nu\nu$ regions has been evaluated after the application of RICH PID, including or not $m^2_{miss}(RICH)$ and $m^2_{miss}(Beam)$ cuts, resulting in factor 0.51 ± 0.04. This factor in reality under-estimates the effect if the muon decay happens after the spectrometer magnet. This is because the direction of the muon from the first two chambers and the speed of the positron after the decay will be taken. Now one has to correct the estimated number of expected background by this factor. The calculated factor is directly applied, even though it over-estimates the background as explained before. The final background estimation from $K_{\mu 2}, \mu \to e$ is:

$$N^{final}_{expected} = 0.036 \pm 0.016 \;\; events. \tag{5.19}$$

5.7.4 $K^+ \to e^+\nu$ background

The study of this background was performed on the standard K_{e2} MC with 10M events. The suppression is based mainly on the kinematics and particle identification in the RICH and the calorimeters. The key kinematic variable is the squared missing mass: $m^2_{miss} = (P_{K^+} - P_{\pi^+})^2$, where P_{K^+} is a 4-momentum of the kaon track and P_{π^+} is a 4-momentum of the downstream track in the pion mass hypothesis. The kinematics of the process is illustrated in Figure 5.13. The

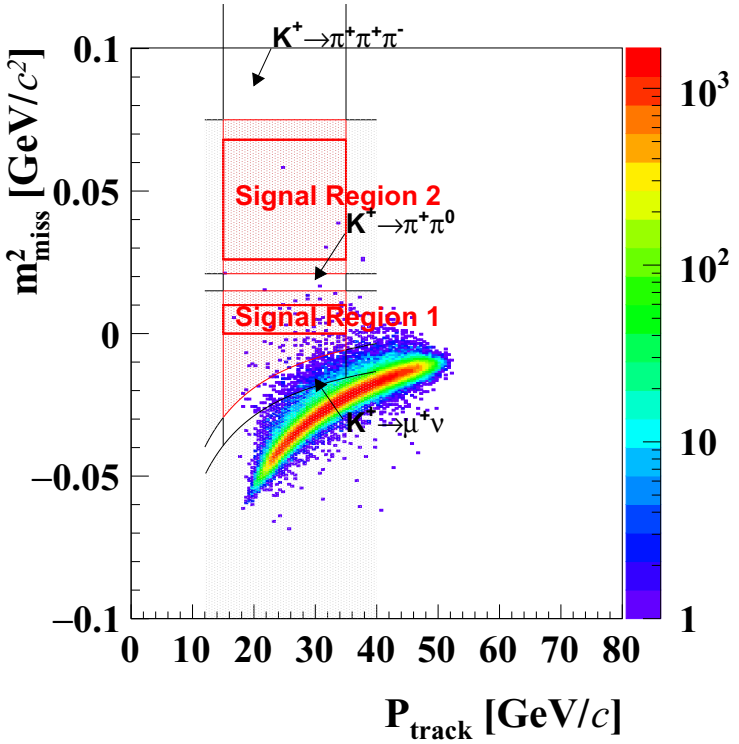

Figure 5.13: The distribution of the m^2_{miss} in the pion mass hypothesis as a function of the downstream track momentum.

process is factorized accordingly:

$$\varepsilon^{Total} = BR(K_{e2}) \times \varepsilon^{Selection} \times \varepsilon^{ParticleID} \times \varepsilon^{RV} \times \varepsilon^{Trig}, \tag{5.20}$$

where $BR(K_{e2}) = 1.582 \times 10^{-5}$ is the K_{e2} branching fraction, $\varepsilon^{Selection}$ is the efficiency of the $\pi\nu\nu$ selection on K_{e2} including kinematics, $\varepsilon^{ParticleID} = \varepsilon^{RICH}$. ε^{Calo} is the suppression from the RICH and calorimeters, and ε^{RV}, ε^{Trig} are the efficiencies of the random veto and trigger measured on the data. The factors have been measured to be:

- $\varepsilon^{Selection} = (3.2 \pm 0.7) \times 10^{-6}$ - measured on the K_{e2} MC;
- $\varepsilon^{ParticleID} = \sim 10^{-6}$ - measured on the K_{e3} MC, validated with the data;
- $\varepsilon^{RV} = 0.63$, $\varepsilon^{Trig} = 0.87$, $BR(K_{e2}) \sim 10^{-5}$.

Combining the above numbers one gets the suppression of K_{e2} decay at the level of $\sim 10^{-17}$ which is negligible for the $\pi\nu\nu$ analysis.

5.7.5 $K^+ \to \pi^0 e^+ \nu_e$ (K_{e3}) and $K^+ \to \pi^0 \mu^+ \nu_\mu$ ($K_{\mu 3}$) background

The estimation of these backgrounds is performed with the procedure established for $K^+ \to \mu^+\nu$; $\mu^+ \to e^+\nu\bar{\nu}$ background without any Z-position dependence, with the following factorization:

$$\varepsilon^{Total} = BR \times \varepsilon^{Sel} \times \varepsilon^{RICH} \times \varepsilon^{Calo} \times \varepsilon^{Kin} \times \varepsilon^{RV} \times \varepsilon^{Trig}. \tag{5.21}$$

Then, by multiplying ε^{Total} with the number of kaons one gets the estimated background.

K_{e3} background

The branching ratio is $BR(K_{e3}) = 0.0507$, $\varepsilon^{RV} = 0.64$, $\varepsilon^{Trig} = 0.87$ and the remaining factors in eq. (5.21) are:

$$\varepsilon^{Sel} = (5.3 \pm 1.4) \cdot 10^{-7}; \quad \varepsilon^{RICH} = 3.2 \cdot 10^{-5}; \quad \varepsilon^{Calo} = (2.84 \pm 0.02) \cdot 10^{-3}. \quad (5.22)$$

Combining with the number of kaon decays, the total expected background from K_{e3} is:

$$N_{expected} = 0.0002 \pm 0.0002, \quad (5.23)$$

where the uncertainty is the convolution of the statistical uncertainties on all the factors measured on MC samples. This background is negligible for the $\pi\nu\nu$ analysis.

$K_{\mu 3}$ background

The branching ratio is $BR(K_{\mu 3}) = 0.03352$, $\varepsilon^{RV} = 0.64$ and $\varepsilon^{Trig} = 0.87$. Then, exploiting MC simulation,all the other factors have been estimated:

$$\varepsilon^{Sel} = (8.3 \pm 2.4) \cdot 10^{-7}; \quad \varepsilon^{Calo} = (0.99 \pm 0.02) \cdot 10^{-5}, \quad (5.24)$$

while the RICH PID rejection factor is directly taken from data (measured on $K_{\mu 2}$ sample): $\varepsilon^{RICH} = 2.1 \cdot 10^{-3}$.

Combining with the number of kaon decays, the total expected background from K_{e3} is:

$$N_{expected} = 0.0004 \pm 0.0004, \quad (5.25)$$

where again, the uncertainty is the convolution of the statistical uncertainties on all the factors measured on MC samples. This background is also negligible for the $\pi\nu\nu$ analysis.

5.8 Background summary

The summary of all studied backgrounds integrated in R1 and R2, is presented in Table 5.17. The dominant contribution comes from the upstream backgrounds and a serious effort is made to mitigate this component in future.

5.8.1 Final background validation

The final validation is performed in the m^2_{miss} signal regions, but for the momentum range of 35-40 GeV/c. The expected number of events in the m^2_{miss} compatible with R1 and R2 is:

$$N^{background}_{expected} = 0.62 \pm 0.13 \quad (5.26)$$

$$N^{signal}_{expected} = 0.13 \pm 0.01. \quad (5.27)$$

After unmasking these control regions, one event is observed over the m^2_{miss} R2, in agreement with the prediction. The distribution of events in (p, m^2_{miss}) plane after uncovering all of the control regions is shown in Fig. 5.14.

Process	Expected events in signal regions
$K^+ \to \pi^+\pi^0(\gamma)$ IB	$0.29 \pm 0.03_{stat} \pm 0.03_{syst}$
$K^+ \to \mu^+\nu_\mu(\gamma)$ IB	$0.11 \pm 0.02_{stat} \pm 0.03_{syst}$
$K^+ \to \mu^+\nu_\mu(\mu^+ \to e^+\nu_e\bar{\nu}_\mu)$	$0.04 \pm 0.02_{syst}$
$K^+ \to \pi^+\pi^-e^+\nu_e$	$0.12 \pm 0.05_{stat} \pm 0.03_{syst}$
$K^+ \to \pi^+\pi^+\pi^-$	$0.02 \pm 0.02_{syst}$
$K^+ \to \pi^+\gamma\gamma$	$0.005 \pm 0.005_{syst}$
$K^+ \to \ell^+\pi^0\nu_\ell$	negligible
$K^+ \to e^+\nu_e$	negligible
Upstream background	$0.9 \pm 0.2_{stat} \pm 0.2_{syst}$
Total background	$1.5 \pm 0.2_{stat} \pm 0.2_{syst}$

Table 5.17: List of background contributions to $\pi\nu\nu$ signal process.

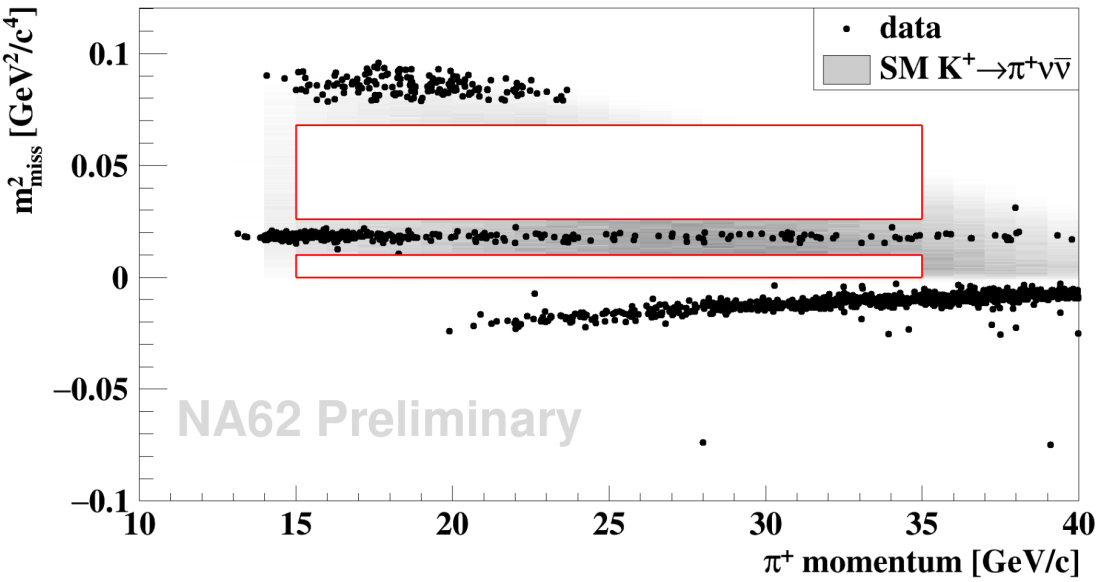

Figure 5.14: The distribution of events after unmasking control regions. Signal regions are kept masked.

6. $K^+ \to \pi^+ \nu\bar{\nu}$ analysis

This chapter describes the procedure to obtain the Single Event Sensitivity (SES) and expected number of $K^+ \to \pi^+ \nu\bar{\nu}$ events from the 2017 data set. All ingredients entering the SES calculation, like the number of kaon decays, acceptances, trigger efficiencies and random veto are studied. The systematic errors related to these studies are evaluated.

6.1 Single Event Sensitivity

The SES for the $\pi\nu\nu$ is:

$$SES = \frac{BR(K^+ \to \pi^+ \nu\bar{\nu})}{N_{\pi\nu\nu}}, \tag{6.1}$$

where $BR(K^+ \to \pi^+ \nu\bar{\nu}) = (8.4 \pm 1.0) \times 10^{-11}$ is the $\pi\nu\nu$ branching ratio and $N_{\pi\nu\nu}$ is the SM number of $\pi\nu\nu$ events expected to be reconstructed after the selection. The latter depends on the number of kaon decays, N_K, and the overall $\pi\nu\nu$ decay reconstruction efficiency $\mathcal{A}_{\pi\nu\nu}$:

$$N_{\pi\nu\nu} = N_K \cdot \mathcal{A}_{\pi\nu\nu} \cdot BR(K^+ \to \pi^+ \nu\bar{\nu}). \tag{6.2}$$

The number of kaon decays is extracted from the normalization channel. The standard normalization channel for the $\pi\nu\nu$ analysis is the $K^+ \to \pi^+\pi^0$ decay selected on control data using criteria similar to $\pi\nu\nu$, except photon and multiplicity rejection and kinematical cuts. An alternative normalization channel $K^+ \to \mu^+\nu$ is also studied. In this case, photon and multiplicity rejection are included, but particle identification in RICH and calorimeters is not applied, signal in MUV3 compatible with the track is required and $K_{\mu 2}$ kinematical region is used. The number of expected events reads:

$$N_{\pi\nu\nu} = N_{norm} \frac{\mathcal{A}_{\pi\nu\nu} \cdot BR(K^+ \to \pi^+ \nu\bar{\nu})}{\mathcal{A}_{norm} \cdot BR(norm)}, \tag{6.3}$$

where N_{norm} is the number of reconstructed normalization events, $\mathcal{A}_{norm}$ is the overall efficiency to reconstruct the normalization sample and $BR(norm)$, with $BR(K^+ \to \pi^+\pi^0) = 0.2056$ and $BR(K^+ \to \mu^+\nu) = 0.6356$, is the branching ratio of the normalization mode $K_{2\pi}$ and $K_{\mu 2}$, respectively.

6.2 Efficiencies

The overall efficiency of the $\pi\nu\nu$ reconstruction is obtained by multiplying different factors. One can factorize the efficiency into:

$$\mathcal{A}_{\pi\nu\nu} \simeq \varepsilon_{det} \cdot \varepsilon_{sel} \cdot \varepsilon_{Random} \cdot \varepsilon_{trig}, \tag{6.4}$$

where

- ε_{det} is the detector efficiency (of detection and reconstruction) of

– KTAG, GTK, STRAW, RICH, NewCHOD, CHOD, LKr;

- ε_{sel} is the selection efficiency:

$$\varepsilon_{sel} \simeq A_{\pi} \cdot \varepsilon_{PID}(Calo,\ RICH) \cdot \varepsilon_{veto}(\pi - induced) \cdot \varepsilon_{K}(K - ID,\ K - \pi), \quad (6.5)$$

where

– $A(\pi)$ is the charged pion acceptance taking into account the geometry, kinematic selection, time/spatial matching, etc.;

– $\varepsilon_{PID}(Calo,\ RICH)$ is the efficiency of the pion identification using the calorimeters and RICH;

– $\varepsilon_{veto}(\pi - induced)$ estimates the fraction of event loss due to pion interactions and decays;

– $\varepsilon_{K}(K - ID,\ K - \pi)$ represents the kaon identification and the kaon-pion matching efficiencies;

- ε_{Random} is the random veto efficiency:

$$\varepsilon_{Random} \simeq \varepsilon_{RV}(\gamma - veto) \cdot \varepsilon_{RV}(\pi - mult) \cdot \varepsilon_{RV}^{MUV3} \cdot \varepsilon_{RV}^{CHANTI} \cdot \varepsilon_{RV}(K - mult), \quad (6.6)$$

where

– $\varepsilon_{RV}(\gamma - veto)$ combines an extra in-time activity in the LKr, LAV, SAC and IRC. It rejects an event if there is some energy deposited in LAV(IRC, SAC) within 3(7) ns, with respect to the π^+ track. Also events with a LKr cluster beyond 100 mm from the π^+ impact point location and within time windows ranging from $\pm$5 ns for cluster energies below 5 GeV to $\pm$50 ns above 15 GeV are rejected.

– $\varepsilon_{RV}(\pi - mult)$ is a set of conditions aiming to suppress activity in detectors induced by an extra charged particle. It contains the conditions on the single track in the STRAW spectrometer and no additional segments reconstructed in STRAW compatible with the decay vertex. Furthermore, it checks the in-time activity in the CHOD and NA48-CHOD unrelated to the π^+ , but in the spatial coincidence with an energy deposit of at least 40 MeV in the LKr. Finally, it rejects the events with in-time signals in the HASC and MUV0 and more than three signals in the NA48-CHOD in-time with the π^+.

– ε_{RV}^{MUV3} is the fraction of events rejected due to the in-time activity in the MUV3.

– $\varepsilon_{RV}^{CHANTI}$ estimates the fraction of rejected events within 3 ns of the π^+ in the CHANTI.

– $\varepsilon_{RV}(K - mult)$ is the efficiency of the upstream multiplicity cut: less than five GTK tracks reconstructed within 2 ns of the KTAG time.

- $\varepsilon_{trig} \simeq \varepsilon_{L0} \cdot \varepsilon_{L1}$ accounts for the trigger efficiencies of L0 and L1, see more details in 6.2.1.

The overall efficiency of the $K_{2\pi}$ reconstruction, used as a normalization, can be written in the same way as for $\pi\nu\nu$:

$$\mathcal{A}_{2\pi} \simeq \varepsilon_{det} \cdot \varepsilon_{sel} \cdot \varepsilon_{Random} \cdot \varepsilon_{trig}, \tag{6.7}$$

where most of the factors are identical, except for:

- in $\varepsilon_{veto}(\pi - induced)$ only pion decays are taken into account, not interactions.
- ε_{Random} contains only ε_{RV}^{MUV3}, $\varepsilon_{RV}^{CHANTI}$ and $\varepsilon_{RV}(K - mult)$ which are the same as for $\pi\nu\nu$.

Trigger efficiency of the control trigger used for the normalization is assumed to be one, relative to PNN mask. To verify this statement several steps are undertaken. First, the number of $K_{\mu 2}$ events after the full $\pi\nu\nu$ selection without applying the RICH conditions (Calo PID and no associated MUV3 candidate still applied) from the control ($N_{\mu 2}^{ctrl}$) and PNN trigger masks ($N_{\mu 2}^{PNN}$) is counted. Then $N_{\mu 2}^{PNN}$ is compared with the corresponding number expected from $N_{\mu 2}^{ctrl}$:

$$N_{\mu 2}^{PNN}(expected) = D \cdot N_{\mu 2}^{ctrl} \cdot \varepsilon_{L0} \cdot \varepsilon_{L1}. \tag{6.8}$$

Further, from the full 2017 data set one gets:

$$\begin{aligned} &N_{\mu 2}^{PNN} = (256.0 \pm 0.5) \times 10^3; \quad N_{\mu 2}^{ctrl} = (710 \pm 27); \quad D = 400; \\ &\varepsilon_{L0} \approx 0.983; \quad \varepsilon_{L1} \approx 0.955; \quad N_{\mu 2}^{PNN}(expected) = (267 \pm 10) \times 10^3. \end{aligned} \tag{6.9}$$

The expected and measured central values of $N_{\mu 2}^{PNN}$ differs by 4% relative to each other and agrees within the error which is dominated by the statistics on the control trigger. As a result, $\pm 4\%$ relative systematic uncertainty is assigned to the L0 trigger efficiency. The value can be in principle improved using another sample for testing.

In the SES computation, only the ratio of the signal and normalization channel enters, so the factors which are the same will cancel out and one can write:

$$N_{\pi\nu\nu}(P, I) = \frac{D \cdot N_{2\pi}^{ctrl}(P, I) \cdot \varepsilon_{RV}(I) \cdot \varepsilon_{trig}(P, I) \cdot A_{\pi\nu\nu}^{MC}(P) \cdot BR(\pi\nu\nu)}{A_{2\pi}^{MC}(P) \cdot BR(2\pi) + A_{bkg}^{MC}(P) \cdot BR(bkg)} \tag{6.10}$$

where the dependence on intensity I and momentum P is explicitly written. Here, $D = 400$ is the down-scaling of the control trigger and bkg refers to the $K_{2\pi}$ sample with π^0 Dalitz decay. $A_{\pi\nu\nu}^{MC}$ and $A_{2\pi}^{MC}$ are the acceptances obtained from the MC and represent the product of $\varepsilon_{sel} \cdot \varepsilon_{det}$ with the differences mentioned above. All of the terms entering equation 6.10 are known, or can be measured, precisely.

6.2.1 Trigger Efficiency

The level zero trigger (L0) efficiency measurement was done separately for the electromagnetic calorimeter (L0Calo) and the other L0 detectors (L0NoCalo).

		15-20	20-25	25-30	30-35
<200 MHz	L0	0.951(3)	0.933(6)	0.915(4)	0.897(4)
200-300 MHz	L0	0.950(3)	0.931(4)	0.913(4)	0.896(4)
300-400 MHZ	L0	0.948(3)	0.930(4)	0.911(4)	0.894(5)
400-800 MHz	L0	0.945(4)	0.927(4)	0.909(4)	0.891(5)
>800 MHz	L0	0.938(4)	0.920(5)	0.902(5)	0.885(5)

Table 6.1: L0 trigger efficiencies in momentum and intensity bins.

Intensity [MHz]	<200	200-300	300-400	400-800	>800
L1 before run 8025	0.970(4)	0.960(5)	0.950(6)	0.931(9)	0.889(14)
L1 after run 8025	0.970(3)	0.965(4)	0.960(6)	0.950(8)	0.928(13)

Table 6.2: L1 trigger efficiencies in intensity bins before and after run 8025.

The L0NoCalo efficiency was measured on data using $K_{2\pi}$ or $K_{\mu 2}$ collected by control trigger and selected like $\pi\nu\nu$ events to evaluate the part uncorrelated to the $\pi\nu\nu$ selection.

For the L0Calo efficiency measurement a sample of $K_{2\pi}$ selected with both γs in LAV(2-12) and π^+ momentum above 40 GeV/c was used. The efficiency was then measured as a function of E_{LKr} converted in π^+ momentum using E/p from $\pi^+\pi^+\pi^-$ events. Finally the efficiency as a function of π^+ momentum in the 15-35 GeV/c range was extracted.

The level one trigger (L1) consists of L1KTAG, L1LAV and L1STRAW. These components were measured in addition to the $\pi\nu\nu$ selection mainly with $K_{\mu 2}$ events, using auto-pass, control and L1 trigger emulator. L1KTAG was found fully efficient and L1STRAW has about 1% inefficiency. L1LAV is intensity dependent and its efficiency decreases with intensity due to a non-negligible additional random veto in addition to the offline random veto. In 2017 there were two periods with different settings of the L1LAV. Before run 8025, the L1LAV was defined as a veto if there were few in-time hits within 10 ns wrt reference time in any of the LAV stations (1-12), while starting at run 8025 only signals from LAV stations 2-12 were taken into account.

All the numbers for combined L0 and L1 in the momenta and intensity bins are summarized in Tables 6.1 and 6.2. The first table presents L0 trigger efficiencies and the second L1 trigger efficiencies for the conditions before and after run 8025. The errors reported in the tables correspond only to the statistics.

A systematic uncertainty for the L0NoCalo trigger at the level of 4 per mile is considered due to nonhomogeneous variations in the intensity. Another 4 per mile from the L0Calo is assigned to systematics based on run-by-run spread of the efficiency. Moreover a relative 4% systematic uncertainty is added to the L0 trigger efficiency considering the relative trigger efficiencies of control trigger and PNN mask, as explained in section 6.2.

As the L1 trigger is not significantly momentum dependent, only a single value valid for the whole momentum range is reported. A small dependence at the level of 2 per mile in the L1STRAW is assigned to the systematic uncertainty of L1 trigger. The L1LAV systematic uncertainty of 1.4% is added based on the intensity dependence and run-by-run spread.

The product of L0 and L1 efficiencies enters in the SES calculation. It is

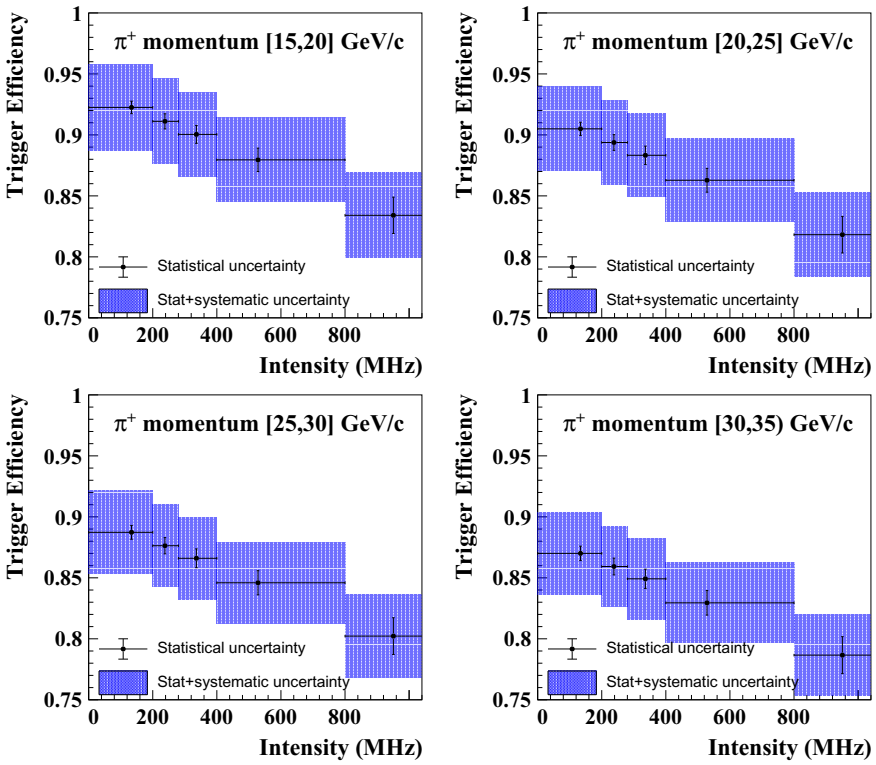

Figure 6.1: Total L0×L1 trigger efficiencies in bins of intensity in four momentum bins, with L1LAV conditions as defined before run 8025.

graphically represented in Figures 6.1 and 6.2 for the period before and after run 8025, respectively.

6.2.2 Random Veto ε_{RV}

The Random Veto (RV) is measured using the $K_{\mu 2}$ events selected from the control trigger. The $K_{\mu 2}$ sample used in this study is obtained using kinematics criteria and positive muon identification. The RV effect is calculated in the following way:

$$\varepsilon_{RV} = \frac{N_{\mu 2(after \gamma-veto, \pi-mult)}}{N_{\mu 2(before \gamma-veto, \pi-mult)}}. \tag{6.11}$$

This efficiency needs to be corrected for the muon induced loss originating from the δ-rays in RICH mirrors, leading to increase of the CHOD multiplicity:

$$\varepsilon_{RV} \rightarrow \varepsilon_{RV} + 1/2(1 - \varepsilon_{\mu}), \tag{6.12}$$

where $\varepsilon_{\mu} = 0.022$ was measured on $K_{\mu 2}$ MC. Systematic uncertainty assigned to the correction is: $\pm 1/2(1 - \varepsilon_{\mu})$. The stability of ε_{RV} was tested against variation of muon identification and kinematic cuts and the maximum observed relative excursion was 2.4%. An average value of $\pm 0.012 \cdot \varepsilon_{\mu}$ is taken and assigned as a systematic uncertainty. The dependence of ε_{RV} on momentum and intensity was also scrutinized and was found to be stable within ± 0.003 wrt the momentum and strongly dependent on the instantaneous beam intensity, as can be seen in Table 6.2.2 and Figure 6.3.

The summary of the results together with the breakdown of error budget is listed in Table 6.2.2.

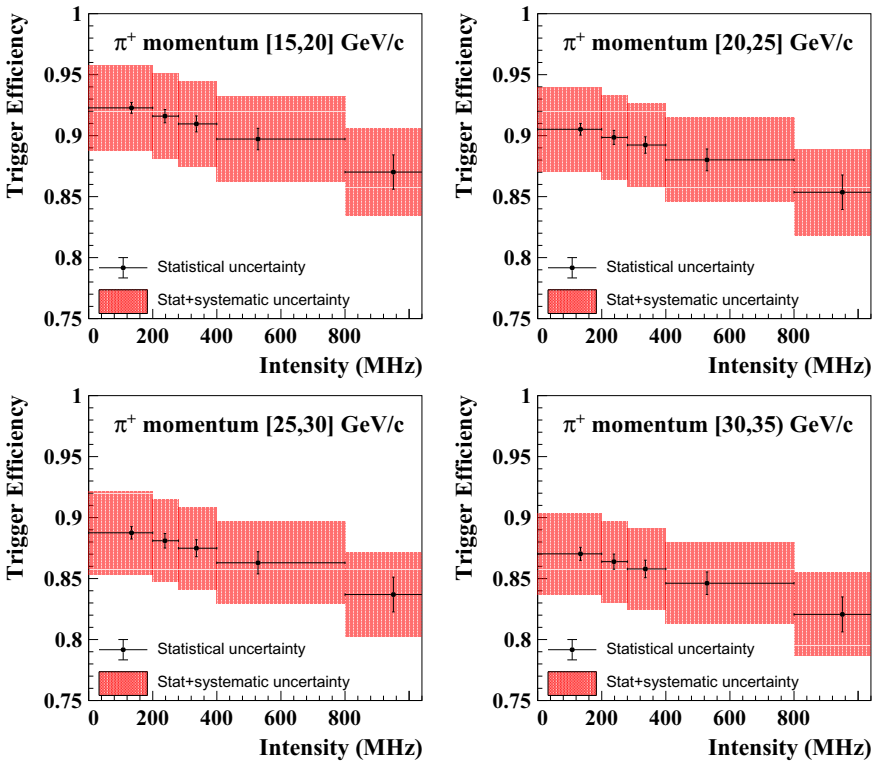

Figure 6.2: Total L0×L1 trigger efficiencies in bins of intensity in four momentum bins, with L1LAV conditions as defined after run 8025.

0-200 MHz	200-300 MHz	300-400 MHz	400-800 MHz	> 800 MHz
0.77005(8)	0.69756(9)	0.64222(7)	0.55467(6)	0.39724(22)

Table 6.3: Random veto rejection at the different beam intensities.

RV averaged over beam intensity	
$\varepsilon_{RV} = 0.638 \pm 0.014$	
Source	Uncertainty
$K_{\mu 2}$ interaction correction	± 0.011
μ identification	± 0.008
momentum dependence	± 0.003
statistics	< 0.001

Table 6.4: RV value and breakdown of its error budget.

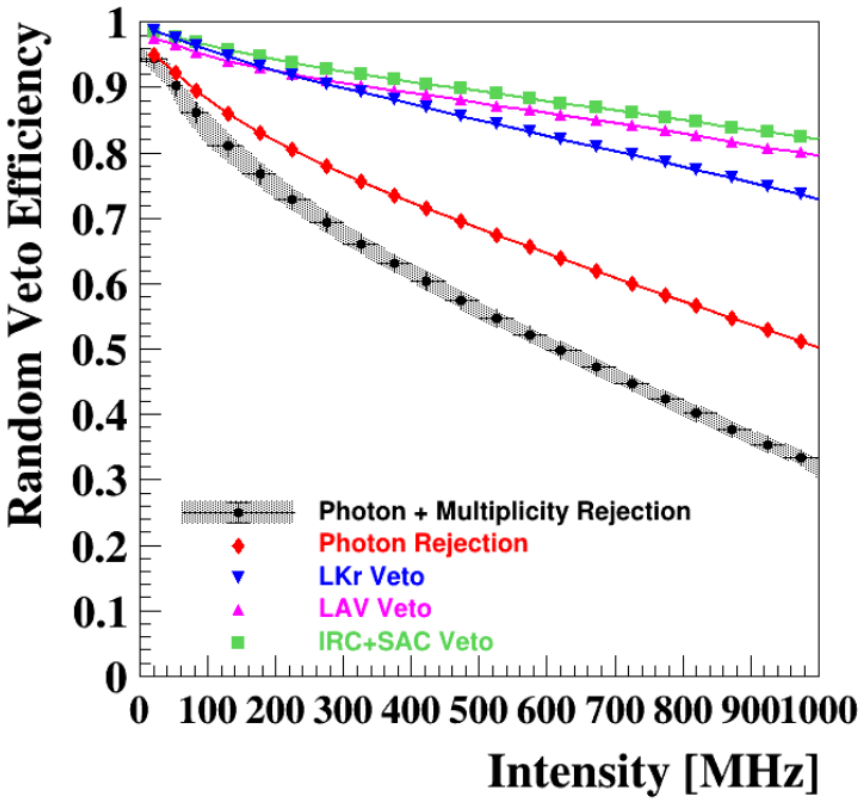

Figure 6.3: RV as a function of the instantaneous intensity. The single sub-detectors and combined effect are presented.

6.2.3 Pion induced veto $\varepsilon_{veto}(\pi - induced)$

The pion induced veto represents the inaccuracy of the simulation of the π^+ loss because of interactions due to the multiplicity and photon rejection cuts. As the extra activity in the detectors accounted for in ε_{RV} is measured on events with a muon track, the pion interaction effects are omitted. In reality, they are suppressed by the multiplicity cuts applied in the $\pi\nu\nu$ selection, but not in the $\pi\pi^0$ one.

To quantify the effect, the cross-check is performed between data and simulation on a specific sample of $\pi^+\pi^0$ selected with both γ's in LAV(2-11) and veto in LKr, LAV1,12, SAC.

The fraction of events surviving the π-multiplicity cuts measured on data is given by:

$$1 - \varepsilon_{mult}^{Data} = (1 - \varepsilon_{mult}^{int}) + (1 - \varepsilon_{mult}^{RV}), \tag{6.13}$$

where $1 - \varepsilon_{mult}^{int}$ corresponds to the loss of π^+ because of interactions due to the multiplicity cuts and $1 - \varepsilon_{mult}^{RV}$ is the loss of π^+ because of random activity due to the multiplicity cuts measured on data. On the MC sample, the measured effect is only due to the pion interactions, as the random activity is not simulated:

$$\varepsilon_{mult}^{MC} = \varepsilon_{mult}^{int}. \tag{6.14}$$

The cross-check of the data ($\varepsilon_{mult}^{int} = 1 + \varepsilon_{mult}^{Data} - \varepsilon_{mult}^{RV}$) with the MC ($\varepsilon_{mult}^{MC}$) shows a discrepancy, clearly visible in Figure 6.4. In data one measures $\varepsilon_{mult}^{int}(Data) =$

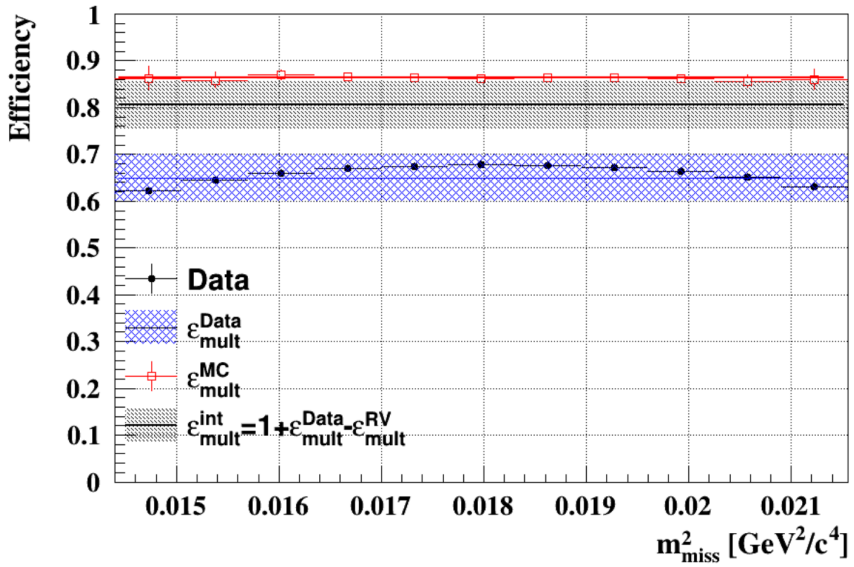

Figure 6.4: Comparison of the fraction of events surviving π-multiplicity cuts evaluated on data and MC. The relative half-difference is propagated to $\varepsilon_{veto}(\pi - induced)$ as a correction factor.

0.81 ± 0.05, while in MC the value is $\varepsilon^{MC}_{mult} = 0.863 \pm 0.001$. The relative half-difference is considered and propagated to $\varepsilon_{veto}(\pi - induced)$ as a correction factor to $A^{MC}_{\pi\nu\nu} : 0.97 \pm 0.03$. The term $\varepsilon_{veto}(\pi - induced)$ affects only $\pi\nu\nu$ and its uncertainty propagates linearly to the SES.

6.3 Normalization selection

6.3.1 $K_{2\pi}$ normalization sample selection

The $K_{2\pi}$ selection is based on the following criteria:

- control trigger;
- a positive *pion candidate*;
- the events pass the beam kinematics conditions, defined in section 4.3.1;
- the events pass the kinematics criteria, defined in section 4.3.3;
- the reconstructed decay vertex lays within 105 m and 165 m;
- no CHANTI candidate associated to the event;
- full upstream - downstream candidate matching, with the matching cuts on the discriminants and time, for details see section 4.2.2;
- a RICH ring reconstructed using the single-ring algorithm associated to the downstream candidate;
- a full calorimetric π^+ particle identification:
  - no reconstructed MUV3 candidate within ± 7 ns of the reference track time;
  - energy in MUV1+2 not associated to the track is below 5 GeV;
  - no associated cluster in MUV2 unless there is a MUV1 cluster associated to the track;
  - the pion probability, $Prob_{\pi^+}$, provided by the standard BDT PID calorimetric algorithm is:

$$Prob_{\pi^+} > max(0.7, 0.98 - 0.4596 \cdot e^{-\frac{p_{\pi^+} - 11.44}{5.27}}), \tag{6.15}$$

    where p_{π^+} is the momentum of the π^+ candidate;
  - $\frac{E_{total}}{p} < 1.2$, where E_{total} is a sum of energies from LKr, MUV1 and MUV2;
  - $\frac{E_{LKr}}{p} < 0.8$;
  - electromagnetic shape cuts, defined in section 4.3.6;
- a full RICH π^+ particle identification:
  - |Likelihood of not pion| < 0.12;
  - $m_{miss}^{RICH} \in (0.125, 0.2)$;
- cut against the *Type* 1 upstream events, defined in section 4.3.2;
- single-track cut, defined in section 4.3.4;

- $m^2_{miss} \in (0.01, 0.026)$.

The number of selected events in the bins of momenta and intensity is summarized in table 6.5.

Intensity \ Momentum	15-20	20-25	25-30	30-35
> 800	256126	444255	564361	559464
$400 - 800$	3559134	6156133	7812197	7758394
$300 - 400$	2766205	4797710	6089868	6034536
$200 - 300$	1578829	2740413	3480937	3443286
< 200	1399323	2431095	3085266	3049071

Table 6.5: Number of reconstructed $K_{2\pi}$ events in bins of momenta and intensity.

6.3.2 $K_{\mu 2}$ normalization sample selection

The $K_{\mu 2}$ events need to pass these conditions:

- control trigger;
- a positive *pioncandidate*;
- the events pass the beam kinematics conditions, defined in section 4.3.1;
- the events pass the kinematics criteria, defined in section 4.3.3;
- the reconstructed decay vertex lays within 115 m and 165 m;
- no CHANTI candidate associated to the event;
- full upstream - downstream candidate matching, with the matching cuts on the discriminants and time, for details see section 4.2.2;
- a RICH ring reconstructed using the single-ring algorithm associated to the downstream candidate;
- cut at final collimator against upstream background (*box cut*), defined in section 4.3.2;
- Z_{vertex} versus radius cut at Straw chamber against $K_{3\pi}$ background, defined by eq. (4.33);
- cut against the *Type* 1 upstream events, defined in section 4.3.2;
- selection criteria against extra activity in detectors, see section 4.3.5;
- single-track cut, defined in section 4.3.4;
- no reconstructed STRAW segments, see section 4.3.5;
- no photon multiplicity, see section 4.3.7;

- a matched MUV3 candidate to *pion candidate*;
- $m^2_{miss} \in (-0.05, m^2_{\mu-kin} + 3\sigma)$.

Number of events passing the selection in various bins of momentum and intensity is shown in Fig. .

Momentum / Intensity	15-20	20-25	25-30	30-35
> 800	62344	521736	682546	762395
$400 - 800$	1190634	9929730	12949402	14464300
$300 - 400$	1043041	8771692	11417202	12694971
$200 - 300$	634201	5349839	6964250	7714461
< 200	608808	5183740	6737557	7442275

Table 6.6: Number of reconstructed $K_{\mu 2}$ events in bins of momenta and intensity.

6.4 Acceptances

All the acceptances were obtained using a MC with the upstream pile-up generator (PileupParticleGenerator pre-analyzer), which works in the 150 ns wide time window, and generates on average 4 beam kaons per event. The final SES were checked with and without the upstream pile-up generator and were found to be stable within few per mile. When the upstream pile-up is applied, one gets better MC/Data agreement for the tails of m^2_{miss} distribution. The data-MC agreement is not perfect over a full range of invariant mass, with up to 60% discrepancy on the sides of the main peak. About 20% of this discrepancy is coming from the imperfections of simulation of the scattering in STRAWs and the rest is due to shortcomings in the upstream pile-up generator.

6.4.1 MC $\pi\nu\nu$ acceptance

For the $\pi\nu\nu$ acceptance measurement a MC sample generated with v1.1.3 was used. The decays generated within $105 < Z_{decay} < 165$ m are considered. The main difference between MC and Data is the particle identification, where the relative effect is around 10% in favor of MC. This effect, summarized in Table 6.7, is measured in bins of momentum on $\pi^+\pi^0$ sample. The other discrepancies are the $\pi - K$ matching, 5% relative difference, and $\varepsilon^{int}_{veto}(\pi - induced)$ at the level of 3% - for more details, see 6.2.3. The statistical error is, given the size of the simulated sample, negligible. The acceptance in bins of momentum is shown in Fig. 6.5 and the integrated value is:

$$A^{MC}_{\pi\nu\nu} = 0.030 \pm 0.004. \tag{6.16}$$

The errors depicted in the Figure 6.5 are set to 10%, representing the difference in PID between data and MC. The main uncertainties of PID and $\pi - K$ association will cancel out for the SES calculation when $\pi^+\pi^0$ is used as the normalization, as they are the same and only the acceptances ratio enters the calculation. If $K_{\mu 2}$

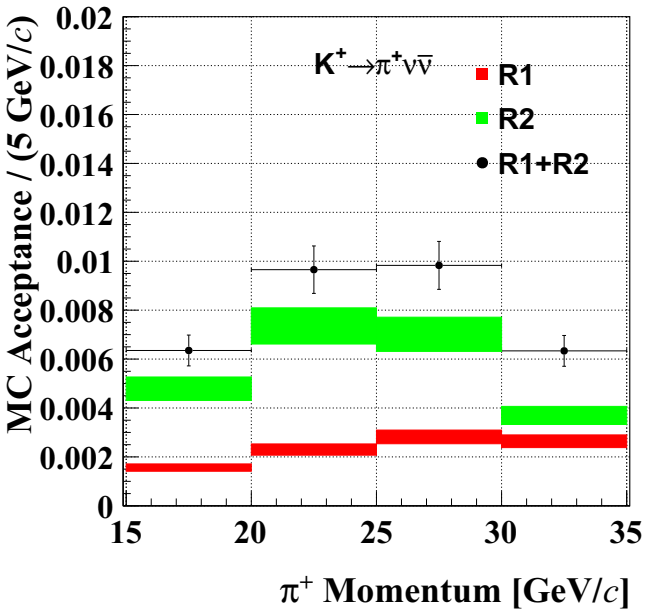

Figure 6.5: The acceptance of $\pi\nu\nu$ in bins of momentum for two signal regions and their sum.

Data					
	15-20	20-25	25-30	30-35	All
Calorimeters	0.793(1)	0.785(1)	0.768(1)	0.753(1)	0.771(1)
RICH	0.775(1)	0.860(1)	0.837(1)	0.753(1)	0.808(1)
Combined	0.615(1)	0.675(1)	0.643(1)	0.567(1)	0.623(1)
MC					
Calorimeters	0.828(1)	0.819(1)	0.805(1)	0.786(1)	0.806(1)
RICH	0.822(1)	0.900(1)	0.895(1)	0.819(1)	0.863(1)
Combined	0.681(1)	0.737(1)	0.720(1)	0.644(1)	0.696(1)

Table 6.7: Particle identification efficiencies for pion in calorimeters and RICH measured on data and MC.

is used as a normalization, only the $\pi - K$ will cancel out in the ratio, not the PID as it is not applied in this normalization channel selection. Hence, for the SES calculation, when using $K_{\mu 2}$ as a normalization, a systematic uncertainty is assigned in the bins of momentum, employing the difference between data and MC according to Table 6.7, to the acceptance. On the other hand, using $K_{\mu 2}$ as a normalization, the same treatment for the photon and multiplicity rejection is used, so only a $\varepsilon^{int}_{veto}(\pi - induced)$ needs to be applied on top. In both cases there is an effect of $\varepsilon^{int}_{veto}(\pi - induced)$ resulting in 3% systematic uncertainty.

6.4.2 MC $\pi^+\pi^0$ acceptance

The acceptance of the normalization channel was obtained from the MC sample generated with v1.1.3 within $105 < Z_{decay} < 165$ m. The agreement of the simulation compared to data was studied in various kinematic variables, see an example in Fig. 6.6.

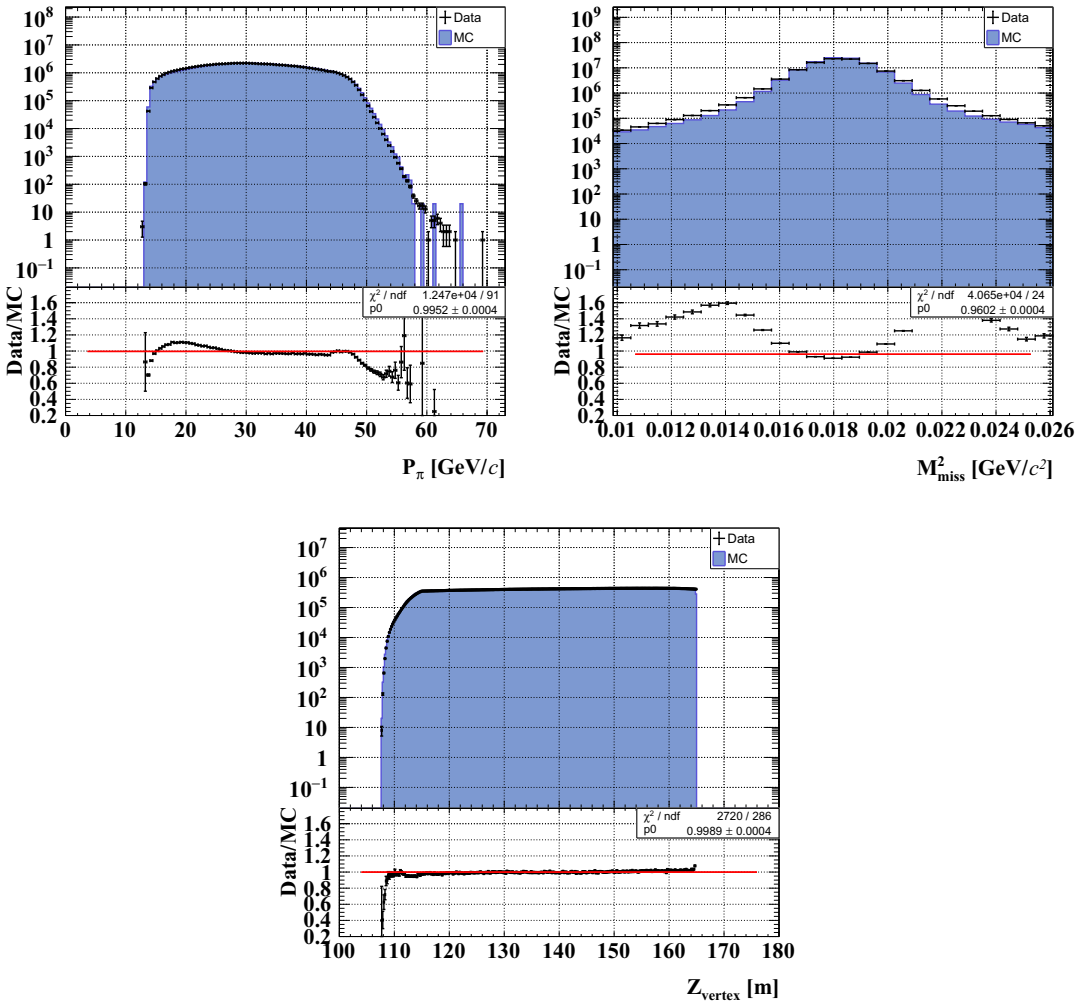

Figure 6.6: Data/MC comparison of the $K_{2\pi}$ for the momentum (top left), missing mass (top right) and Z_{vertex} distributions (bottom).

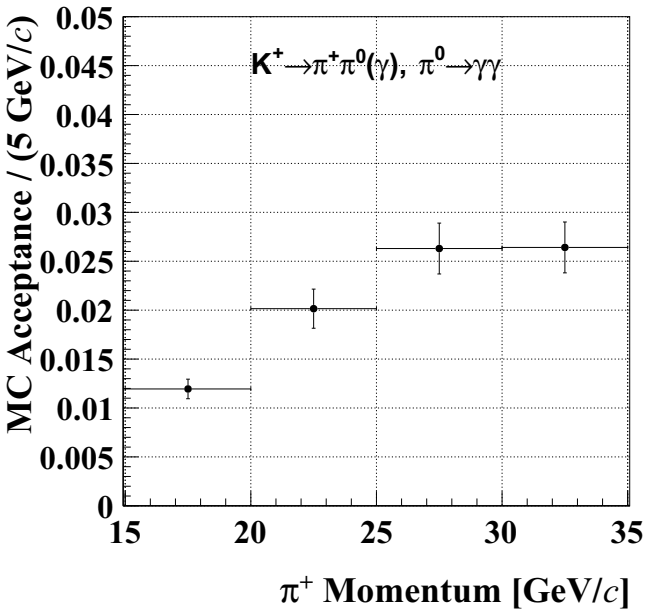

Figure 6.7: The acceptance of $\pi^+\pi^0$ in bins of momentum.

The main discrepancy between simulation and data lies again in the particle identification, which is about 10% better in the MC, and in the $K-\pi$ association, where the relative difference is at the level of 5%. The statistical error is, given the size of the simulated sample, negligible. The integrated acceptance is:

$$A_{2\pi}^{MC} = 0.09 \pm 0.01 \tag{6.17}$$

shown in bins of momentum in Fig. 6.7.

Kinematically same decay, $\pi^+\pi^0_D$, has about eight times smaller acceptance.

6.4.3 MC $\mu^+\nu$ acceptance

The analyzed MC sample was generated with v1.1.3 within $105 < Z_{decay} < 165$ m. The validation of the MC sample compared to data in different kinematic variables is shown in Fig. 6.8.

Here, RICH and calorimetric particle ID is not applied as the final state particle is different compared to signal. A positive in time signal in MUV3 is required. This requirement of MUV3 signal is efficient at the level of 99.5%. The overall acceptance is:

$$A_{\mu 2}^{MC} = 0.067 \pm 0.005, \tag{6.18}$$

where the dominant error contribution is from the $K-\pi$ association at the level of 5%. The $K-\pi$ association error is not assigned as systematics as it will cancel in the ratio with $\pi\nu\nu$ acceptance. Acceptance in bins of momentum is shown in Fig. 6.9.

6.5 SES and number of expected events

To compute the single event sensitivity and number of expected SM events two different normalization channels, $K_{2\pi}$ and $K_{\mu 2}$, are used. Both of them follow

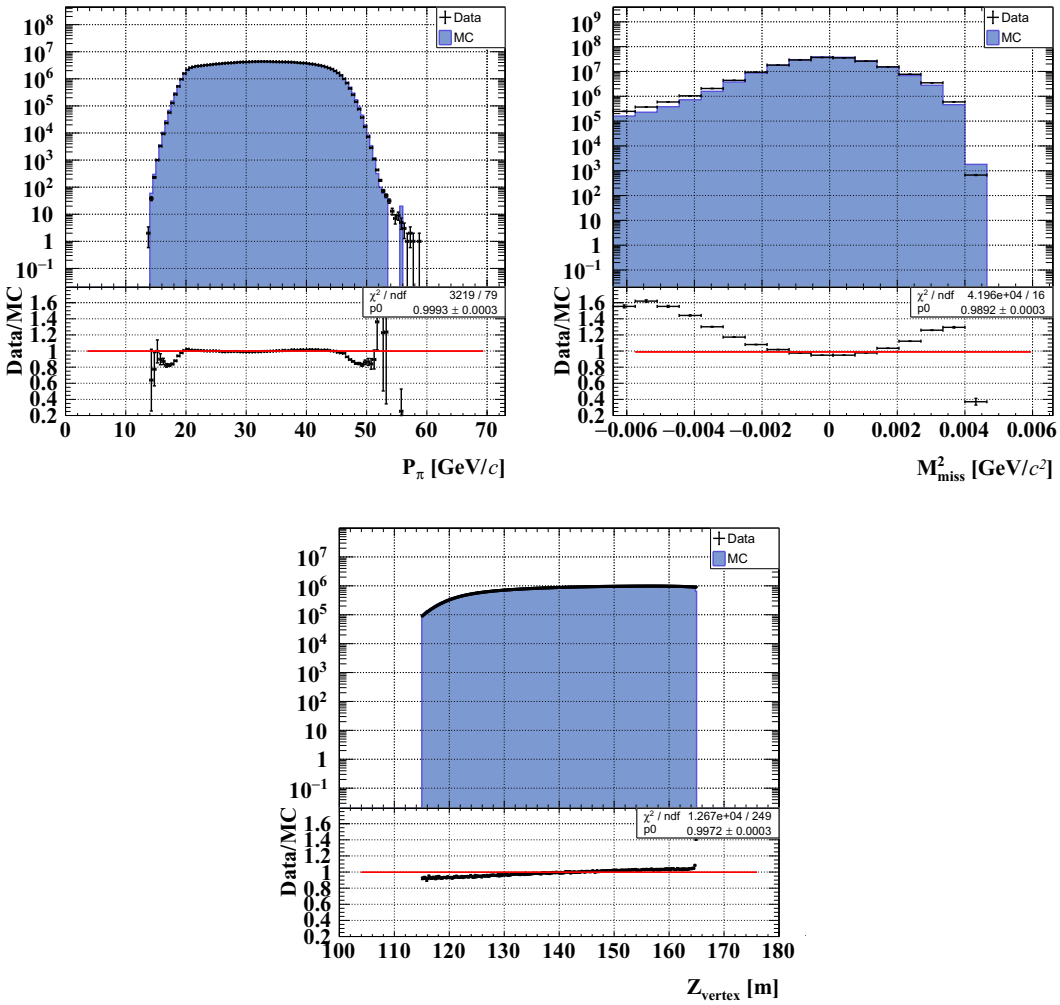

Figure 6.8: Data/MC comparison of the $K_{\mu 2}$ for the momentum (top left), missing mass (top right) and Z_{vertex} distributions (bottom).

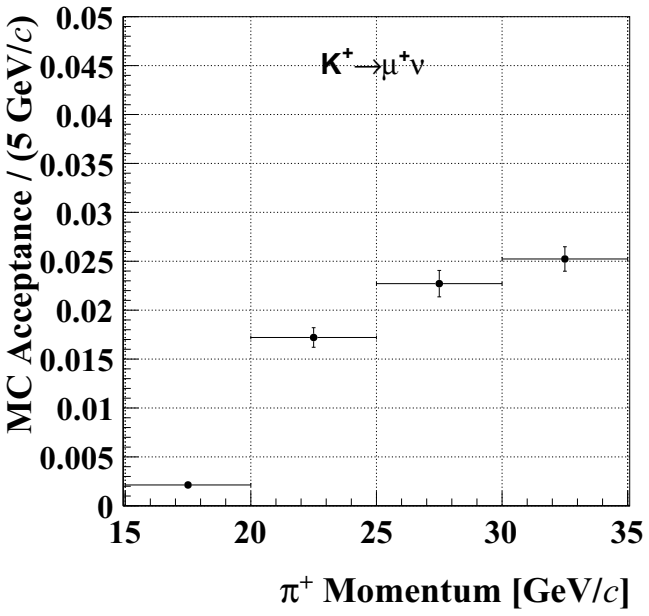

Figure 6.9: The acceptance of $\mu^+\nu$ in bins of momentum.

the analysis steps of $\pi\nu\nu$ as far as possible to cancel most of the systematic effects. The differences from $\pi\nu\nu$ are outlined below and are accounted for either in additional factors or systematical uncertainties. In the end the SES and $N_{exp}^{\pi\nu\nu}$ are compatible within the statistical and systematical errors.

6.5.1 Using $K_{2\pi}$ as normalization

When $K_{2\pi}$ as a normalization to $\pi\nu\nu$ is used, several uncertainties and imperfections, like $\pi - K$ association and particle identification, will cancel out in the ratio. However, some effects are not taken into account in the simulation and the final SES needs to be scaled with some external factors, namely Random Veto and Trigger efficiencies, measured on data. Then the final formula for SES computation has the following form:

$$SES_{K_{2\pi}} = \frac{1}{N_K^{2\pi} \cdot A_{\pi\nu\nu} \cdot \varepsilon_{RV} \cdot \varepsilon_{trig} \cdot \varepsilon_{veto}(\pi - induced)}, \tag{6.19}$$

where $N_K^{2\pi}$ means effective number of kaon decays measured through the $K_{2\pi}$ stream as explained in 6.3.1. The resulting SES integrated over the beam intensity and π^+ momentum is:

$$SES_{K_{2\pi}} = (3.78 \pm 0.21) \times 10^{-11}. \tag{6.20}$$

The breakdown of the error budget is reported in Table 6.8.

The SES are calculated in bins of π^+ momentum and beam intensity, assuming that $\pi\nu\nu$ events have been taken at the same intensity of the $\pi^+\pi^0$ events selected for normalization. They are shown in Figure 6.10 as a functions of π^+ momentum and beam intensity, together with statistical and systematical errors.

Comparing them with the SM branching fraction prediction
$BR(K^+ \to \pi^+\nu\bar{\nu}) = (8.4 \pm 1.0) \times 10^{-11}$, and integrating over π^+ momentum and

Source	Uncertainty $\times 10^{-11}$
L0 trigger	± 0.15
Acceptance	± 0.12
Random veto	± 0.08
L1 trigger	± 0.03
Normalization background	< 0.001

Table 6.8: The error budget of SES obtained using $K_{2\pi}$ as a normalization.

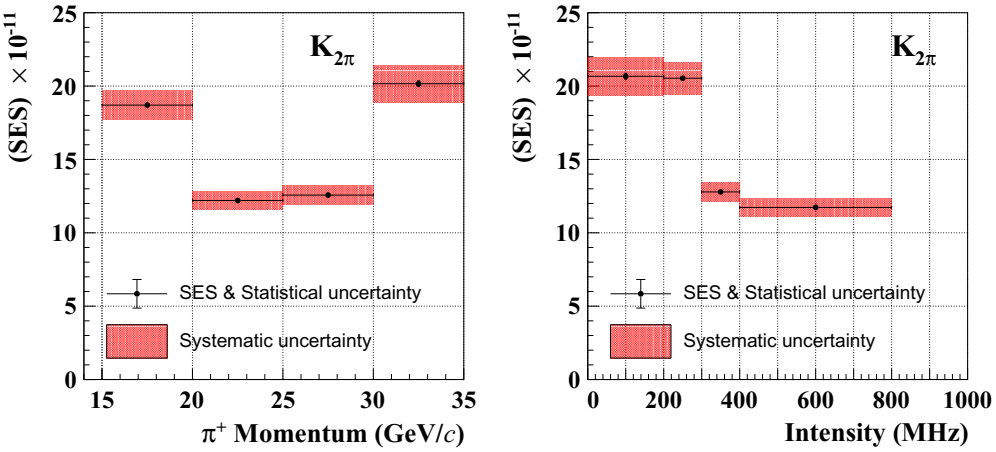

Figure 6.10: SES in bins of π^+ momentum (left) and beam intensity (right), with the corresponding statistical and systematical errors.

beam intensity bins, one gets the number of expected events:

$$N_{\pi\nu\nu}^{exp} = \frac{BR(K^+ \to \pi^+ \nu\bar{\nu})}{SES_{K_{2\pi}}} = 2.22 \pm 0.12 \pm 0.26_{ext}, \tag{6.21}$$

where the first error propagates from the SES and the second represents the external uncertainty from the branching fraction theoretical prediction. The number of expected events in separate bins of π^+ momentum and beam intensity, without the external uncertainty, are published in Table 6.9.

Figure 6.11 details the $N_{\pi\nu\nu}^{exp}$ in bins of π^+ momentum and beam intensity, together with the combined statistical and systematical uncertainty, and the ex-

Momentum → Intensity ↓	15-20	20-25	25-30	30-35	Sum
0-200 MHz	0.082(4)	0.126(7)	0.122(6)	0.076(4)	0.406(26)
200-300 MHz	0.083(4)	0.127(7)	0.123(7)	0.077(4)	0.409(22)
300-400 MHz	0.133(7)	0.203(11)	0.198(11)	0.123(7)	0.657(35)
400-800 MHz	0.145(8)	0.222(12)	0.215(11)	0.134(7)	0.716(38)
>800 MHz	0.007(1)	0.011(1)	0.010(1)	0.006(1)	0.033(4)
Sum	0.449(23)	0.688(36)	0.668(36)	0.417(27)	2.22(12)

Table 6.9: Number of expected SM $\pi\nu\nu$ events, using $K_{2\pi}$ as normalization. The shown errors does not contain the external uncertainty from $BR(K^+ \to \pi^+ \nu\bar{n}\bar{u})$ theoretical prediction.

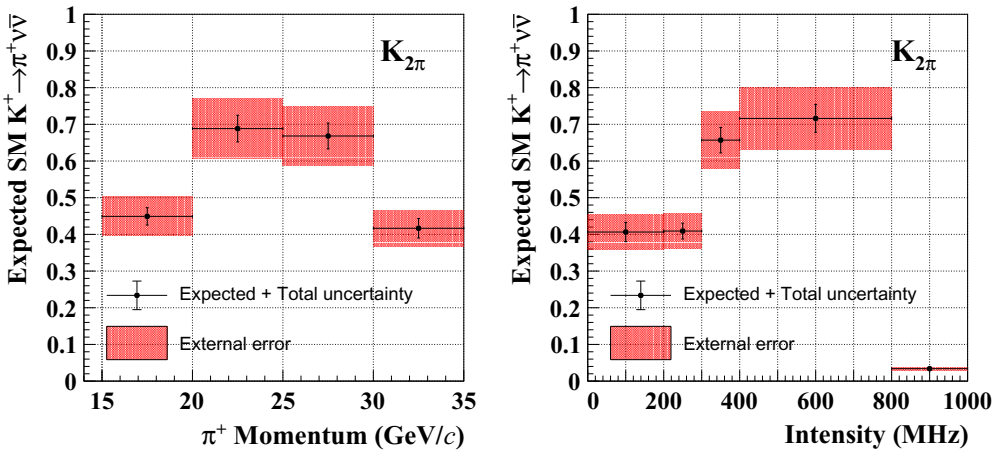

Figure 6.11: Number of expected SM $\pi\nu\nu$ events in bins of π^+ momentum (left) and beam intensity (right), using $K_{2\pi}$ as a normalization. The combined statistical and systematical uncertainty, and the external error are drawn.

ternal error.

6.5.2 Using $K_{\mu 2}$ as normalization

Using $K_{\mu 2}$ as a normalization differs from $K_{2\pi}$ in various aspects. Most notably, the full photon and multiplicity rejection is applied and particle identification cuts are not, only an in-time candidate in MUV3 is required. So, while the $\pi - K$ association imperfections are canceled in the ratio, particle ID Data/MC discrepancies will result in larger systematical uncertainty in the acceptances. On the other hand, random veto is not present in the computation of SES and one can write:

$$SES_{K_{\mu 2}} = \frac{1}{N_K^{\mu 2} \cdot A_{\pi\nu\nu} \cdot \varepsilon_{trig} \cdot \varepsilon_{veto}(\pi - induced)}, \tag{6.22}$$

where $N_K^{\mu 2}$ represents the effective number of kaon decays, for details see section 6.3.2. Integrating over downstream track momentum and beam intensity bins, one gets a following SES:

$$SES_{K_{\mu 2}} = (3.37 \pm 0.36) \times 10^{-11}. \tag{6.23}$$

The contributing uncertainties are outlined in Table 6.10, where the dominant input comes from the acceptance, due to imperfect simulation of PID in the RICH and the calorimeters.

Source	Uncertainty $\times 10^{-11}$
Acceptance	± 0.34
L0 trigger	± 0.15
L1 trigger	± 0.03
Normalization background	< 0.001

Table 6.10: The error budget of SES obtained using $K_{\mu 2}$ as a normalization.

SES as a functions of π^+ momentum and beam intensity are depicted in Figure 6.12.

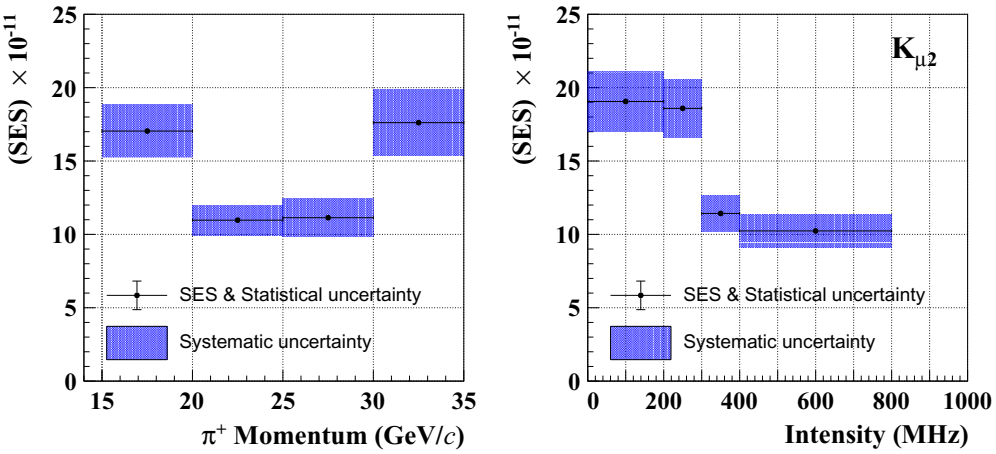

Figure 6.12: SES as a functions of π^+ momentum (left) and beam intensity (right). The statistical and systematical errors are shown.

Momentum → Intensity ↓	15-20	20-25	25-30	30-35	Sum
0-200 MHz	0.087(12)	0.136(19)	0.134(19)	0.084(13)	0.441(47)
200-300 MHz	0.089(13)	0.139(19)	0.137(20)	0.086(13)	0.452(48)
300-400 MHz	0.146(20)	0.226(31)	0.223(32)	0.141(21)	0.735(79)
400-800 MHz	0.163(23)	0.251(34)	0.248(36)	0.158(24)	0.821(88)
>800 MHz	0.008(1)	0.013(2)	0.013(2)	0.008(1)	0.041(5)
Sum	0.493(52)	0.766(72)	0.754(86)	0.477(60)	2.49(0.27)

Table 6.11: Number of expected SM $\pi\nu\nu$ events, using $K_{\mu 2}$ as normalization. The shown errors does not contain the external uncertainty from $BR(K^+ \to \pi^+\nu\bar{\nu})$ theoretical prediction.

Combining SES with the SM $BR(K^+ \to \pi^+\nu\bar{\nu}) = (8.4 \pm 1.0) \times 10^{-11}$ prediction, the number of expected SM events is obtained. They are summarized in single bins of π^+ momentum and beam intensity, with their statistical and systematical errors, in Table 6.11. Integrating over the bins one gets an overall number of expected events:

$$N_{\pi\nu\nu}^{exp} = \frac{BR(K^+ \to \pi^+\nu\bar{\nu})}{SES_{K_{\mu 2}}} = 2.49 \pm 0.27 \pm 0.30_{ext}. \tag{6.24}$$

The $N_{exp}^{\pi\nu\nu}$ as a functions of μ^+ momentum and beam intensity are illustrated in Figure 6.13.

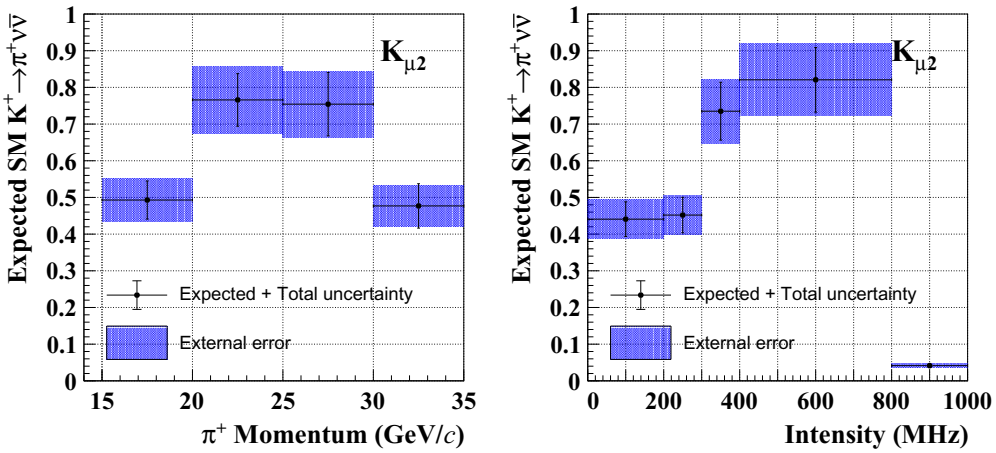

Figure 6.13: Number of expected SM $\pi\nu\nu$ events in bins of π^+ momentum (left) and beam intensity (right), using $K_{2\pi}$ as a normalization. The combined statistical and systematical uncertainty, and the external error are drawn.

7. Results

The preliminary result from the 2017 data is obtained using the $K_{2\pi}$ decay as a normalization. This choice is made as the PID simulation imperfections cancels out and does not induce a large systematic uncertainty as in the case of $K_{\mu 2}$.

After unmasking the signal regions, two events are observed in R2, see Fig. 7.1. The background profiles in Fig. 7.2 show that both events are in the regions with the high signal/background ratio, far from edges of the signal regions. Their selected properties are listed in Table 7.1.

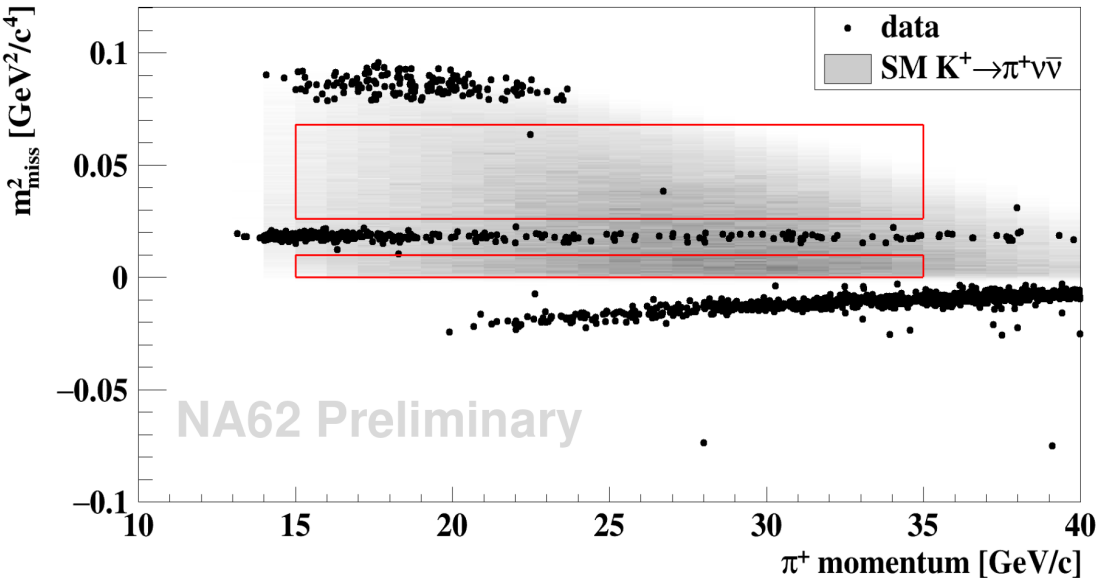

Figure 7.1: Distribution of events after unmasking the signal regions. Two events are present in the R2.

Property	Signal Event 1	Signal Event 2
Z_{vertex} [m]	140.4	158.8
CDA [mm]	0.609	1.383
$p_{\pi+}$ [GeV/c]	26.53	22.39
m^2_{miss} [GeV$^2/c^4$]	0.038	0.064
$m^2_{miss}(Beam)$ [GeV$^2/c^4$]	0.034	0.064
$m^2_{miss}(RICH)$ [GeV$^2/c^4$]	0.034	0.065
Pion probability	0.9965	0.9973
Muon probability	0.001	0.003
RICH mass [MeV/c^2]	134.4	139.7
Kaon momentum [GeV/c]	74.97	75.48

Table 7.1: Selected properties of the signal events.

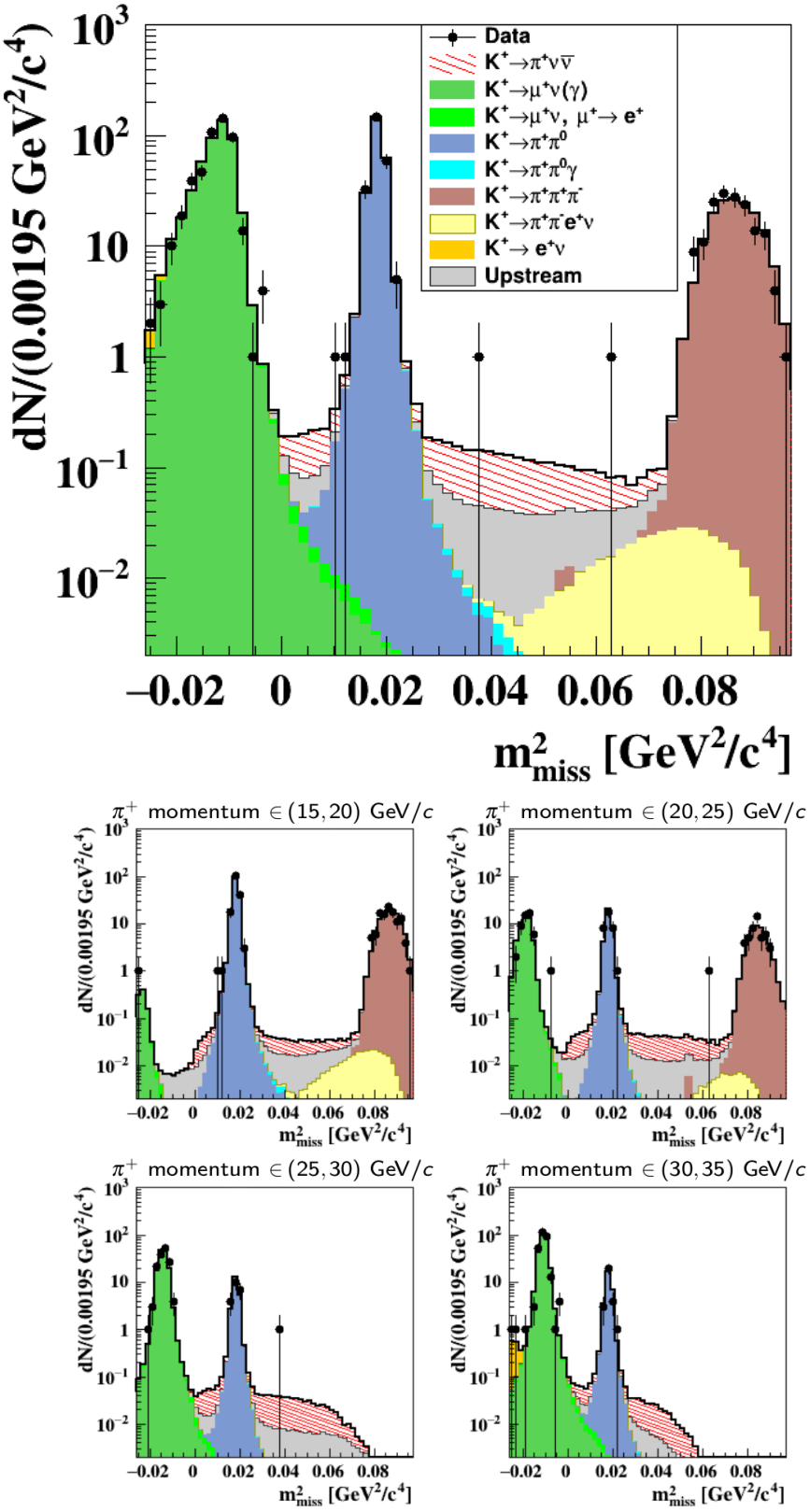

Figure 7.2: The m^2_{miss} distribution of the data and expected background events after $\pi\nu\nu$ selection in the full 15-35 GeV/c momentum range (top) and in 5 GeV/c wide bins (bottom).

Single event sensitivity	$(3.78 \pm 0.21) \times 10^{-11}$
Expected background	1.50 ± 0.30
Expected SM signal events	2.22 ± 0.29
Events observed	2

Table 7.2: Final results from the $\pi\nu\nu$ analysis of the 2017 data.

Observed	Expected (background only)	CL
$BR(\mathrm{K}^+ \to \pi^+\nu\bar{\nu}) < 1.76 \times 10^{-10}$	$BR(\mathrm{K}^+ \to \pi^+\nu\bar{\nu}) < 1.41 \times 10^{-10}$	90%
$BR(\mathrm{K}^+ \to \pi^+\nu\bar{\nu}) < 2.11 \times 10^{-10}$	$BR(\mathrm{K}^+ \to \pi^+\nu\bar{\nu}) < 1.76 \times 10^{-10}$	95%

Table 7.3: Observed and expected upper limits on the branching ratio at 90% and 95% CL.

7.1 Statistical interpretation

The expected number of signal and background events with the final observation is summarized in table 7.2. They are Poisson-distributed variables.

The interpretation of the result is performed with the hybrid Bayesian-frequentist approach [64] and the CLs method [65]. The statistical model is a counting experiment with only one parameter, the $\mathrm{K}^+ \to \pi^+\nu\bar{\nu}$ SM branching ratio. Symmetric uncertainties of the input variables are considered. The corresponding expected and observed upper limits on the branching ratio are presented in Table 7.3, for two different confidence levels (CL).

The decay rate computed with the two-sided 68% band is:

$$BR(\mathrm{K}^+ \to \pi^+\nu\bar{\nu}) = (0.20^{+0.69}_{-0.20}) \times 10^{-10}. \tag{7.1}$$

7.2 Combined 2016 and 2017 results

Combining data from 2016 with 2017 results in the upper limits presented in Table 7.4. Again, the Bayesian-frequentist approach and the CLs method are used.

The decay rate with the two-sided 68% band is:

$$BR(\mathrm{K}^+ \to \pi^+\nu\bar{\nu}) = (0.47^{+0.72}_{-0.47}) \times 10^{-10}. \tag{7.2}$$

This result is compatible with the existing measurement performed by the E787 and E949 experiments in BNL. Fig. 7.3 shows the comparison of the NA62 combined result with the previous measurements and the theoretical prediction.

The measurement of the charged kaon decay to charged pion, neutrino and anti-neutrino is theoretically connected in the SM, and in most of its extensions, with the neutral kaon decay to neutral pion, neutrino and anti-neutrino. This

Observed	Expected (background only)	CL
$BR(\mathrm{K}^+ \to \pi^+\nu\bar{\nu}) < 1.85 \times 10^{-10}$	$BR(\mathrm{K}^+ \to \pi^+\nu\bar{\nu}) < 1.32 \times 10^{-10}$	90%
$BR(\mathrm{K}^+ \to \pi^+\nu\bar{\nu}) < 2.44 \times 10^{-10}$	$BR(\mathrm{K}^+ \to \pi^+\nu\bar{\nu}) < 1.62 \times 10^{-10}$	95%

Table 7.4:

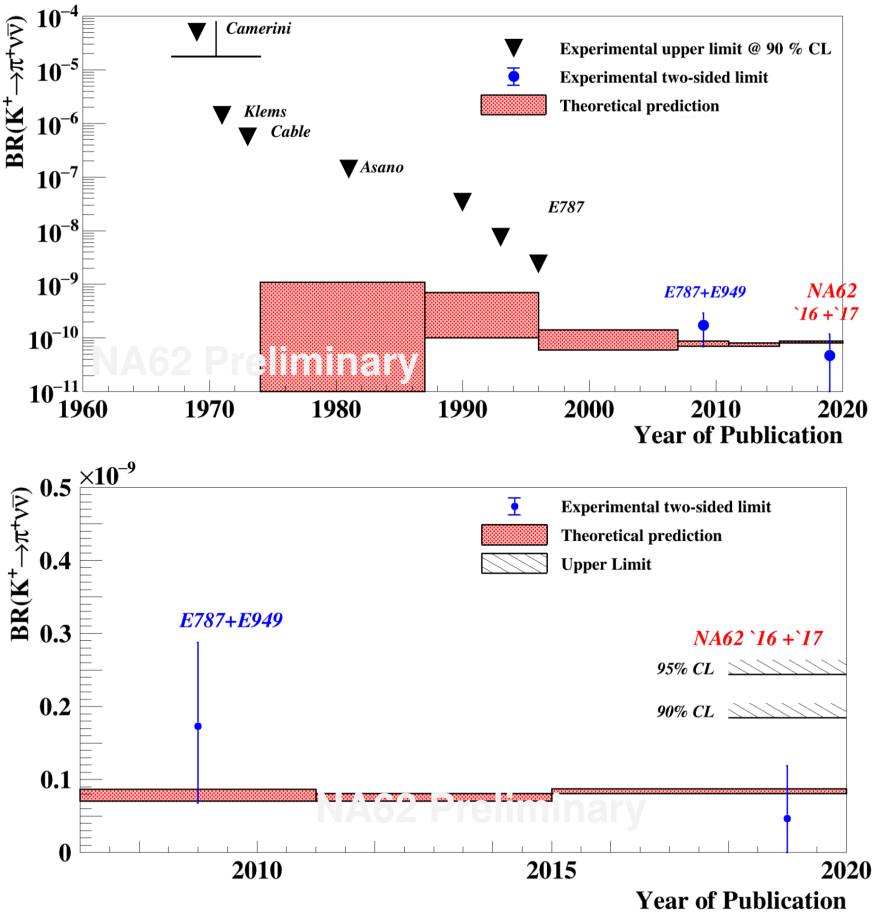

Figure 7.3: New NA62 measurement in the context of the previous experiments compared to the theoretical prediction. The upper plot shows the whole timeline, while the lower plot is zoomed to the two best measurements in recent years.

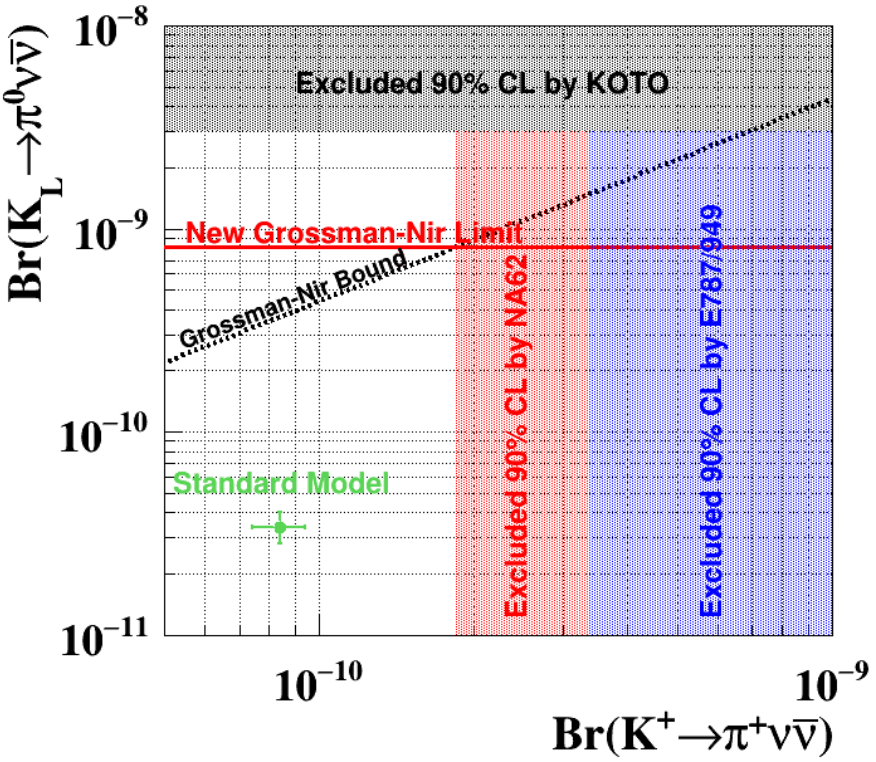

Figure 7.4: Grossman-Nir bound.

connection is represented by the Grossman-Nir condition (1.52), explained in section 1.5. The new NA62 measurement can, through this connection, set an upper limit on the neutral kaon decay, as is shown in Fig. 7.4.

Conclusion

Analysis of the data collected by the NA62 experiment in 2017 has been performed. After the selection, two events are observed in the signal region. The final result of the $K^+ \to \pi^+ \nu\bar{\nu}$ decay branching ratio is obtained. The upper limit on the branching ratio measured on the 2017 data is:

$$BR(K^+ \to \pi^+ \nu\bar{\nu}) < 1.76 \times 10^{-10} \qquad @90\% \text{ CL.} \tag{7.3}$$

The decay rate computed with the two-sided 68% band is:

$$BR(K^+ \to \pi^+ \nu\bar{\nu}) = (0.20^{+0.69}_{-0.20}) \times 10^{-10}. \tag{7.4}$$

After combining the 2017 data sample with the previously analyzed data collected in 2016, where one event was observed, the following result is obtained:

$$BR(K^+ \to \pi^+ \nu\bar{\nu}) < 1.85 \times 10^{-10} \qquad @90\% \text{ CL.} \tag{7.5}$$

The decay rate computed with the two-sided 68% band for 2016 combined with 2017 data samples is:

$$BR(K^+ \to \pi^+ \nu\bar{\nu}) = (0.47^{+0.72}_{-0.47}) \times 10^{-10}. \tag{7.6}$$

The analysis of 2018 data sample is ongoing and NA62 plans to continue data taking in 2021.

A. Appendix

A.1 Full $K^+ \to \pi^+\pi^0$ selection

The following criteria are required to select $K^+ \to \pi^+\pi^0$ events:

- at least 1, but no more than 2000 LKr hits;
- at least 1 good STRAW track passing through the geometrical acceptance, with associated activity in NA48CHOD, CHOD and LKr;
- NA48CHOD track time must be within ±25 ns of the trigger time;
- a selected track must have associated KTAG and GTK candidates;
- contol trigger;
- one and only one pair of the LKr clusters compatible with the π^0 decay, see App. A.4;
- the π^0 is within ±5 ns of the NA48CHOD track time;
- $115 < Z^{\pi^0}_{vertex} < 165$ m;
- the decay vertex reconstructed using kaon and the π^+ candidate must be in the region (115, 165) m;
- no associated CHANTI candidate;
- the event must pass the kinematics criteria, defined in section 4.3.3;
- no photons in LAV, IRC and SAC, as described in section 4.3.7;
- only two standard clusters reconstructed in LKr not associated to the π^+ candidate;
- momentum of the expected π^+ between (5, 80) GeV; here the expected π^+ momentum is computed assuming that the reconstructed π^0 is produced at $Z^{\pi^0}_{vertex}$ and the nominal beam momentum and direction are taken;
- the expected π^+ is at least 150 mm distant from each of the photon candidates;
- a standard LKr cluster is closer than 200 mm from the position of the expected π^+ at the LKr surface and within ±5 ns of the $]pi^0$ time; if the standard LKr cluster is missing a cluster is looked for by summing up the cells above 40 MeV closer than 200 mm to the position of the expected pi^+ at the LKr surface; in this last case the cluster must be within ±8 ns of the π^0 time;
- $0.008 < m^2_{miss}(\pi^0) < 0.031$ GeV$^2/c^4$, where $m^2_{miss}(\pi^0) = (p_K - p_{\pi^0})^2$, with p_K is the nominal kaon 4-momentum and π^0 is the measured π^0 4-momentum.

A.2 $K^+ \to \pi^+\pi^+\pi^-$ selection

The $K^+ \to \pi^+\pi^+\pi^-$ sample is selected using the following criteria:

- three good STRAW tracks passing through the geometrical acceptance, with associated activity in NA48CHOD and LKr and no association in MUV3;
- exactly one three-track vertex reconstructed with the VertexLSF tool [58];
- a RICH ring reconstructed with the standalone ring reconstruction must be associated to one of the positive pion tracks. The time T_{RICH} is computed as the average of the ring times of the matched pions;
- the KTAG candidate closest in time with T_{RICH} must have 5 or more sectors fired and must be within ± 2 ns of T_{RICH};
- no activity in the SAC, IRC and LAV detectors;
- the invariant mass of the three pions $m_{3\pi}$ must be in the 491.5−495.5 MeV/c^2 mass range.

A.3 $K^+ \to \pi^0 e^+ \nu_e$ selection

$K^+ \to \pi^0 e^+ \nu_e$ events were extracted with the following conditions:

- at least 1, but no more than 2000 LKr hits;
- at least 1 good STRAW track passing through the geometrical acceptance, with associated activity in NA48CHOD, CHOD and LKr;
- NA48CHOD track time must be within ± 25 ns of the trigger time;
- a selected track must have associated KTAG and GTK candidates;
- contol trigger;
- one and only one pair of the LKr clusters compatible with the π^0 decay, see App. A.4;
- the π^0 is within ± 5 ns of the NA48CHOD track time;
- $115 < Z^{\pi^0}_{vertex} < 165$ m;
- $Z_{e^+} \in (115, 165)$;
- the event must pass the kinematics criteria, defined in section 4.3.3;
- the events pass the beam kinematics conditions, defined in section 4.3.1;
- full upstream - downstream candidate matching, with the matching cuts on the discriminants and time, for details see section 4.2.2;
- identified π^0 decay, see App. A.4;

- the π^0 is within ± 5 ns of the NA48CHOD track time;
- no associated CHANTI candidate;
- transverse momentum $P_T > 0.04$ GeV/c;
- no MUV3 candidate associated to the STRW track;
- m^2_{miss} out of $K_{2\pi}$ kinematic region defined in Table 3.1;
- $|P_K - P_{e^+} - P_{\pi^0}|^2 \leq 0.01$, where the P_K, P_{e^+} and P_{π^0} are the 4-momenta of the kaon, positron and π^0, respectively;
- exactly one RICH ring reconstructed using the single-ring algorithm associated to the downstream candidate;
- no reconstructed STRAW segments, see section 4.3.5;
- single-track cut, defined in section 4.3.4;
- downstream track momentum within (15, 35) GeV/c range;
- $E_{LKr}/p > 0.8$, where E_{LKr} is the energy of the track associated LKr cluster and $|p|$ is its momentum;
- no photons in LAV, IRC and SAC, as described in section 4.3.7.

A.4 π^0 decay identification

To identify a π^0 decay, the following conditions is applied:

- at lest 2 electromagnetic-like clusters in LKr (*photon candidate*), where a cluster is electromagnetic-like if the following conditions are satisfied:
  - the cluster is reconstructed by the standard LKr algorithm;
  - its energy, E_{LKr}, is ≥ 3 GeV;
  - is at least 20 mm away of the dead cell;
  - it is located at least 150 mm from the center of the LKr;
  - it satisfies the condition $0.2 < E_{LKrSeed}/E_{LKr} < 0.44$ together with $1 \leq (N_{LKrCell} - 2.21)/(0.93 \cdot E_{LKr}) < 2.2$;
- the 2 *photon candidates* should be in time within ± 3 ns between each other and at least 150 mm distant from each other;
- a photon pair satisfying the previous conditions must be produced at $105 < Z^{\pi^0}_{vertex} < 180$ m, where $Z^{\pi^0}_{vertex}$ is computed from the energy and position of the photon clusters assuming the π^0 mass and the nominal beam direction and momentum;
- the selected *photon candidates* must not intersect the RICH beam pipe.

Bibliography

[1] G. Anelli et al. Proposal to measure the rare decay $K^+ \to \pi^+\nu\bar{\nu}$ at the CERN SPS. 2005.

[2] Giancarlo D'Ambrosio and Gino Isidori. $K^+ \to \pi^+\nu\bar{\nu}$: A Rising star on the stage of flavor physics. *Phys. Lett.*, B530:108–116, 2002.

[3] S. Adler et al. Further search for the decay $K^+ \to \pi^+\nu\bar{\nu}$. *Phys. Rev. Lett.*, 84:3768–3770, 2000.

[4] S. Adler et al. Further evidence for the decay $K^+ \to \pi^+\nu\bar{\nu}$. *Phys. Rev. Lett.*, 88:041803, 2002.

[5] Stephen Scott Adler et al. Search for the decay $K^+ \to \pi^+\nu\bar{\nu}$ in the momentum region P(pi) less than 195-MeV/c. *Phys. Lett.*, B537:211–216, 2002.

[6] S. Adler et al. Further search for the decay $K^+ \to \pi^+\nu\bar{\nu}$ in the momentum region P ¡ 195-MeV/c. *Phys. Rev.*, D70:037102, 2004.

[7] V. V. Anisimovsky et al. Improved measurement of the $K^+ \to \pi^+\nu\bar{\nu}$ branching ratio. *Phys. Rev. Lett.*, 93:031801, 2004.

[8] A. V. Artamonov et al. New measurement of the $K^+ \to \pi^+\nu\bar{\nu}$ branching ratio. *Phys. Rev. Lett.*, 101:191802, 2008.

[9] S. Adler et al. Measurement of the $K^+ \to \pi^+\nu\bar{\nu}$ branching ratio. *Phys. Rev.*, D77:052003, 2008.

[10] Eduardo Cortina Gil et al. First search for $K^+ \to \pi^+\nu\bar{\nu}$ using the decay-in-flight technique. *Phys. Lett.*, B791:156–166, 2019.

[11] S. L. Glashow, J. Iliopoulos, and L. Maiani. Weak Interactions with Lepton-Hadron Symmetry. *Phys. Rev.*, D2:1285–1292, 1970.

[12] William J. Marciano and Zohreh Parsa. Rare kaon decays with "missing energy". *Phys. Rev.*, D53(1):R1, 1996.

[13] D. Rein and L. M. Sehgal. Long Distance Contributions to the Decay $K^+ \to \pi^+$ Neutrino anti-neutrino. *Phys. Rev.*, D39:3325, 1989.

[14] John S. Hagelin and Laurence S. Littenberg. Rare Kaon Decays. *Prog. Part. Nucl. Phys.*, 23:1, 1989.

[15] Gerhard Buchalla and Andrzej J. Buras. $K \to \pi$ neutrino anti-neutrino and high precision determinations of the CKM matrix. *Phys. Rev.*, D54:6782–6789, 1996.

[16] Gerhard Buchalla and Andrzej J. Buras. QCD corrections to rare K and B decays for arbitrary top quark mass. *Nucl. Phys.*, B400:225–239, 1993.

[17] Mikolaj Misiak and Jorg Urban. QCD corrections to FCNC decays mediated by Z penguins and W boxes. *Phys. Lett.*, B451:161–169, 1999.

[18] Gino Isidori, Federico Mescia, and Christopher Smith. Light-quark loops in $K \to \pi\nu\bar{\nu}$. *Nucl. Phys.*, B718:319–338, 2005.

[19] Viacheslav Duk. Search for $K^+ \to \pi^+\nu\bar{\nu}$ at the NA62 experiment. *EPJ Web Conf.*, 130:06001, 2016.

[20] Joachim Brod, Martin Gorbahn, and Emmanuel Stamou. Two-Loop Electroweak Corrections for the $K \to \pi\nu\bar{\nu}$ Decays. *Phys. Rev.*, D83:034030, 2011.

[21] Gerhard Buchalla and Andrzej J. Buras. Two loop large m_t electroweak corrections to $K \to \pi\nu\bar{\nu}$ for arbitrary Higgs boson mass. *Phys. Rev.*, D57:216–223, 1998.

[22] Andrzej J. Buras, Dario Buttazzo, Jennifer Girrbach-Noe, and Robert Knegjens. $K^+ \to \pi^+\nu\overline{\nu}$ and $K_L \to \pi^0\nu\overline{\nu}$ in the Standard Model: status and perspectives. *JHEP*, 11:033, 2015.

[23] Thomas Hermann, Mikolaj Misiak, and Matthias Steinhauser. Three-loop QCD corrections to $B_s \to \mu^+\mu^-$. *JHEP*, 12:097, 2013.

[24] Martin Gorbahn. Latest results of the $K \to \pi\nu\bar{\nu}$ branching ratio calculations. *Presentation on KAON conference*, 2019.

[25] Gino Isidori, Guido Martinelli, and Paolo Turchetti. Rare kaon decays on the lattice. *Phys. Lett.*, B633:75–83, 2006.

[26] Joachim Brod and Martin Gorbahn. Electroweak Corrections to the Charm Quark Contribution to $K^+ \to \pi^+\nu\bar{\nu}$. *Phys. Rev.*, D78:034006, 2008.

[27] A. I. Vainshtein, Valentin I. Zakharov, V. A. Novikov, and Mikhail A. Shifman. On the Strong Interaction Effects on the $K(L) \to 2\mu$ Decay and $K(L)$ $K(s)$ Mass Difference. A Reply. *Phys. Rev.*, D16:223, 1977.

[28] John R. Ellis and J. S. Hagelin. Constraints on Light Particles from Kaon Decays. *Nucl. Phys.*, B217:189–214, 1983.

[29] Gerhard Buchalla and Andrzej J. Buras. The rare decays $K^+ \to \pi^+\nu\bar{\nu}$ and $K_L \to \mu^+\mu^-$ beyond leading logarithms. *Nucl. Phys.*, B412:106–142, 1994.

[30] Andrzej J. Buras, Martin Gorbahn, Ulrich Haisch, and Ulrich Nierste. Charm quark contribution to $K^+ \to \pi^+\nu\bar{\nu}$ at next-to-next-to-leading order. *JHEP*, 11:002, 2006. [Erratum: JHEP11,167(2012)].

[31] Federico Mescia and Christopher Smith. Improved estimates of rare K decay matrix-elements from Kl3 decays. *Phys. Rev.*, D76:034017, 2007.

[32] Gerhard Buchalla, Andrzej J. Buras, and Markus E. Lautenbacher. Weak decays beyond leading logarithms. *Rev. Mod. Phys.*, 68:1125–1144, 1996.

[33] Yuval Grossman and Yosef Nir. $K_L \to \pi^0$ neutrino anti-neutrino beyond the standard model. *Phys. Lett.*, B398:163–168, 1997.

[34] Andrzej J. Buras, Dario Buttazzo, and Robert Knegjens. $K \to \pi\nu\overline{\nu}$ and ϵ'/ϵ in simplified new physics models. *JHEP*, 11:166, 2015.

[35] Monika Blanke, Andrzej J. Buras, and Stefan Recksiegel. Quark flavour observables in the Littlest Higgs model with T-parity after LHC Run 1. *Eur. Phys. J.*, C76(4):182, 2016.

[36] Monika Blanke, Andrzej J. Buras, Bjorn Duling, Katrin Gemmler, and Stefania Gori. Rare K and B Decays in a Warped Extra Dimension with Custodial Protection. *JHEP*, 03:108, 2009.

[37] Tomáš Blažek and Peter Maták. Left–left squark mixing, $K^+ \to \pi^+\nu\bar{\nu}$ and minimal supersymmetry with large $\tan\beta$. *Int. J. Mod. Phys.*, A29(27):1450162, 2014.

[38] Gino Isidori, Federico Mescia, Paride Paradisi, Christopher Smith, and Stephanie Trine. Exploring the flavour structure of the MSSM with rare K decays. *JHEP*, 08:064, 2006.

[39] Marzia Bordone, Dario Buttazzo, Gino Isidori, and Joachim Monnard. Probing Lepton Flavour Universality with $K \to \pi\nu\bar{\nu}$ decays. *Eur. Phys. J.*, C77(9):618, 2017.

[40] S. Fajfer, N. Košnik, and L. Vale Silva. Footprints of leptoquarks: from $R_{K^{(*)}}$ to $K \to \pi\nu\bar{\nu}$. *Eur. Phys. J.*, C78(4):275, 2018.

[41] Andrzej J. Buras and Robert Fleischer. Bounds on the unitarity triangle, $\sin 2\beta$ and $K \to \pi\nu\bar{\nu}$ decays in models with minimal flavor violation. *Phys. Rev.*, D64:115010, 2001.

[42] Andrzej J. Buras. Minimal Flavour Violation. arXiv:hep-ph/0310208, 2003.

[43] Andrzej J. Buras, Fulvia De Fazio, and Jennifer Girrbach. The Anatomy of Z' and Z with Flavour Changing Neutral Currents in the Flavour Precision Era. *JHEP*, 02:116, 2013.

[44] Andrzej J. Buras, Dario Buttazzo, Jennifer Girrbach-Noe, and Robert Knegjens. Can we reach the Zeptouniverse with rare K and $B_{s,d}$ decays? *JHEP*, 11:121, 2014.

[45] Eduardo Cortina Gil et al. The Beam and detector of the NA62 experiment at CERN. *JINST*, 12(05):P05025, 2017.

[46] F Hahn et al. NA62: Technical Design Document. Technical Report NA62-10-07, CERN, Geneva, Dec 2010.

[47] Claude Bovet, Réne Maleyran, L Piemontese, Alfredo Placci, and Massimo Placidi. *The CEDAR counters for particle identification in the SPS secondary beams: a description and an operation manual*. CERN Yellow Reports: Monographs. CERN, Geneva, 1982.

[48] E. Goudzovski et al. Development of the kaon tagging system for the na62 experiment at cern. *Nuclear Instruments and Methods in Physics Research Section A: Accelerators, Spectrometers, Detectors and Associated Equipment*, 801:86 – 94, 2015.

[49] Collaboration NA62. 2017 NA62 status report to the CERN SPSC. Technical Report CERN-SPSC-2017-013. SPSC-SR-208, CERN, Geneva, Mar 2017.

[50] F. Ambrosino et al. CHANTI: a fast and efficient charged particle veto detector for the NA62 experiment at CERN. *Journal of Instrumentation*, 11(03):P03029–P03029, mar 2016.

[51] R. Veenhof. Garfield - simulation of gaseous detectors. http://garfield.web.cern.ch/garfield. Accessed: 2019-11-18.

[52] R. E. Kalman. A New Approach to Linear Filtering and Prediction Problems. *Journal of Basic Engineering*, 82(1):35–45, 03 1960.

[53] S A Fedotov, A A Kleymenova, and A N Khotjantsev. New CHOD detector for the NA62 experiment at CERN. *Phys. Part. Nucl.*, 49(1):26–29. 4 p, 2018.

[54] J. R. Batley et al. Observation of a cusp-like structure in the $\pi^0\pi^0$ invariant mass distribution from $K^+ \to \pi^\pm\pi^0\pi^0$ decay and determination of the $\pi\ \pi$ scattering lengths. *Phys. Lett.*, B633:173–182, 2006.

[55] Aliberti R. Particle Identification with Calorimeters for the Measurement of the Rare Decay $K^+ \to \pi^+\nu\bar{\nu}$ at NA62. PhD thesis at Johannes Gutenberg Univeristat Mainz, 2018.

[56] NA62 Collaboration. Data formats, 2017.

[57] Francesco Brizioli. Lkr cluster energy corrections fine-tuning based on π^0 mass, 2019.

[58] Na62 framework. http://na62-sw.web.cern.ch/doxygen. Accessed: 2019-11-19.

[59] Hoecker A. et al. Tmva - toolkit for multivariate data analysis. arXiv:physics/0703039.

[60] Brun R. et al. Root - data analysis framework. https://root.cern.ch/.

[61] Marchevski R. I. First measurement of the $K^+ \to \pi^+\nu\bar{\nu}$ decay with the NA62 experiment at CERN. PhD thesis at Johannes Gutenberg Univeristat Mainz, 2018.

[62] NA62 Collaboration. 2019 na62 status report to the cern spsc. https://na62.web.cern.ch/na62/Documents/SPSC-SR-249.pdf, 2019.

[63] M. Tanabashi et al. Review of particle physics. *Phys. Rev. D*, 98:030001, Aug 2018.

[64] Robert D. Cousins, James T. Linnemann, and Jordan Tucker. Evaluation of three methods for calculating statistical significance when incorporating a systematic uncertainty into a test of the background-only hypothesis for a poisson process. *Nuclear Instruments and Methods in Physics Research Section A: Accelerators, Spectrometers, Detectors and Associated Equipment*, 595(2):480 – 501, 2008.

[65] A L Read. Presentation of search results: theCLstechnique. *Journal of Physics G: Nuclear and Particle Physics*, 28(10):2693–2704, sep 2002.

List of Figures

1 History of the experimental efforts directed towards the $K^+ \to \pi^+\nu\bar{\nu}$ decay rate measurement. 5

1.1 Feynman box-diagrams and $Z-$penguin diagram in the SM [19]. . 7
1.2 Possible scale dependence in NNLO for the top quark contribution (left) and error budget to $X(x_t)$ at NLO (right). 9
1.3 $P_c(X)$ as a function of the scale parameter μ_c in the NLO (left) and NNLO (right). The different lines correspond to various strategies of the $\alpha_s(\mu_c)$ computations [30]. 11
1.4 Error budget of the BR for the charged (left) and the neutral (right) $K \to \pi\nu\bar{\nu}$ decays [22]. 13
1.5 Example of the NP correlations in the plane of $K \to \pi\nu\bar{\nu}$ BRs [34]. The green bands correspond to Minimal Flavour Violation models, where no right-handed interactions are present. The blue lines illustrate the correlation between the BRs in the Littlest Higgs with T-parity and Z' FCNC models, with pure left-handed or right-handed couplings. The expanding red area represent the models with general left- and right-handed couplings, such as Randall-Sundrum models with custodial symmetry, where no correlation is expected. 16

2.1 Schematic drawing of the K12 beam line. The solid red line represents the trajectory of a particle produced in the middle of the target at a nominal momentum at the indicated angle. The dashed line corresponds to the trajectory of an initially on-axis particle with the nominal momentum [45]. 20
2.2 Close view of the beam line in the downstream part of the NA62 experiment [45]. 21
2.3 Schematic view of the NA62 detectors [45]. 22
2.4 Schematic layout of the momentum measurement in the second achromat (A2). The beam arrives to the first GTK station, then it is deflected vertically by 60 mm by two C-shaped dipole magnets. Then it passes through the second GTK station and returns to its nominal direction by another pair of dipoles. Before reaching the third GTK station, the beam crosses the collimators C6/C7 and is deflected by TRIM5. Inside the achromat, there is a toroidally magnetized scraping iron collimator (SCR1) sweeping away muons together with return yokes of the last two magnets of the achromat (dark shaded areas) [45, 46]. 23
2.5 Left: Orientations of the views inside the chamber, with the 12 cm hole for the passage of the beam. Right: The arrangement of the straws in a single view. This geometry was chosen to ensure that passing particle will always cross at least two straws per view, as needed to resolve the left-right ambiguity. The 3°angle represents the angular range of tracks produced in kaon decays and detected within the geometrical acceptance of the spectrometer [45]. 25

2.6 Left: The lead glass crystal with attached PM and light guide [45]. Right: The schematic drawing of the LAV station [46]. 26
2.7 The schematic view of the RICH detector [45]. 26
2.8 Schematic sketch of the CHOD planes [45]. 28
2.9 The schematic sketch of the MUV0 detector. The arrow on the left indicates the position of the RICH vessel [45]. 28
2.10 IRC detector installation in front of the LKr cryostat (left side), prior to wrapping in black paper for light tightness [45]. 29
2.11 The accordion geometry of ribbons inside the LKr. 30
2.12 Position of spacers in the LKr used to assure stability and permanent tension of about 20 N of ribbons [45]. 30
2.13 Schematic view of the muon veto detectors. First two, MUV1 and MUV2, are hadronic calorimeters, then followed by 80 cm iron wall and the fast scintillator detector MUV3 [55]. 32
2.14 Profile view of MUV3 cell, with scintillator tile and two PMs inside a light tight box [45]. 33
2.15 One HASC module made of 60 scintillator and 60 lead plates (left) and one read out section made of 6 scintillator plates interleaved with lead (right) [45]. 34
2.16 Illustration of the LKr corrections based on π^0 mass. Left: The reconstructed π^0 mass before (blue) and after (red) the corrections are applied. Right: Reconstructed missing mass from the $K^+ \to e^+\pi^0\nu$ events before (blue) and after (red) the corrections are applied. 40

3.1 Distribution of m^2_{miss} for the signal and background processes. Note that the signal curve is enhanced by a factor 10^{10} [45]. . . . 42
3.2 Resolution of the squared missing mass as a function of the π^+ momentum with a break-down of the contributions. 43
3.3 Signal, control and background regions marked in the p_{π^+}, m^2_{miss} plane. 44

4.1 Left: The distribution of the CHOD48 discriminant with marked cut. Right: The distribution of the time difference between the CHOD48 candidate and the track time as measured by STRAW; the cut is set at ± 20 ns. 46
4.2 Left: The distribution of the CHOD discriminant with marked cut. Right: The distribution of the time difference between the CHOD candidate and the track time as measured by STRAW. 47
4.3 Left: Distribution of the time difference between RICH single ring time and CHOD48 time. Right: Distribution of the RICH discriminant D_{RICH}, as defined in eq. (4.3). 48
4.4 The difference between the LKr cluster time and CHOD48 time. . 49
4.5 Left: The time difference between the KTAG candidate and the *pion candidate*. Right: Distribution of number of active KTAG sectors, with highlighted cut. 51
4.6 The time difference distributions between GTK track time and KTAG (left), RICH (right) candidate times. 53

4.7 Left: The closest distance of approach (CDA) between GTK and STRAW tracks. Right: A 2D plane with discriminants defined in eq. (4.10), with selection cut marked by the red line and highlighted signal region. 53
4.8 Left: Distribution of $\Delta T = T_{GTK} - T_{KTAG}$ for GTK tracks tagged by $K_{3\pi}$ events with the corresponding PDF function, with the same distribution for the pileup tracks using kaon time shifted by 15 ns. Right: Comparison of the CDA distributions for the kaon track and pileup GTK track. 55
4.9 Projection of the decay vertex in (x, y) plane at $Z_{vertex} = 105$ m (left) and at $Z_{vertex} = 165$ m (right). The reconstructed vertex coordinates must be compatible with the beam profile at a give Z_{vertex} position, marked with the black box. 56
4.10 Illustration of the early decays producing the *upstream events*. The kaon (blue line) decays after the second GTK station and all products of the decay, except a pion (red line), are absorbed in the collimator. A pileup pion track (dashed black line), giving a good GTK candidate, is associated to the pion from the decay, reconstructing a fake vertex. The pion from the decay can pass through the inner part of the collimator (upper plot), or through the gaps in the last dipole of the achromat (lower plot). 57
4.11 Position at TRIM5 of downstream track from a data sample enriched for upstream events. Left plot represents the $Type$ 1 events, while right plot illustrates the distribution of the $Type$ 2 events. Blue lines indicate the contour of the last dipole of the second achromat, four red boxes represent the four blocks of the final collimator and black line correspond to the acceptance region covered by CHANTI. 58
4.12 Distribution of the Z_{vertex} as a function of the radius of the downstream track in the first STRAW chamber. On the left the $\pi\nu\bar{\nu}$ MC simulation is shown, while plot on the right is obtained from the $K_{2\pi}$ MC where the kaons are decaying upstream the fiducial volume. The red contours specify the cut. 59
4.13 Ring radius measured by RICH as a function of momentum for positrons, muons and pions. The dashed lines mark the signal region of the $\pi\nu\bar{\nu}$ analysis, owing to best performance of the particle identification. 64
4.14 Top: RICH efficiency for the pions and muons as a function of their momentum. Middle: Pion and muon efficiencies after applying calorimetric particle identification as a function of their momentum. Bottom: The combined particle identification efficiencies for pions and muons measured on control data samples. 66
4.15 Left: The m^2_{miss} distribution of the $K_{2\pi}$ events selected on control trigger before applying photon rejection and multiplicity cuts. Right: The same distribution for the $K_{2\pi}$ events selected on $\pi\nu\nu$ trigger after applying photon rejection and multiplicity cuts. . . . 68
4.16 Rejection of π^0 as a function of momentum (left) and instantaneous beam intensity (right) [62]. 69

4.17 The distribution of the events after the full $\pi\nu\bar{\nu}$ selection. Signal and control regions are kept masked. 70

5.1 The effect of the π^0 tagging studied on MC. It has no bias in the tails in R1 and it reduces significantly the background in R2. . . . 73
5.2 Distribution of m^2_{miss} of the selected $K_{2\pi}$ control events using data, with two γ from π^0 tagged in the LKr (black dots). MC distribution of $K_{2\pi}$ with tagged π^0 is superimposed (red line), with the 1 σ systematic uncertainty (red band). The simulated pileup contribution to m^2_{miss} is illustrated by the gray bands. A small contribution of $K_{3\pi}$ events is visible in the large m^2_{miss} region. 74
5.3 Kinematic tails f^{kin} variations with respect to momentum (left) and beam intensity (right). 74
5.4 Validation of the $K_{2\pi}(\gamma)$ background as a function of momentum. The red boxes represent the expected number of $K_{2\pi}(\gamma)$ events with errors (area of the box) in the control regions around the $\pi^+\pi^0$ peak. The black dots correspond to number of events observed, with the statistical uncertainties, after unmasking the control regions. 75
5.5 Distribution of m^2_{miss} of the selected $K_{\mu 2}$ control events using data (black dots). MC distribution is superimposed (red line), with the 1 σ systematic uncertainty (red band). The simulated pileup contribution to m^2_{miss} is illustrated by the gray bands. 76
5.6 Kinematic tails f^{kin} variations with respect to momentum (left) and intensity (right). 77
5.7 Validation of the $K_{\mu 2}(\gamma)$ background as a function of momentum. The red boxes represent the expected number of $K_{\mu 2}(\gamma)$ events in the $CR_{K_{\mu 2}}$. The black dots correspond to number of events observed after unmasking the $CR_{K_{\mu 2}}$. 78
5.8 Validation of the K_{e4} background of the samples. The red boxes represent the expected number of K_{e4} events in the $0.026 < m^2_{miss} < 0.072$ GeV$^2/c^4$ control region. The black dots correspond to number of events observed after unmasking this control region. 80
5.9 Distribution of the *upstream events* in the $T_{GTK}-T_{KTAG}$, $T_{RICH}-T_{KTAG}$ plane. The accidental bands around $T_{RICH} - T_{KTAG} = 0$ and $T_{GTK} - T_{KTAG} = 0$ correspond to *Type* 1, 2 events and *Type* 3 events, respectively. *Type* 4 and 5 events are around the center of the plot. 82

5.10 Top left: comparison of the CDA distribution between the $Type$ 1 events found in the geometrical region $D1$ extracted from a MC simulation (blue histogram) and a data sample with events from the geometrical region of $D1$ but in the side-bands of the ΔT distribution and with the $K-\pi$ matching inverted (black dots with error bars). The PDF used in the mistagging probability simulation is the fit of the MC distribution (solid red line). Top right: same comparison, but for events in geometrical region C. The resulting PDF (solid red line) extracted from the MC histogram (blue histogram) agrees with the data ($\chi^2/DoF = 0.6$) and it is the one used for the $\pi\nu\overline{\nu}$ background estimation. Bottom: CDA distribution of $Type$ 2 events taken from data in the geometrical region of the $D2$ sample but in the side-bands of the ΔT distribution and with $K-\pi$ matching inverted (blue dots with error bars). The PDF used in the mis-tagging probability simulation is the fit to the distribution (red solid line). 85
5.11 Top left: the mis-matching probability $P_{K-\pi}^{matching}$ as a function of $|\Delta T|$ for $Type$ 1 events in sample $D1$. Top left: $P_{K-\pi}^{matching}$ for $Type$ 1 events in sample C used for the upstream background estimation in the $\pi\nu\overline{\nu}$ signal region. Bottom: $P_{K-\pi}^{matching}$ for $Type$ 2 events. . . 86
5.12 Validation of the Upstream background samples. The red boxes represent the expected number of events in the control region. The black dots correspond to number of events observed after unmasking this control region. 87
5.13 The distribution of the m^2_{miss} in the pion mass hypothesis as a function of the downstream track momentum. 92
5.14 The distribution of events after unmasking control regions. Signal regions are kept masked. 94

6.1 Total L0×L1 trigger efficiencies in bins of intensity in four momentum bins, with L1LAV conditions as defined before run 8025. . . . 99
6.2 Total L0×L1 trigger efficiencies in bins of intensity in four momentum bins, with L1LAV conditions as defined after run 8025. . . . 100
6.3 RV as a function of the instantaneous intensity. The single subdetectors and combined effect are presented. 101
6.4 Comparison of the fraction of events surviving π-multiplicity cuts evaluated on data and MC. The relative half-difference is propagated to $\varepsilon_{veto}(\pi - induced)$ as a correction factor. 102
6.5 The acceptance of $\pi\nu\nu$ in bins of momentum for two signal regions and their sum. 106
6.6 Data/MC comparison of the $K_{2\pi}$ for the momentum (top left), missing mass (top right) and Z_{vertex} distributions (bottom). 107
6.7 The acceptance of $\pi^+\pi^0$ in bins of momentum. 108
6.8 Data/MC comparison of the $K_{\mu 2}$ for the momentum (top left), missing mass (top right) and Z_{vertex} distributions (bottom). 109
6.9 The acceptance of $\mu^+\nu$ in bins of momentum. 110
6.10 SES in bins of π^+ momentum (left) and beam intensity (right), with the corresponding statistical and systematical errors. 111

6.11 Number of expected SM $\pi\nu\nu$ events in bins of π^+ momentum (left) and beam intensity (right), using $K_{2\pi}$ as a normalization. The combined statistical and systematical uncertainty, and the external error are drawn. 112
6.12 SES as a functions of π^+ momentum (left) and beam intensity (right). The statistical and systematical errors are shown. 113
6.13 Number of expected SM $\pi\nu\nu$ events in bins of π^+ momentum (left) and beam intensity (right), using $K_{2\pi}$ as a normalization. The combined statistical and systematical uncertainty, and the external error are drawn. 114

7.1 Distribution of events after unmasking the signal regions. Two events are present in the R2. 115
7.2 The m^2_{miss} distribution of the data and expected background events after $\pi\nu\nu$ selection in the full 15-35 GeV/c momentum range (top) and in 5 GeV/c wide bins (bottom). 116
7.3 New NA62 measurement in the context of the previous experiments compared to the theoretical prediction. The upper plot shows the whole timeline, while the lower plot is zoomed to the two best measurements in recent years. 118
7.4 Grossman-Nir bound. 119

List of Tables

3.1 Definition of two signal regions (R1, R2), two control regions for $K_{2\pi}$ (CR1 and CR2), control region for $K_{\mu 2}$ ($CR_{K_{\mu 2}}$) and background regions for $K_{\mu 2}$, $K_{2\pi}$ and $K_{3\pi}$. Downstream track momentum p_{π^+} is in GeV/c and m^2_{miss}, $m^2_{miss}(Beam)$ and $m^2_{miss}(RICH)$ are defined in (3.2), (3.6), and the missing mass resolution σ is defined in (3.5). 44

4.1 The energy dependent timing cuts to classify the extra LKr clusters as photons. 67
4.2 Summary of time cuts for IRC and SAC. The times T_{IRC} and T_{SAC} represent the IRC and SAC hit times. ToT is the time over threshold measured by the TDC readout module. 68

5.1 List of all considered backgrounds, with corresponding branching ratios (BR) [63] and mechanism used to suppress them. 71
5.2 Trigger efficiency (ε^{Trig}), random veto efficiency (ε^{RV}) and total number of kaon decays (N_K) estimated from the 2017 data. . . . 71
5.3 Number of observed events in given momentum bins. 72
5.4 Number of expected events in control (CR1, CR2) and signal (R1, R2) regions. 73
5.5 The error budget for the $N^{\pi\pi}_{expected}$. 73
5.6 Number of observed events in bins of momentum. 77
5.7 Number of expected events in control (CR) and signal (SR) regions. 77
5.8 The error budget for the $N^{\mu\nu}_{expected}$. 78
5.9 Number of expected and observed events in the control (CR) regions. 79
5.10 Number of expected and observed events for various K_{e4} validation samples. 80
5.11 The error break-down for the $N^{expected}_{upstream}$. 87
5.12 Particle identification cut efficiencies studied on MC for several different modes. The estimation of acceptances of the K_{e3} selection for signal and the most significant backgrounds after the $E/p > 0.8$ cut is given in the last row. 88
5.13 Number of the reconstructed K_{e3} events from different periods, background contamination and the final RICH electron misinterpretation as pion. The limit on the overall RICH efficiency is obtained with the CLs method at 68% confidence level. 89
5.14 Values entering the calculation of ε^{Total} for $K_{2\pi_D}$. The errors not listed are negligible compared to the others and were thus ignored. 90
5.15 Various efficiencies contributing to the evaluation of ε^{Total} as defined by Eq. 5.18 for different ranges. 91
5.16 Expected background of background events in different ranges. . . 91
5.17 List of background contributions to $\pi\nu\nu$ signal process. 94

6.1 L0 trigger efficiencies in momentum and intensity bins. 98
6.2 L1 trigger efficiencies in intensity bins before and after run 8025. . 98
6.3 Random veto rejection at the different beam intensities. 100

6.4 RV value and breakdown of its error budget. 100
6.5 Number of reconstructed $K_{2\pi}$ events in bins of momenta and intensity. 104
6.6 Number of reconstructed $K_{\mu 2}$ events in bins of momenta and intensity. 105
6.7 Particle identification efficiencies for pion in calorimeters and RICH measured on data and MC. 106
6.8 The error budget of SES obtained using $K_{2\pi}$ as a normalization. . 111
6.9 Number of expected SM $\pi\nu\nu$ events, using $K_{2\pi}$ as normalization. The shown errors does not contain the external uncertainty from $BR(K^+ \to \pi^+ \nu \bar{n} u)$ theoretical prediction. 111
6.10 The error budget of SES obtained using $K_{\mu 2}$ as a normalization. . 112
6.11 Number of expected SM $\pi\nu\nu$ events, using $K_{\mu 2}$ as normalization. The shown errors does not contain the external uncertainty from $BR(K^+ \to \pi^+ \nu \bar{\nu})$ theoretical prediction. 113

7.1 Selected properties of the signal events. 115
7.2 Final results from the $\pi\nu\nu$ analysis of the 2017 data. 117
7.3 Observed and expected upper limits on the branching ratio at 90% and 95% CL. 117
7.4 117

List of Abbreviations

SM - Standard Model
CERN - Conseil Européen pour la Recherche Nucléaire
SPS - Super Proton Synchrotron
BR - Branching Ratio
CKM - Cabibbo-Kobayashi-Maskawa
BNL - Brookhaven National Laboratory
CL - Confidence Level
FCNC - Flavour-Changing Neutral Current
BSM - Beyond the Standard Model
QCD - Quantum Chromodynamics
SD - Short-Distance
NP - New Physics
LO - Leading Order
NLO - Next-to-Leading Order
NNLO - Next-to-Next-to-Leading Order
RG - Renormalization Group
SES - Single Event Sensitivity
CDA - Closest Distance of Approach
MC - Monte Carlo

List of publications

E. Cortina Gil *et al.* [NA62 Collaboration], "The Beam and detector of the NA62 experiment at CERN," JINST **12**, no. 05, P05025 (2017). [arXiv:1703.08501 [physics.ins-det]].

E. Cortina Gil *et al.* [NA62 Collaboration], "First search for $K^+ \to \pi^+ \nu\bar{\nu}$ using the decay-in-flight technique," Phys. Lett. B **791**, 156 (2019). [arXiv:1811.08508 [hep-ex]].

Selected proceedings

M. Zamkovsky [NA62 Collaboration], "Rare strange particle decays," [arXiv:1906.08567 [hep-ex]].

M. Zamkovsky [NA62 Collaboration], "Search for heavy neutral leptons at the NA62 experiment at CERN," Int. J. Mod. Phys. A **33**, no. 31, 1844026 (2018).

M. Zamkovsky [NA62 Collaboration], "Searches for heavy neutral lepton production and lepton flavour violation in kaon decays at the NA62 experiment," PoS ICHEP **2018**, 188 (2019).